

Spontaneous Emission of a Single Trapped Ca^+ -Ion

Dissertation

zur Erlangung des Doktorgrades an der
naturwissenschaftlichen Fakultät
der Leopold-Franzens-Universität Innsbruck

vorgelegt von

Axel Kreuter

durchgeführt am Institut für Experimentalphysik
unter der Leitung von
o. Univ. Prof. Dr. R. Blatt

Innsbruck
September 2004

Abstract

This thesis reports on the experimental demonstration of a highly deterministic atom-cavity field interaction. A single $^{40}\text{Ca}^+$ ion is trapped in a Paul trap situated inside an optical high finesse cavity. The resonator is stabilised to the narrow $S_{1/2}$ - $D_{5/2}$ atomic transition and the lifetime of the $D_{5/2}$ level is measured at different positions in the vacuum standing wave in the cavity. A reduction of the lifetime of $\approx 15\%$ in the node of the standing wave is observed.

For the lifetime measurement a new technique is introduced based on high-efficiency quantum state detection after deterministic excitation to the D-state and subsequent free, unperturbed spontaneous decay. This method allows the precise lifetime measurement of both metastable D-levels, $D_{5/2}$ and $D_{3/2}$, using a single ion. The result for the natural lifetime of the $D_{5/2}$ state of 1168(9) ms agrees excellently with the most precise published value. The lifetime of the $D_{3/2}$ state is measured with a single ion for the first time and yields 1176(11) ms which improves the statistical uncertainty of previous results by a factor of four. Systematic errors are discussed in detail.

Zusammenfassung

Diese Arbeit berichtet über die experimentelle Realisierung kontrollierter Kopplung zwischen einem Atom und einem Resonatorfeld. Ein einzelnes $^{40}\text{Ca}^+$ Ion wird in einer Paul-Falle gefangen, die sich in einem optischen hoch-Finesse Resonator befindet. Der Resonator wird auf den atomaren $S_{1/2}$ - $D_{5/2}$ Übergang stabilisiert, und die Lebensdauer des $D_{5/2}$ Niveaus wird an verschiedenen Positionen in der Vacuum Stehwelle des Resonators gemessen. Im Knoten der Stehwelle wird eine Lebendauerverkürzung von etwa 15% beobachtet.

Für die Lebensdauerermessung wird eine neue Methode vorgestellt, die auf hoch-effizienter Quantenzustandsdetektion nach deterministischer Anregung und freiem, ungestörtem atomarem Zerfall basiert. Diese Methode erlaubt die Lebensdauerermessung beider metastabilen D-Niveaus, $D_{5/2}$ und $D_{3/2}$, an einem einzelnen Ion. Das Ergebnis für die natürliche Lebensdauer des $D_{5/2}$ Niveaus ist 1168(9) ms in hervorragender Übereinstimmung mit dem genauesten bisher veröffentlichten Wert. Die $D_{3/2}$ Lebensdauer wird erstmals an einem einzelnen Ion gemessen, wobei das Ergebnis von 1176(11) ms den statistischen Fehler bisheriger Messungen um einen Faktor vier reduziert. Systematische Fehler werden ausführlich diskutiert.

Contents

1	Introduction	1
1.1	Single Particle Experiments	2
1.2	CQED Experiments in Perspective	3
2	Theory of Spontaneous Emission	7
2.1	Approaches to Atom-Field Interaction	7
2.1.1	Semiclassical Theory	8
2.1.2	Jaynes-Cummings Model	9
2.2	Spontaneous Emission in the Weisskopf-Wigner Approximation	10
2.3	Cavity QED and The Purcell Effect	12
3	Experimental Set-Up	15
3.1	General Principles	15
3.1.1	Ion Traps	15
3.1.2	Optical Resonators	17
3.2	The Trap-Cavity Assembly	20
3.3	Calcium	22
3.4	Laser Sources	23
3.5	Geometry	26
3.6	The Transfer Lock	28
4	Characterisation of a Single Ion	31
4.1	Loading and Detection	31
4.2	The Electronic State	32
4.3	The Motional State	34
4.3.1	Cooling	34
4.3.2	Heating	38
5	Lifetime Measurements	41
5.1	Overview	41
5.2	The $D_{5/2}$ Level	42
5.2.1	Method	42
5.2.2	Results and Discussion	44

Contents

5.3	The $D_{3/2}$ Level	48
5.3.1	Method	48
5.3.2	Results and Discussion	49
5.4	Comparison with other Experimental and Theoretical Results	53
6	Enhanced Spontaneous Emission	57
6.1	Ion-Cavity Coupling	57
6.1.1	Coherent Coupling	57
6.1.2	Standing Wave Pattern	58
6.1.3	Lateral Positioning	60
6.2	AC-Stark Shift	62
6.3	Mapping the Cavity Vacuum Field	63
6.4	Discussion	64
7	Summary and Conclusion	67
A	Loading a Single Ion: Tricks and Hints	69
B	Statistical Methods for Data Analysis	71
C	Systematic Errors	75
C.1	Detection Error	75
C.2	Rate Error	77
C.3	π Pulse Error	78
D	Lifetime Measurement Strategy at a Single Delay Time	81
E	Spontaneous emission lifetime of a single trapped Ca^+ ion in a high finesse cavity	83
F	New experimental and theoretical approach to the 3d ^2D-level lifetimes of $^{40}\text{Ca}^+$	89
	Bibliography	103

1 Introduction

In an unobtrusive article in 1946 Purcell pointed out that the spontaneous emission probability of nuclear magnetic moment transitions can be considerably enhanced when the system is coupled to a resonant electrical circuit. In that case thermal equilibrium at room temperature could be reached in the order of minutes instead of 5×10^{21} seconds [1]. This article became one of the most widely cited references in works on cavity quantum electrodynamics (CQED) being the first explicit note on the 'Purcell effect': the shortening of an atomic lifetime by modified boundary conditions of the vacuum. It took almost 40 years until it was observed experimentally - in a totally different system and with pure academic motivation. Today, in the context of quantum computation,

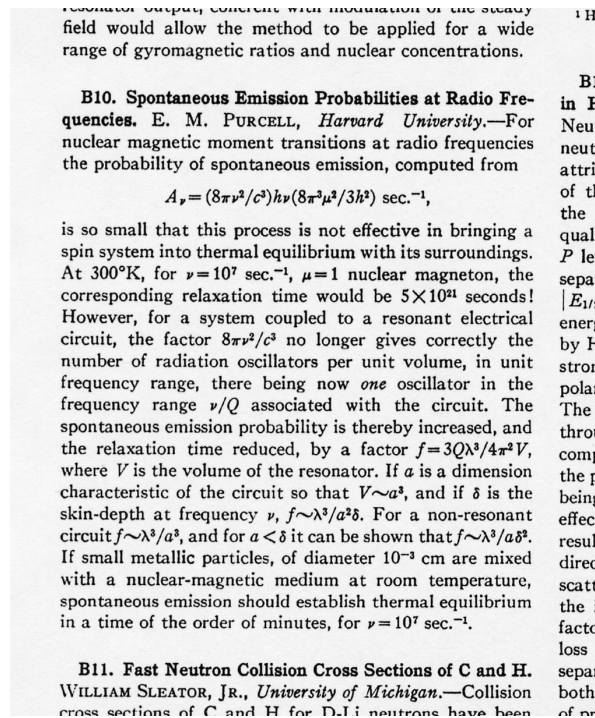


Figure 1.1: Purcell's original paper on enhanced spontaneous emission in a proceedings of the American Physical Society, Phys. Rev. **69**, 681 (1946)

1 Introduction

the Purcell effect has a different implication: it is the basis for an interface of atomic and optical quantum information (QI) for realising a quantum network.

This work reports on an experiment where a single ion has been deterministically coupled to a single mode of the electromagnetic field inside a cavity and exhibiting the Purcell effect - small in magnitude but in the purest implementation. The significance of such a system in the context of modern physics is described in the following historic overview.

1.1 Single Particle Experiments

Single particle experiments are, in fact, relatively young. The first experiment with a single particle was reported in 1973 [2] where a single electron was trapped in a Penning trap. The first single ion was trapped in 1980 in Heidelberg [3]. In the following years, the experimental control on the single particle level was refined by new techniques, e.g. laser cooling, and technological advances of laser sources and stabilisation. These experiences were the foundation for single particle experiments becoming the model system for proof-of-principle experiments in the emerging field of quantum information processing (QIP) in recent years.

In classical information theory the basic carrier of information is the bit which can take two values 0 or 1 typically realised as two different electrical potentials. It has been pointed out already by Feynman in 1982 [4] that if a quantum mechanical (QM) 2-level system would be used to encode and process information, interesting computational possibilities would emerge. The unit of information is then called quantum bit or qubit and is encoded in a coherent superposition of, for example, two atomic levels. The power of the QM version of the bit stems from the superposition principle and the notion of entanglement. The latter is a pure QM feature that has no classical counterpart. The concept entanglement is one the strangest consequences of QM that has raised many discussions in the early days of QM, the most prominent between Bohr and Einstein. A quantitative treatment is still subject of current theoretical research (see for example reference [5]). Originally, Feynman suggested to use such a quantum computer (QC) to simulate large quantum systems [4]. Because at that time any experimental realisation was far out of reach it remained a pure concept at first. It was not until the early 1990's that other useful proposals were brought forward that demonstrated the real power of the QC and created a new field of research in quantum information. In 1992 Deutsch and Josza formulated a problem that could be solved more efficiently on a QC [6]. Two years later Shor [7] proposed the first quantum algorithm of practical interest. His algorithm allows the factorisation of large prime numbers much faster than any known classical version on a classical computer. Another proposal was Grover's search algorithm [8] for searching large databases more efficiently than its classical counterpart. Especially Shor's proposal gave the field of quantum information high practical relevance and attraction. The main reason is that

classical cryptography and hence personal and national security is based on the very fact that factorising sufficiently large prime numbers, the basis of present encryption methods, is intractable on classical computers.

Various proposals for the physical realisation of QC have been put forward [9]. One promising realisation are strings of trapped ions [10] which can meet the necessary experimental requirements for QC, known as the DiVincenzo criteria [11]. Using a single trapped calcium ion the Deutsch-Josza algorithm has recently been implemented [12]. Also two-ion entangling operations such as the universal controlled-NOT operation (proposed 1995 [10]) have been demonstrated in ion-traps [13, 14]. The most recent milestone was the impressive achievement of quantum teleportation of an atomic state [15, 16]. These developments show that the ion trap realisation at this stage is best suited at least for proof-of-principle experiments.

1.2 CQED Experiments in Perspective

Experiments in the context of CQED have been realised using various different physical implementations foremost in atomic and solid state physics. The aim of this section is to introduce and compare these different approaches and to point out their respective strengths and limitations.

In atomic physics the first experiments were done in the 1980's using thermal molecular [17] and atomic beams [18]. In the microwave regime Rydberg atoms became the workhorse of CQED because of their large dipole moments and the availability of superconducting high-Q cavities allowing a strongly coupled system. For example, enhanced spontaneous emission was first revealed in such a system [19], and in a similar setup a one-atom maser was realised [20]. Inhibited spontaneous emission was also first observed in Rydberg atoms [21] after the proposal of Kleppner [22]¹.

Experiments with single atoms in the *optical* domain were first realized by Heinzen *et al.* [24]. They measured both enhanced and inhibited emission rates² of a thermal beam of Ytterbium atoms traversing a confocal optical cavity. Attenuated atomic beams with single atoms in the cavity at a time have further shown interesting atom-cavity effects, like normal modesplitting [25, 26]. The experimentally more demanding optical analogue of the famous one-atom maser (then dubbed microlaser) was also demonstrated in such a system [27].

The development of laser cooling and trapping of neutral atoms refined these experiments since the atoms could be delivered into smaller volume cavities in a more controlled way: by dropping them from a Magneto-Optical Trap (MOT) [28] or pushing them from below in an atomic fountain [29]. From the cavity transmission signal the transit and even the trajectory of a single atom could be inferred. Using this signal

¹The same effect was also observed about the same time in the cyclotron motion of a single trapped electron in a Penning trap [23].

²The relative modification of the emission was +1.6%/-0.5%, respectively.

1 Introduction

the cavity field itself could be used to trap and cool single atoms for up to 3 seconds [30, 31]. Recently, it has been achieved to guide atoms in a dipole trap into the cavity on an atomic 'conveyor belt' [32]. Localisation of the atoms seems to be the highest refinement of neutral atom CQED experiments. This, of course is the strength of trapped ion systems, where localisation of the ion, i.e. its wavepacket is much smaller than the optical wavelength. This has been used to map the standing wave inside an optical resonator [33, 34] (see also chapter 6.1.2 in this work).

An alternative approach to CQED has emerged in solid state physics since the 1990's. The rapid advance of semiconductor technology enabled the production of nanostructures from 2-D quantum wells to 0-D quantum dots (QD). A quantum dot is a small volume (few ten nanometers) semiconductor material embedded in another semiconductor environment resulting in novel properties like discrete energy levels due to its reduced dimensions. The electronic excitation (exciton) can be tailored to have only 2 bound levels. That is why a QD is also called 'artificial atom'. The same technological control of semiconductor growth and etching methods allows the fabrication of high-Q cavity structures in various designs, for example planar Bragg-reflector cavities, micro discs and -pillars and recently photonic-crystal defect cavities. These ingredients make CQED with quantum dots a promising field in the future.

A first success of semiconductor quantum optics was the observation of normal mode splitting in a quantum well coupled to a Bragg reflector microcavity [35]. Altered spontaneous emission has been observed as early as 1988 [36] in double heterostructures but the first clear demonstration of the Purcell effect in QD's was presented in 1998 by Gérard *et al.* [37]. They measure a 5-fold enhancement of the spontaneous emission rate of an ensemble of QD's coupled to a planar cavity in a micro pillar. The emission rate is determined by time resolved photoluminescence detection. In an improved system with a microdisc cavity enhancements of up to a factor of 12 have been reported [38]. An alternative measurement approach for the spontaneous emission rate is pump-power dependent cw photon correlation of the photoluminescence. This has been applied by Kiraz *et al.* [39] where a *single* QD³ coupled to a microdisc cavity has exhibited a 6-fold exciton lifetime reduction. There, also the ability to tune the QD's resonance frequency has been demonstrated. Finally, a factor of 9 in the emission enhancement has been achieved in QDs in a photonic-crystal defect cavity [41]. A remotely related approach to observing CQED effects that is worth mentioning here is doped microspheres [42] and nanocrystals on microspheres [43].

An overview over the relevant different systems is illustrated in fig.1.2. The picture attempts to summarise in one view the respective strengths and limitations of experimental approaches to CQED. However, the most important question is, as to which goal these measures refer. All techniques have equally revealed CQED effects and have confirmed the theory, certainly one aim of experimental physics. On the other hand, as noted in the introduction, one key role of CQED is that of an atom-photon interface in

³See also reference [40]

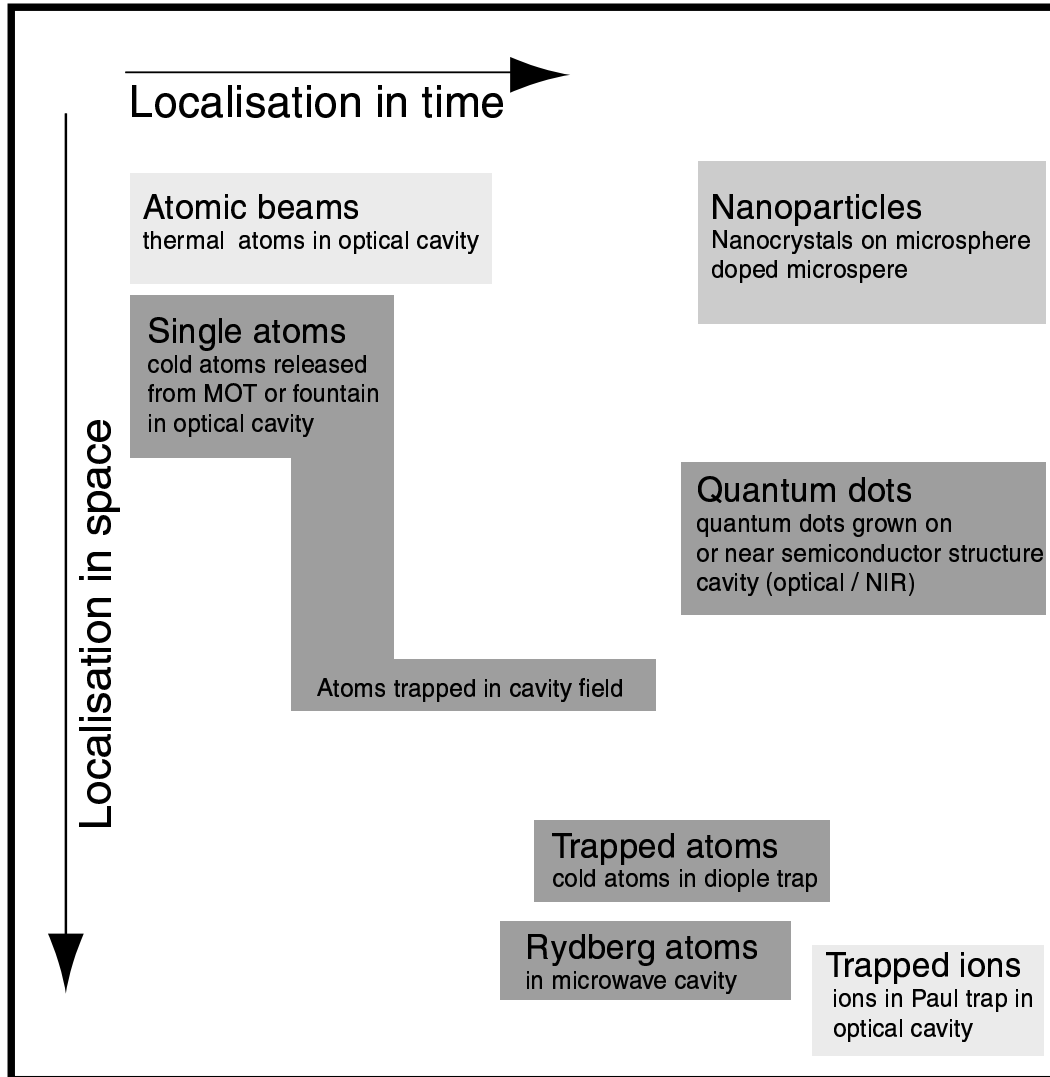


Figure 1.2: Schematic comparison of various physical implementations of CQED experiments with respect to deterministic cavity coupling. Spatial localisation refers to the coupling control, i.e. how well can the particle be placed with respect to the cavity mode. Temporal localisation is related to interaction time. The grey shade of the boxes indicates the achieved coupling strength (darker = stronger).

quantum information processing. The key requirement is deterministic coupling, both in space and time. In that sense the trapped ion system is the ideal system where qubits can be placed at specific points in the cavity mode. Unfortunately, the coupling strength is technically still very limited (c.f. sections 2.3 and 3.1.2). The overall

1 Introduction

technical complexity is also manifest in that the above mentioned experiments are not only very recent but also unique. With cold atoms, Rydberg atoms or quantum dots strong coupling is accessible but other drawbacks are apparent. In the first two cases the interaction times⁴ have been increased but e.g. lifetimes even in a dipole trap never reach the ion trap order of magnitude. With QDs exact positioning of a quantum dot with respect to the cavity mode has been the main drawback. While the localisation is ideal the spatial and spectral overlap is not always deterministic. The best suitable quantum dots have to be selected for the experiment. This system, however, has the huge advantage that nanotechnology is still growing fast. In addition, it has the best scaling properties which makes it a promising candidate in the future for beyond proof-of-principle experiments. Recently, proposals have been put forward to combine the advantages of both atomic and solid state systems in a hybrid system [48], an idea which might be extended to CQED experiments.

This thesis is organised as follows: Chapter 2 provides some theoretical background of atom-field interaction and spontaneous emission. In chapter 3 the experimental set-up is described and some operational principles are outlined. Chapter 4 is an introduction to the general experimental tools and methods along with some important results which form the prerequisites for the following experiments. In chapter 5 the new lifetime measurement technique is introduced along with the results, which are analysed and discussed. The CQED measurement, the observation of cavity enhanced spontaneous emission is found in Chapter 6. All results are summarised in chapter 7 which concludes and provides an outlook. The appendices include some practical technicalities of the experiment and statistical methodology used for the lifetime analysis. Finally, the two publications comprising the important results are appended.

⁴It should be noted that interaction time is much less a problem in the microwave regime: the transit time through the large mode volume of a millimeter wavelength cavity field is much longer than the coupling time scale in the strong coupling regime.

2 Theory of Spontaneous Emission

In this chapter, the theoretical foundation for spontaneous emission of excited atomic states is presented. Starting from general semi-classical atom-field interaction the concept of the quantum vacuum is introduced. Finally, the way cavities modify the vacuum along with natural atomic properties is discussed. Spontaneous emission is one of the most demanding problems in the study of atom-field interactions, many different approaches were developed and even today conceptual subtleties exist, for example, how to interpret the role of vacuum fluctuations (VF). Here, some of the approaches are discussed with emphasis on the physical concepts as opposed to pure mathematics.

2.1 Approaches to Atom-Field Interaction

A first success in describing atom-field interaction which was consistent with the findings of Planck, i.e. the introduction of light quanta of energy $\hbar\omega$, was achieved by Einstein in 1917. He considered 2-level atoms in equilibrium with a thermal electromagnetic field (blackbody radiation) and found relations for the coefficients of stimulated emission B_{21} and absorption B_{12} and spontaneous emission A_{21} , the so-called Einstein coefficients. Using only the Boltzmann distribution for the ratio of atoms in the excited and ground state (N_2 and N_1) and the energy density of the field $\rho_E(E)$ he derived the relation of spontaneous and stimulated emission coefficients [51]:

$$\frac{A_{21}}{B_{21}} = \frac{\hbar\omega^3}{\pi^2 c^3} \quad (2.1)$$

In the absence of an external field $N_2(t) = N_2(0) \cdot e^{-A_{21}t}$ describes the exponential decay of the excited population N_2 . The density of field modes $\rho(\omega)$ in the interval $[\omega, \omega + d\omega]$ is found by counting states in k-space and converting the sum into an integral over frequency

$$\rho(\omega) = \frac{\omega^2}{\pi^2 c^3} \quad (2.2)$$

The energy density follows from $\rho_E(E) = \langle n \rangle \hbar\omega \rho(\omega)$ where $\langle n \rangle \hbar\omega$ is the average photon energy. The expression for $\rho_E(E)$ equals Planck's formula for the blackbody spectrum. Einstein's model offers a consistent mathematical expression for the decay rate but

2 Theory of Spontaneous Emission

is unsatisfactory, however, in the sense that it is a phenomenological 'postulate' of spontaneous emission. Nevertheless, the coefficients can be calculated in the framework of a semiclassical theory.

2.1.1 Semiclassical Theory

When the full quantum mechanical machinery was developed in the 1920's the problem of spontaneous emission could be tackled in a more rigorous way: In a simple semi-classical theory the atom is treated by standard quantum mechanics whereas the field is still described by the classical Maxwell equations. In perturbation theory the Hamiltonian is conveniently written as a sum of an unperturbed atomic term H_a and an interaction term H_{int} incorporating the atom-field coupling. A quantum state is determined by its (complex) probability amplitudes c_n for a set of basis states φ_n . For the 2-level atom considered here and referring to the quadrupole transition between $S_{1/2}$ and $D_{5/2}$ states at ω_{SD} , the state is written:

$$|\psi\rangle = c_1|\varphi_1\rangle + c_2|\varphi_2\rangle = c_1|S_{1/2}\rangle + c_2|D_{5/2}\rangle \quad (2.3)$$

substituting into the time dependent Schrödinger equation (TDSE) yields two coupled differential equations for the amplitudes [50], e.g. for c_2 :

$$\dot{c}_2 = -\frac{1}{\hbar}\langle S|\tilde{H}_{int}|D\rangle e^{i\omega_{SD}t}c_1 \equiv -\frac{1}{\hbar}|\tilde{H}_{int}|e^{i\omega_{SD}t}c_1 \quad (2.4)$$

For electromagnetic (EM) fields with harmonic time dependence, the transition matrix element of atom-light interaction is of the form: $|\tilde{H}_{int}| = |H_{int}|eE_0\cos(\omega t)$ where $|H_{int}|$ depends on the type of transition. Integrating 2.4 from 0 to t and applying the rotating wave approximation (RWA, see [50]) yields

$$|c_2|^2 = \frac{|H_{int}|^2}{4\hbar^2} \frac{\sin^2[(\omega - \omega_{SD})t/2]}{(\omega - \omega_{SD})^2}. \quad (2.5)$$

For longer times $1/t < (\omega - \omega_{SD})$ the last term can be written in terms of the Dirac delta function $\delta(\omega - \omega_{SD})$ ¹. Considering a continuous density of states $\rho(\omega)$ the total probability of finding the excited state is

$$|c_2|^2 = \frac{1}{2\hbar^2} \int d\omega |H_{int}|^2 t \rho(\omega) \delta(\omega - \omega_{SD}) \quad (2.6)$$

The delta function under the integral is equivalent to the assumption that $|\tilde{H}_{int}(\omega)|$ and $\rho(\omega)$ vary slowly in the vicinity of ω_{SD} . Evaluating 2.6, Fermi's Golden Rule is recovered:

$$\frac{1}{\tau} = \Gamma = \frac{d}{dt}|c_2|^2 = \frac{\pi(eE_0)^2}{2\hbar^2} |H_{int}|^2 \rho(\omega_{SD}) \quad (2.7)$$

¹One definition of the Dirac delta function is: $\delta(\omega - \omega_0) = \frac{2}{\pi} \lim_{t \rightarrow \infty} \frac{\sin^2[(\omega - \omega_0)t/2]}{(\omega - \omega_0)^2 t}$

2.1 Approaches to Atom-Field Interaction

To connect this expression to the Einstein coefficients the monochromatic field strength E_0 must be replaced by an integrated energy density $U(\omega)$ over all frequencies

$$\frac{1}{2}\epsilon_0 E_0^2 = \int d\omega U(\omega) \quad (2.8)$$

where for the vacuum the integral is simply $\hbar\omega\rho(\omega) = (\hbar\omega^3)/(\pi^2c^3)$. Substituting into 2.7 and identifying the stimulated transition rate $B_{21} = \frac{\pi e^2}{\hbar^2\epsilon_0}|\tilde{H}_{int}|^2$ equation 2.1 is recovered.

For the evaluation of 2.7 the matrix element $|H_{int}|$ must be specified. For a quadrupole transition the atomic quadrupole moment \hat{Q} couples to the gradient of the electric field:

$$H_{int} = \hat{Q}\nabla E(t) \quad (2.9)$$

For the transition between the $S_{1/2}, m = -1/2$ and $D_{5/2}, m = -5/2$ Zeeman sublevels the matrix element computes to [113]:

$$|H_{int}| = |\langle S_{1/2} | (\mathbf{r}\cdot\mathbf{e})(\mathbf{r}\cdot\mathbf{k}) | D_{5/2} \rangle| \quad (2.10)$$

where \mathbf{r} is the operator describing the position of the valence electron relative to the atomic center of mass and \mathbf{k} and \mathbf{e} describe the light's direction and polarisation, respectively. The matrix element is related to the coupling parameter, i.e. the Rabi frequency Ω_0 by:

$$\Omega_0 = \frac{eE_0}{2\hbar}|H_{int}| \quad (2.11)$$

2.1.2 Jaynes-Cummings Model

For a full quantum model the field must be quantised as well. This was considered by Jaynes and Cummings [54] after whom the well known model was named which has become the 'theoretical workhorse' in quantum optics. In this formalism the Hamiltonian for a 2-level atom in a quantised EM-field is written as

$$H = \underbrace{\frac{1}{2}\hbar\omega_a\sigma_z}_{\text{atom}} + \underbrace{\hbar\omega_k aa^\dagger}_{\text{field}} + \underbrace{\hbar g(a^\dagger\sigma_- + a^-\sigma_+)}_{\text{interaction}} \quad (2.12)$$

σ_z is one of the Pauli spin operators and can be written in terms of the commutator of the spin flip pseudo-operators σ_- and σ_+ , $\sigma_z = [\sigma_-, \sigma_+]$. The field operators a and a^\dagger are also called photon annihilation and creation operators and obey the usual bosonic commutation relations $[a, a^\dagger] = 1$. The atom-field coupling is here denoted by g which is related to equation 2.11 by $g = \frac{1}{2}\Omega_0$. The RWA is applied by omitting terms like $a^\dagger\sigma_+$ and $a^-\sigma_-$. In the Heisenberg picture the TDSE for the operators becomes $i\hbar\frac{d}{dt}A = [H, A]$ and one finds for the equation of motion for the atomic operator

$$\ddot{\sigma}_z = \Omega^2\sigma_z \quad (2.13)$$

2 Theory of Spontaneous Emission

This yields an oscillatory solution which describes a harmonic exchange between atom and field. The frequency Ω is the generalised Rabi frequency that is encountered frequently in quantum optics; $\Omega = \sqrt{\Omega_0^2 + \Delta^2}$. The Hamiltonian 2.12 can be readily modified to be applied to many other problems in quantum optics, e.g. for treating the quantised motion of a cooled, trapped atom which is used in chapter 4.3. The Hamiltonian then includes the phonon operators, a and a^+ of the same form as the photon operators, for the vibrational modes of the atom, and one finds solutions for the quantised Rabi frequencies depending on the motional state.

In section 2.3 the Jaynes-Cummings model is applied to atom-cavity field coupling where g then depends on the cavity mode volume.

One of the consequences of formally quantising a harmonic oscillator is its zero-point energy $E_0 = \frac{1}{2}\hbar\omega_k$ corresponding to half an excitation quantum. This means that even for a zero EM field there remains a virtual field which is referred to as quantum vacuum consisting merely of 'vacuum fluctuations' (VF). Mathematically, this translates to the expectation value of the electric field operator in vacuum being zero: $\langle vac|\hat{E}|vac\rangle = 0$, whereas the variance remains nonzero (since $\langle vac|\hat{E}^2|vac\rangle \neq 0$).

The concept of VF was quickly regarded to be responsible for spontaneous emission [55, 56]. It was, however, proven to be an over-simplified picture.

2.2 Spontaneous Emission in the Weisskopf-Wigner Approximation

The first satisfactory mathematical account for the irreversible exponential decay behavior of excited atomic levels was presented by Weisskopf and Wigner in 1930 [55].

In terms of the chosen basis $\varphi_1 = |D, 0\rangle = |excited\ atom, vacuum\rangle$ and $\varphi_2 = |S, k_\alpha\rangle = |atom\ in\ groundstate, one\ photon\ in\ kth\ mode\rangle$ the quantum state vector in the Schrödinger picture is written as [51]

$$\psi = A(t)e^{i\omega_{SD}t}|D, 0\rangle + B(t)e^{i\omega_\alpha t} \sum_{\alpha} |S, k_\alpha\rangle \quad (2.14)$$

where φ_1 describes the state where the atom is in the excited state and the EM field in the ground state (vacuum state) and φ_2 is the atomic ground state and a photon in the mode with wave vector k_α , frequency ω_α and polarisation vector \hat{e}_α where the index α runs over all frequencies and polarisations. The multimode version of the Hamiltonian 2.12 is

$$H = \frac{1}{2}\hbar\omega_{SD}\sigma_z + \hbar \sum \omega_k a_\alpha a_\alpha^+ + \hbar \sum g_\alpha (a^+ \sigma_- + adj.) \quad (2.15)$$

Inserting into the TDSE one obtains two coupled differential equations for the ampli-

2.2 Spontaneous Emission in the Weisskopf-Wigner Approximation

tudes $A(t)$ and $B(t)$. The time dependent amplitude for φ_1 is

$$\dot{A}(t) = - \sum_{\alpha} g_{\alpha}^2 \int_0^t dt' e^{-i(\omega_{SD} - \omega_{\alpha})(t-t')} A(t') \quad (2.16)$$

The essential approximation used here is to set $\int_0^t dt' A(t') = A(t) \int_0^t dt'$. This is sometimes called Markov approximation and means that the amplitude is independent of earlier times, in other words, it has 'no memory'. Equation 2.16 contains a typical QED integral which can be replaced for sufficiently long times ($\omega_0 t \gg 1$) using Cauchy's 'Residuensatz':

$$\int dt' e^{-i(\omega - \omega_0)(t-t')} = -iP \left(\frac{1}{\omega - \omega_0} \right) + \pi \delta(\omega - \omega_0). \quad (2.17)$$

Then after turning the sum over modes into an integral 2.16 can be written as

$$\dot{A}(t) = -(\Gamma/2 - i\Delta)A(t) \quad (2.18)$$

to reveal an exponential decay of the excited state probability: $|A(t)|^2 = e^{-\Gamma t}$. From equations 2.16 and 2.17 the decay constant is

$$\Gamma = \frac{e^2 \omega_{SD}^3}{\hbar \pi c^3 \epsilon_0} |H_{int}|^2 \quad (2.19)$$

which recovers expression 2.7 when one uses equation 2.8 again. The other important result of 2.18 is the implication of the imaginary part $i\Delta$ which describes a frequency shift Δ of the upper level.

There remained, however, several puzzles, concerning the interpretation of the physical origin of spontaneous decay or the respective roles of VF, the quantum point-of-view and radiation reaction (RR)², the classical point-of-view. This discussion has been emphasized by Milonni [52](and references therein) and others [53]. Note that the issue of vacuum fluctuations is not explicit in the Weisskopf-Wigner-formalism using the Schrödinger picture. In the Heisenberg picture the equations of motion for the atomic spin operators and the field operators are integrated. In analogue to equation 2.18 one finds the time derivative for the expectation value of the atomic spin operator σ_z . It turned out that the respective ordering of field and atomic operators plays the crucial role in the interpretation of the origin of spontaneous decay, see e.g.[52]. For example, the atomic operator equation reads

$$\dot{\sigma}(t) = -i\omega_0 \sigma + g(a + a^+) \sigma_z \quad (2.20)$$

²In classical electrodynamics RR accounts for the back action of the radiated field onto the emitting (point) particle.

2 Theory of Spontaneous Emission

The solution for the field operator $a(t)$ can be decomposed into a sum of a vacuum part and a source field created by the atomic radiation $a'(t)$.

$$a(t) = a(0)e^{i\omega_\alpha t} + a'(t) \quad (2.21)$$

The second term of 2.20 is not unique with respect to ordering of operators. It could also be written as, for example $g(\sigma_z a + a^\dagger \sigma_z)$ which is called 'normal ordering'. Then only the source term $a'(t)$ contributes to the expectation value $\langle vac | \sigma_z | vac \rangle$ and the decay would be interpreted to be solely the result of radiation reaction. Other orderings yield contributions from both, VF and RR.

2.3 Cavity QED and The Purcell Effect

In the expression for the decay rate 2.19 a spectral mode density is implicit. It would therefore not come as a surprise if the decay is modified by changing the mode density of the vacuum with specific boundary conditions. In a rather brief but often cited publication, Purcell [1] was the first to predict that for a nuclear spin system coupled to a resonant electrical circuit the spontaneous decay at radio frequencies could be enhanced by a factor of $f = 3Q\lambda^3/4\pi^2V$ where $Q(= \omega/\delta\omega)$ is the resonator's quality factor and V is it's mode volume. For a confocal optical cavity the derivation differs slightly. The decay rate into the cavity mode is modified by the response function $t(\omega)$ which describes the enhancement of the intra-cavity field³

$$\frac{\gamma}{\gamma_{\text{free}}} = t(\omega) \simeq \frac{F}{\pi} \frac{1}{1 + (F/\pi)^2 \sin^2(\omega L/c)} \quad (2.22)$$

which has a maximum

$$\frac{\gamma_{\text{enh}}}{\gamma_{\text{free}}} = \frac{F}{\pi} \quad (2.23)$$

The total decay rate Γ_{enh} into solid angle $\Delta\Omega$ that the cavity mirrors subtend is

$$\Gamma_{\text{enh}} = \Gamma_{\text{free}} + \gamma_{\text{enh}} = \Gamma_{\text{free}} \left[1 + \frac{F\Delta\Omega}{4\pi^2} \right] = \Gamma_{\text{free}} \left[1 + \frac{F}{4\pi^2} \frac{\lambda^2}{w_0^2} \right] \quad (2.24)$$

$$\Gamma_{\text{enh}} = \Gamma_{\text{free}} [1 + f] \quad (2.25)$$

To improve this naive first calculation the geometry of the radiation pattern must be accounted for. So we write $f = \alpha F \lambda^2 / w_0^2$. For a quadrupole transition with $\Delta m = 2$

³This is related to the ratio of cavity to free space density of modes $\rho_{\text{cav}}(\omega)/\rho_{\text{free}}(\omega)$. Around the resonances $t(\omega)$ can be written as a Lorentzian.

2.3 Cavity QED and The Purcell Effect

the geometric factor turns out to be $\alpha = 5/\pi^3$ [118]. In terms of Q, λ and V the expression for f for a quadrupole transition becomes $f = 5Q\lambda^3/32\pi^3V$.

Within the Jaynes-Cummings formalism from section 2.1.2 the enhanced decay rate can be derived more formally. The effective (non-Hermitian) Hamiltonian for the coupled atom-cavity system is modified from 2.12 and includes a loss term for both atom (decay constant γ_{\perp}) and cavity (decay constant κ)

$$H_{\text{eff}} = H_{\text{acf}} - i\hbar(\gamma_{\perp}\sigma_{+}\sigma_{-} + 2\kappa a_c a_c^{\dagger}). \quad (2.26)$$

Using the same basis states as in the Weisskopf-Wigner approach $|D, 0\rangle$ and $|S, k_{\alpha}\rangle$ and solving the TDSE we find the time dependent coefficients $A(t)$ and $B(t)$ [51]:

$$A(t) \sim e^{\lambda_{+}t}; B(t) \sim e^{\lambda_{-}t} \quad (2.27)$$

where the eigenvalues are

$$\lambda_{\pm} = -\frac{\gamma_{\perp} + \kappa}{2} \pm \sqrt{\left(-\frac{\gamma_{\perp} + \kappa}{2}\right)^2 - g^2} \quad (2.28)$$

The dynamics now depends on the system's parameters $(\gamma_{\perp}, \kappa, g)$. For the case where the cavity interaction is dominated by dissipation, i.e. $(\kappa \gg g^2/\kappa \gg \gamma_{\perp})$ the exponents λ_{\pm} are real and the system is damped which is called the '**bad cavity regime**'. This is the relevant regime realised in the cavity experiment described in this work. The eigenvalues can then be approximated by

$$\lambda_{+} \approx -\left(\gamma_{\perp} + \frac{g^2}{\kappa}\right) = -\gamma_{\perp}(1 + 2C) \quad (2.29)$$

$$\lambda_{-} \approx -\left(\kappa - \frac{g^2}{\kappa}\right) \quad (2.30)$$

where $C = f/2 = \frac{g^2}{2\gamma_{\perp}\kappa}$ is defined as the cooperativity parameter. When the expressions for g, κ and γ_{\perp} are substituted one finds again the expression 2.24. Because of the weak atom-cavity coupling the new eigenstates retain their character to a large extent: λ_{+} corresponds to an 'atom-like' state consisting mainly of $|e, 0\rangle$, accordingly λ_{-} corresponds to a cavity state. The important result from 2.29 is that the atomic decay occurs at a faster rate⁴ expressed by the Purcell factor $F = (1 + 2C)$ or a relative shortening of $\beta = 2C/(1 + 2C)$. Another consequence is that the geometry of the emission is modified: the enhanced decay (fraction β) occurs into the cavity mode, that is, for large Purcell factors the emission pattern becomes one-dimensional [25].

For the quadrupole transition we obtain:

$$g = \frac{e}{2\hbar}|H_{\text{int}}|\sqrt{\frac{2\hbar\omega}{\epsilon_0 L \pi w_0^2}} = \frac{eE_p}{2\hbar}\sqrt{2}|H_{\text{int}}| \equiv \Omega_0/2 \quad (2.31)$$

⁴Similarly, the cavity decay rate is modified.

2 Theory of Spontaneous Emission

where the 'electric field per photon'[51]

$$E_p = \sqrt{\frac{\hbar\omega_c}{\epsilon_0 V}} \quad (2.32)$$

has been introduced. L and w_0 are the length and waist of the cavity mode, respectively, and determine the cavity mode volume $V = L\pi w_0^2$. Comparing equations 2.11 and 2.32: E_p replaces the field amplitude E_0 , the reason why $2g$ is also called the vacuum Rabi frequency Ω_0 . For the relevant S-D transition, the atom-cavity coupling is evaluated to

$$g = \sqrt{\frac{5\gamma_\perp c\lambda^2}{2\pi^2 V}} \quad (2.33)$$

Considering the system's parameter $(g, \kappa, \gamma) = 2\pi(89, 10^5, 0.16)\text{s}^{-1}$, c.f. chapter 3, the value of C_0 is calculated to $C_0 = 0.51$ and the maximal decay enhancement is expected to be around two. Note that for applications such as the quantum information interface or a single photon source the cavity decay *must* be set the fastest timescale ('bad' cavity) because once the photon is emitted into the cavity it must be able to leak out before being absorbed again by the atom.

If $g \gg \kappa, \gamma_\perp$, i.e. the cavity coupling is the dominant parameter, then the eigenvalues are imaginary and the system shows oscillatory behavior: the energy can be exchanged periodically between atom and cavity field. This so-called 'strong coupling regime' is realised, for example, in the neutral atom experiments in references [28, 30, 31].

The Jaynes-Cummings model can also be modified if the quantum state is described by a density matrix ρ rather than a state vector to incorporate the incoherent process. The TDSE for operators is then called the master equation:

$$\dot{\rho} = \frac{1}{i\hbar}[H, \rho] + L\rho \quad (2.34)$$

where L is the so-called Liouvillian of the system:

$$L\rho = \gamma([\sigma_+\sigma_-, \rho] + 2\sigma_+\rho\sigma_-) \quad (2.35)$$

This models a small quantum system coupled weakly to a large reservoir or bath. The reservoir incorporates all empty modes of the EM field. The modes are uncoupled and hence it is sometimes expressed as the reservoir having no 'memory'. This assumption is also implicit in the Weisskopf-Wigner method.

3 Experimental Set-Up

The whole experimental set-up is a complex entity consisting of a detailed trap-cavity apparatus in a UHV chamber, the heart of the experiment, and various laser sources, optical components and electronics. Since the experiment has been developed over many years most components have been described in detail elsewhere (in other PhD theses produced in this group). References are given accordingly.

The apparatus described here has been set up by A.B. Mundt within his PhD work where it has also been described in more detail [113]. First, the basic operational principles will be presented followed by the technical implementation.

3.1 General Principles

3.1.1 Ion Traps

Since electric fields obey the Laplace equation $\Delta\Phi = 0$, confinement of a charged particle is not possible in static electric fields alone. One possible trick is to use a time dependent field, the idea of dynamical electromagnetic confinement. Effectively, an appropriately varying quadrupole field generates a pseudo-harmonic potential for confinement in all three dimensions. First a 2-dimensional experimental implementation was realised by Wolfgang Paul in 1953 intended for mass-spectrometry. A little later, the same principle led to the radio frequency (RF) Paul trap [57, 58] from which the modern traps differ only in technical refinements like, for example, miniaturisation and more complex electrode structures. The mathematical description, however, is essentially the one of the original mass spectrometer.

Consider a quadrupole potential composed of static and time dependent part:

$$\Phi(x, y, z, t) = \frac{1}{2}[U + V \cos(\Omega_{RF}t)][\alpha x^2 + \beta y^2 + \gamma z^2] \quad (3.1)$$

The restrictions for the coefficients (α, β, γ) then follow from the Laplace equation:

$$\alpha + \beta + \gamma = 0 \quad (3.2)$$

which illustrates the static instability: at least one of the coefficients must be negative yielding a 'saddle' potential.

3 Experimental Set-Up

The equation of motion (in the x-direction) for the trapped particle is derived from 3.1:

$$\ddot{x} = \frac{-Q}{m} \frac{\partial \Phi}{\partial x} = \frac{-Q\alpha}{m} [U + V \cos(\Omega_{RF}t)]x \quad (3.3)$$

which can be cast into a standard mathematical form, the so-called Mathieu differential equation:

$$\frac{d^2x}{d\xi^2} + [a_x - 2q_x \cos(2\xi)]x = 0 \quad (3.4)$$

using the substitutions

$$\xi = \frac{1}{2}\Omega_{RF}t, \quad a_x = \frac{4QU\alpha}{m\Omega_{RF}^2}; \quad q_x = \frac{2QV\alpha}{m\Omega_{RF}^2} \quad (3.5)$$

where Ω_{RF} is the radio frequency (RF) trap drive, Q and m the ion's charge and mass, and α depends on the trap geometry. The exact solution to 3.4 is quite complicated and can be found e.g. in references [59] and [60]. The lowest order approximation is already satisfactory in most cases and describes oscillatory motion:

$$x = A_x \cos(\omega_x t + \phi) \left(1 + \frac{q_x}{2} \cos(\Omega_{RF}t)\right) \quad (3.6)$$

which can be decomposed into a harmonic or secular motion at frequency ω_x (the trap frequency) and a fast, driven amplitude modulated 'micromotion' at the trap drive frequency Ω_{RF} . In the experiment the micromotion is minimised to the largest possible extent by shifting the ion into the node of the RF, see section 4.1, and is often neglected (secular approximation). The ion can then be regarded as effectively being confined in a pure harmonic pseudo-potential. For a ring Paul trap which is cylindrically symmetric about the z-axis (normal to the ring) the trap frequencies (radial and axial) are given by

$$\omega_i = \beta_i \frac{\Omega_{RF}}{2} \quad \text{and} \quad \beta_i = \sqrt{a_i + \frac{q_i^2}{2}}. \quad (3.7)$$

where the trap parameters a and q are

$$\begin{aligned} a_x = a_y = a_r &= -\frac{8QU}{m(r_0^2 + 2z_0^2)\Omega_{RF}^2}, & a_z &= -2a_x, \\ q_x = q_y = q_r &= \frac{4QV}{m(r_0^2 + 2z_0^2)\Omega_{RF}^2}, & q_z &= -2q_x, \end{aligned} \quad (3.8)$$

However, stable solutions exist only for certain values of a and q . Here, the trap is operated at parameters $a \approx 0$ and $q \approx 0.5 - 0.6$ which are well in the first stable region.

Besides the ring trap various other designs exist to realise a quadrupole field. Originally, the quadrupole mass filter consisted of four parallel hyperbolic rods. Two endcaps at a positive DC-voltage achieve axial confinement which converts the mass filter into a linear Paul trap. Such a trap is suited in particular for trapping large ion crystals or strings of few ions as required for QC. The ring trap design has only one point in space with no RF present (point-symmetric potential) and is therefore most suitable for single ion experiments. It has also other advantages such as simpler design than linear traps at similar trap frequencies and better optical access.

The other concept for electromagnetic ion confinement is the Penning trap which is based on a combination of a static electric quadrupole field and a static magnetic field.

As a final note: the principle of ion traps is extensively discussed in the recommendable book by Ghosh [59] and appears also in all PhD theses produced in this group, e.g. [113–119].

3.1.2 Optical Resonators

The concept of an optical resonator is that light is reflected back and forth between two spherical mirrors¹ mapping the mode onto itself after a roundtrip. Some spectral, temporal and spatial properties of the resonator mode are discussed in the following. One consequence of multiple reflections is wavelength selectivity due to interference

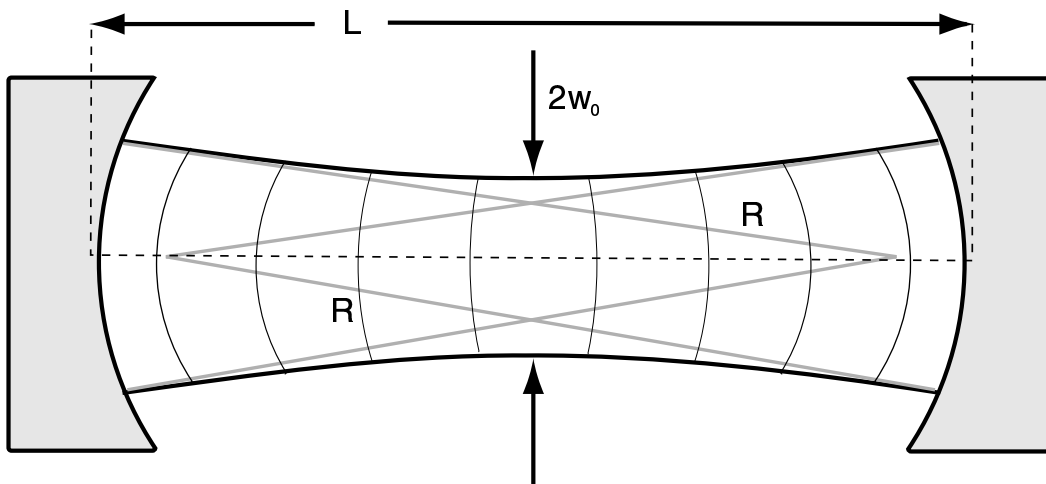


Figure 3.1: Sketched cavity mode and geometric parameters. The cavity length L is close to the mirror curvature R (near-confocal cavity). The fundamental Gaussian mode TEM_{00} is characterized by the waist w_0 . The curved lines indicate the mode's phase fronts.

¹Various other types exist, e.g. ring cavities with three or more mirrors

3 Experimental Set-Up

of the reflected fields: The cavity can only sustain certain frequencies that fulfil the resonance condition, the principle of the Fabry-Perot filter. The intensity transmission function (the square of the sum of the reflected field phasors) looks as follows:

$$I(\omega) = \frac{I_{max}}{1 + (2F/\pi)^2 \sin^2(\pi\omega/\nu_{FSR})} \quad (3.9)$$

For high mirror reflectivities this function has periodic Lorentzian peaks with linewidth $\delta\omega$ separated by the so-called free spectral range (FSR) ω_{FSR} . The ratio is the finesse of the cavity

$$\frac{\nu_{FSR}}{\delta\nu} = F \quad (3.10)$$

which depends on the mirror reflectivity R

$$F = \frac{\pi\sqrt{R}}{1-R} \quad (3.11)$$

whereas the FSR only depends on the resonator length:

$$\nu_{FSR} = \frac{c}{2L} \quad (3.12)$$

which corresponds to the reciprocal of the time for a complete roundtrip for the light between the two mirrors. Transmission and absorption of the mirrors are losses that cause the light intensity in the cavity to decay exponentially $I(t) = I_0 e^{(-t/\tau)}$. The cavity decay rate κ (the decay of the field) is related to the decay time τ and the cavity linewidth by:

$$\kappa = \frac{1}{2\tau} = \pi\delta\nu \quad (3.13)$$

Spatially, the allowed transverse modes are solutions of the paraxial Helmholtz equation of which the Gaussian mode, the TEM₀₀ mode, is the simplest and most important case here. It is characterised by a waist w_0 (see also fig. 3.1) depending on the cavity configuration [61]:

$$w_0^2 = \lambda/2\pi \sqrt{L(2R-L)} = \frac{\lambda b}{2\pi} \quad (3.14)$$

where the waist is expressed in terms of the wavelength and the confocal parameter b . For a confocal cavity, $L = R$ and

$$w_0 = \sqrt{\frac{\lambda L}{2\pi}} \quad (3.15)$$

From equation 3.14 the waist can be reduced by increasing the cavity length towards $L = 2R$ (concentric cavity) or $L = 0$ (planar cavity), both at the cost of increasing

instability of the resonator. For cavity QED experiments the key parameter is actually the mode *volume* $V = L\pi w_0^2$ which is generally sought to be minimised. The significance of the mode volume will become lucid in section 2.3.

Figure 3.2 shows a photograph of the experimental realisation: the ring trap in the cavity. The cavity mirrors are hidden behind the conical metal caps to protect them from the atomic Calcium beam and to shield the trap from stray charges on the dielectric high reflectivity coatings. The hook shaped electrodes are for compensating stray electric fields which lead to micromotion.

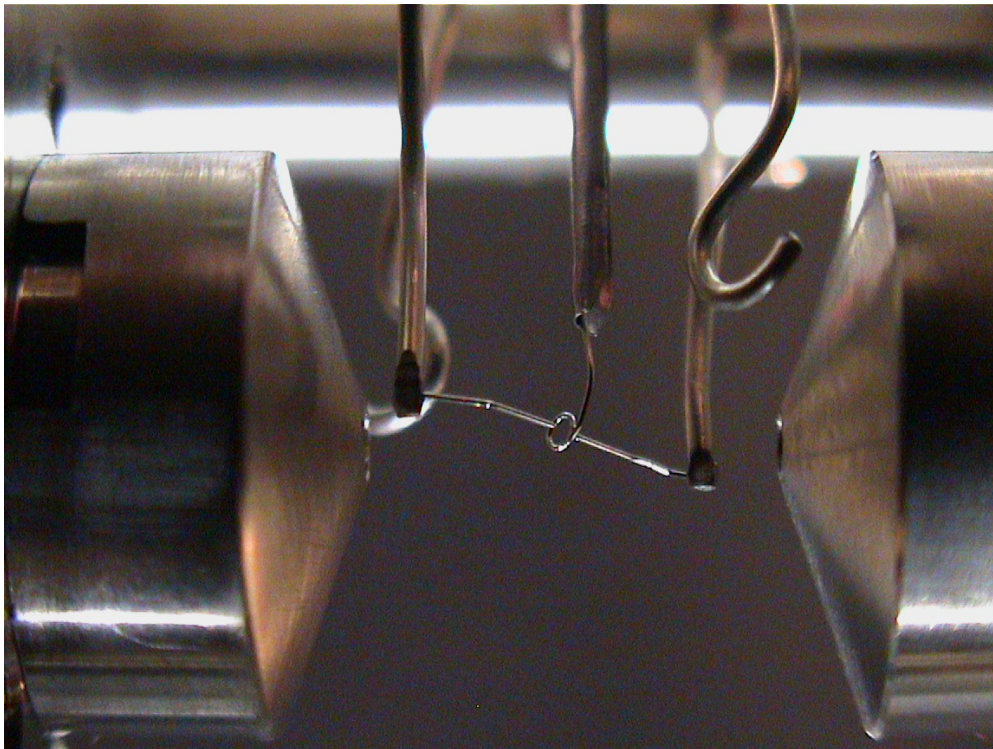


Figure 3.2: The miniaturised Paul trap. The ring electrode (diameter ≈ 1.4 mm) and the endcaps (tip electrodes) are made of molybdenum wire (diameter ≈ 0.2 mm). The hook shaped wires are the compensation electrodes used to shift the ion into the node of the RF field.

3.2 The Trap-Cavity Assembly

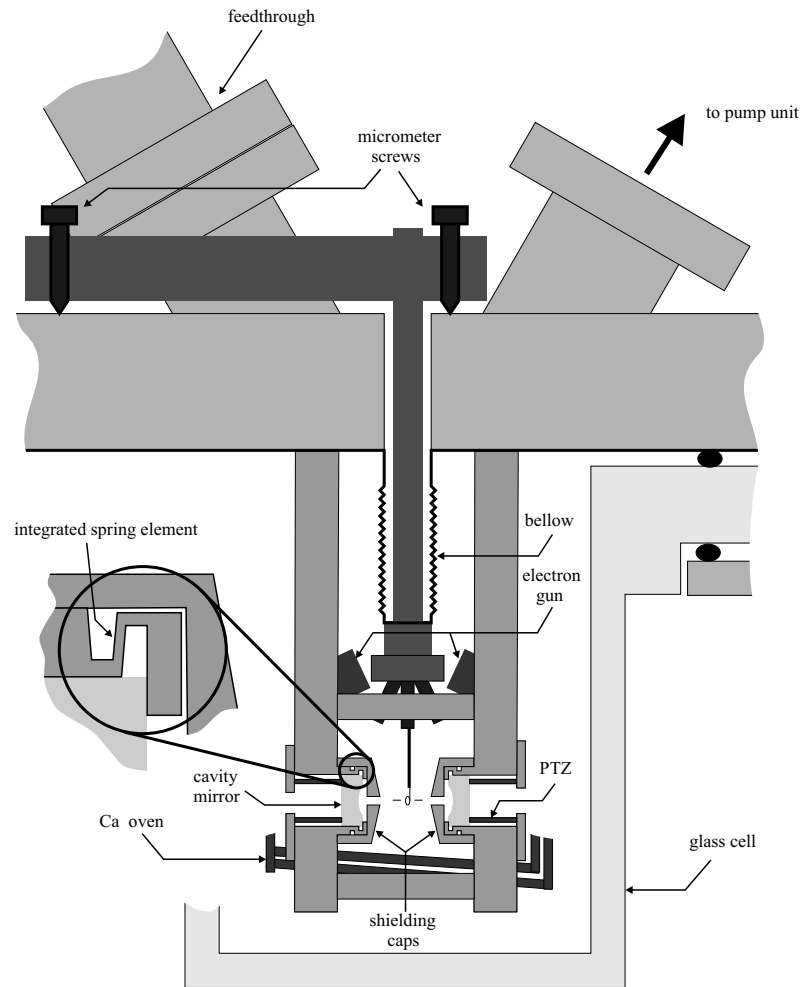


Figure 3.3: Schematic drawing of the trap-cavity assembly inside the vacuum chamber. All components are mounted on a stainless steel baseplate (248 mm in diameter) inside a glass cell for optimal optical access. The glass cell is sealed onto the steel base with helico-flex seals, which initially resulted in vacuum problems. Two flanges are welded onto the baseplate, connecting pump unit and electrical feedthrough to the vessel. The trap can be moved relative to the cavity by micrometer screws. Wiring and details are omitted for clarity. (Drawing reprinted from reference [113].)

3.2 The Trap-Cavity Assembly

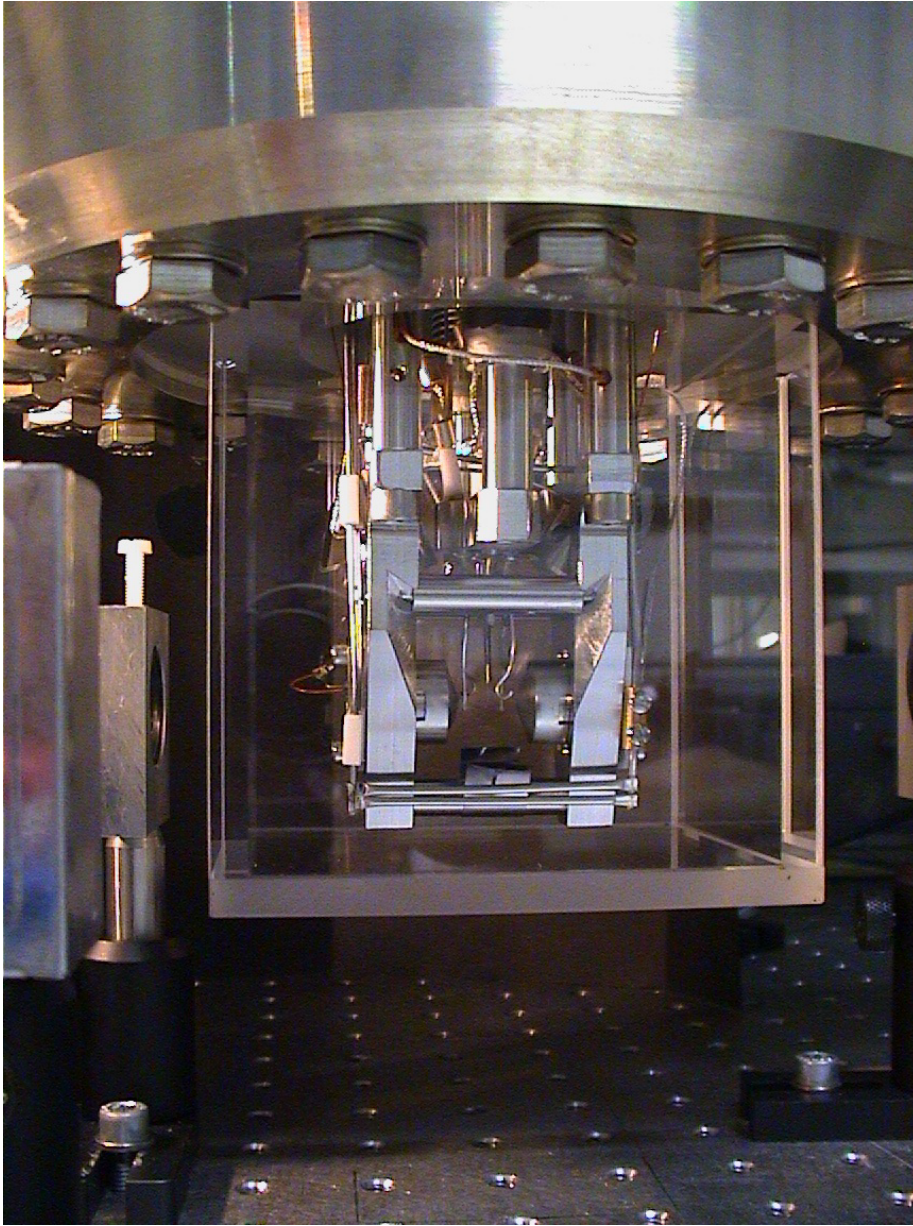


Figure 3.4: Photograph of the assembled experimental apparatus after evacuation and bakeout on the optical table. For good optical access, cavity axis and trap are mounted 94 mm above the optical table. The cuboid glass cell and its flange are visible. At the bottom of the cavity mount, the two Calcium ovens and the aperture for the atom beam are mounted.

3.3 Calcium

Generally, in ion traps charged ions with hydrogenlike electron configuration are best suited (obvious representatives are the alkaline earth metals: Be, Mg, Ca, Sr, Ba, Ra). They all have the same electronic ground state configuration: a valence S-electron around a closed shell in noble gas configuration. The criteria for choosing the best suited ion depend on the application. Possible criteria include transition frequencies, mass and atomic level structure.

Transition wavelengths should be easily accessible with common (commercial) laser sources preferably diode lasers which are relatively cheap and allow a compact experimental set-up. Drawbacks of diode lasers might be limited output power and linewidths and beam profile. The atomic level structure should include features like closed cycles for cooling and long lived states like metastable states or hyperfine splitting. Finally, the natural abundance of the specific element should be high enough to allow easy and efficient loading into the trap.

One special feature of Calcium is that it has a metastable level that is long lived and therefore spectrally narrow. This offers diverse applications in fields such as quantum computation and optical frequency standards. The natural line width of below 1 Hz implies a Q -factor of $\sim 10^{15}$ which could be used in an optical frequency standard [62] potentially improving current microwave based frequency standards by more than an order of magnitude. For the current status of optical frequency metrology see [63, 64] and references therein. The long lifetime also offers the possibility of using it for quantum information processing. For iontrap QC application the gatespeed is the main criterion. It is proportional to the squareroot of the recoil energy times trap frequency, i.e. inversely proportional to the transition frequency over mass (see

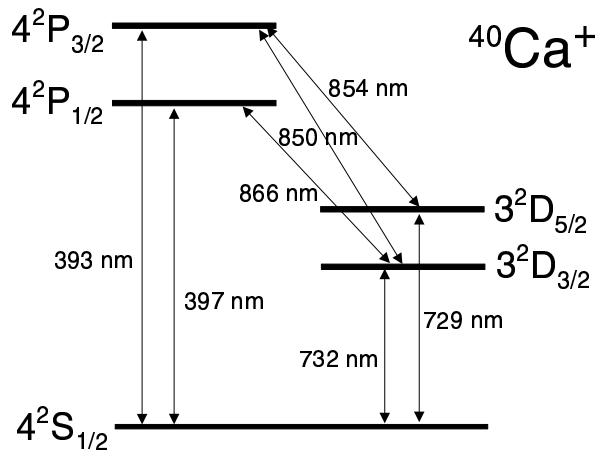


Figure 3.5: The five lowest energy levels of $^{40}\text{Calcium}^+$

reference [65] or [114] for more detail).

Calcium is also of major interest in astrophysics because of its abundance in stellar coronae and interstellar gases. Absorption lines in the near infrared and near ultraviolet from singly ionized Calcium (Ca II) are among the most prominent that are accessible from the earth. Relevant are all strong transitions in the 5-level scheme (S-P and P-D transitions, see level scheme) at 393 and 397 in the UV (H and K lines) and the so-called Near Infrared Triple (NIT) at 850, 854 and 866nm. From the absorption strengths (or ratios of linestrengths) and linewidths information about kinematics and distribution of stellar and interstellar gases can be extracted. Most directly related to the experiment described here is the 854nm line which corresponds to the observation of the Ca II $D_{5/2}$ level. Since the lifetime of this level is sensitive to collisions it is an independent indicator for temperature and density in stellar clouds. The H and K lineprofiles were used in the survey of 44 galactic stars and revealed the detailed structure of several individual interstellar cloud components [66]. The UV and 854 lines were also used, for example, in the investigation of the spatial structure of the disk of dust around Beta Pictoris [67, 68], a near-by star with cold disk-shaped dust distributed around it. Its study is highly interesting because of the possibility of observing an analogue to the solar system in its early stage, in the hope of finding clues about the mechanism of planet formation (special asymmetries in the disk). Another example of the application of calcium spectroscopy in astrophysics is the study of T Tauris stars, young protostars, which could give insight into the development of stars.

For a reliable and also quantitative analysis precise spectroscopic data about transition strengths and wavelengths are required. These data were provided by theoretical or semi-empirical calculations and experimental measurements which, however, in the past had discrepancies of up to 30%. That is why lifetime measurements of the metastable levels in calcium is of such interest for the astronomers.

3.4 Laser Sources

To drive the relevant transitions in fig. 3.5 the following laser sources are needed:

Cooling Laser at 397 nm [118]

The UV light used for Doppler-cooling and state detection on the $S_{1/2} \leftrightarrow P_{1/2}$ dipole transition is generated by frequency doubling a 794 nm Ti:Sapphire (Ti:Sa) laser². The Ti:Sa is locked using Pound–Drever–Hall method (PDH) [71] to a temperature stabilised reference cavity, resulting in a linewidth of about 200 kHz. Frequency doubling is achieved in a commercial LBO doubler³ crystal. Pumped with ≈ 1.5 W from the Ti:Sapphire it yields ≈ 200 mW UV light power at 397 nm. A power of 3 mW at the fibre output on the experiment table is sufficient for laser cooling of the trapped ion.

²CR-899-21, Coherent, Ar⁺ pumped, later replaced by a Coherent Verdi (V10).

³Spectra Physics LAS, ‘Wavetrain’

3 Experimental Set-Up

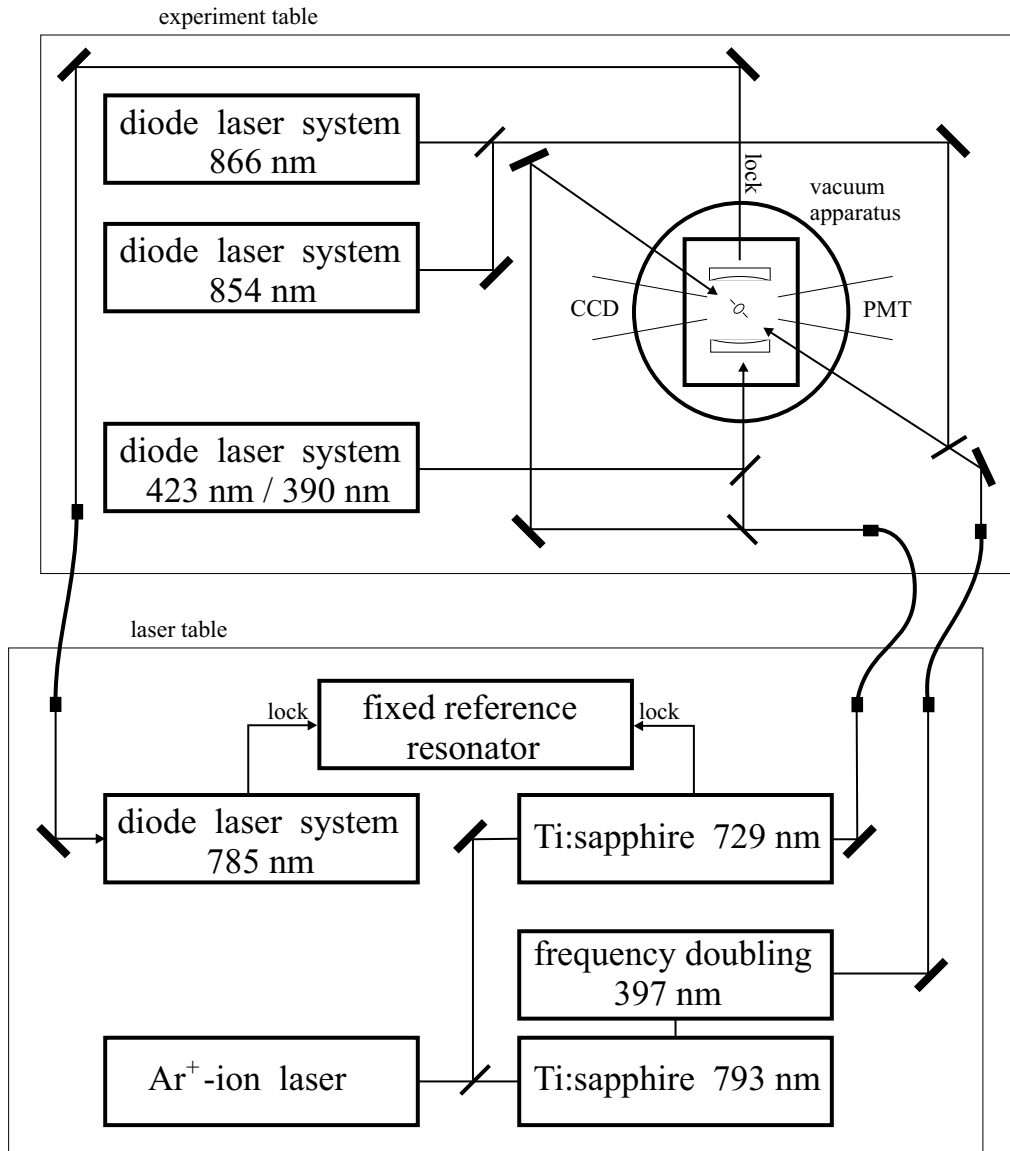


Figure 3.6: Overview of the experimental setup. The experiment extends over two optical tables. The laser sources for 397 nm, 729 nm, and 785 nm light are located on the laser table. The light is transmitted to the experiment table by optical fibres, where the diode laser systems at 866 nm, 854 nm and the ionisation lasers at 423 nm and 390 nm are situated. The vacuum apparatus and the detection units are also located on the experiment table. The Ar⁺-ion laser has now been replaced by two Coherent Verdi lasers for pumping the Ti:Sapphire lasers.

Ultrastable laser at 729 nm [117]

For excitations on the narrow quadrupole transition $S_{1/2} \leftrightarrow D_{5/2}$, a very narrow band Ti:Sapphire laser⁴ at 729 nm is used. Stabilisation is achieved by PDH-locking to an evacuated and temperature stabilised (sub μK , [117]) high finesse cavity ($\mathcal{F} \approx 220000$) and results in a linewidth of about 100 Hz. Typical light power at the experiment table is 25 mW.

Diode lasers at 866 nm and 854 nm [69, 70]

The diode lasers at 866 nm and 854 nm are used to repump occupation of the $D_{3/2}$ and the $D_{5/2}$ levels. The frequencies of the lasers are grating stabilised using the Littrow configuration. They are locked using the Pound–Drever–Hall method [71] to temperature stabilised cavities having a finesse of about $\mathcal{F} \approx 1000$, resulting in laser linewidths of ≈ 10 kHz. About 1 mW of light power is sufficient at the trap apparatus. The wavelengths are measured by comparison with a He-Ne-laser (wavemeter) [72] and checked optionally on a hollow cathode Ca discharge lamp (866 nm) or on the ion (854 nm).

Diode laser at 785 nm [113]

With the help of the diode laser at 785 nm a transfer lock from the 729 nm cavity to the trap cavity is realised. For this the 785 nm laser is locked to the 729 nm cavity and the trap cavity in turn is locked to the 785 nm light. A double pass AOM configuration allows for fine tuning of the trap cavity length. The procedure is described in section 3.6.

Photoionisation lasers at 423 nm and 390 nm [74, 114]

The two step photoionisation light source is composed of laser diodes at 423 nm and 390 nm. The laser at 423 nm excites atomic Ca to the $4p \ ^1P_1$ state. From this level the laser at 390 nm excites further to Rydberg states near the continuum. The Rydberg ion is then field-ionised by the trapping fields. Both laser diodes are grating stabilised by the Littrow technique. Fine tuning of the more critical 423 nm laser frequency is done with the help of a hollow-cathode Ca discharge lamp. The wavelength at 391 nm is relatively uncritical (loading could be achieved between 390.5 nm and 391.4 nm) Both laser beams are superimposed on a polarising beam splitter and focused through the ring of the trap. A power of 1.3 mW at 423 nm and 0.6 mW at 390 nm is sufficient to load a few ions into the trap in about one minute at an oven current of 2.1 A.

All wavelengths are measured with a custom-built wavemeter with a relative precision of 10^{-7} [72]. The wavemeter works by comparing the unknown wavelength with a reference wavelength of a He-Ne laser.

⁴CR-899-21, Coherent

3.5 Geometry

The relative coupling strengths of the Zeeman sublevels depend strongly on the geometry of beam direction and polarisation with respect to the quantisation axis (fig.3.7a). The aim is to maximise the qubit coupling strength (change of magnetic quantum number $\Delta m = 2$) and eliminate the other transitions to the largest possible extent. This should hold for the direction of the cavity axis and the 729 nm beam. The magnetic field is approximately perpendicular to both the cavity mode and the 729 nm beam. This is confirmed for the cavity mode in fig. 3.7b: The measured ion cavity-coupling is shown as a function of the 729 nm polarisation. The polarisation of the 729 nm beam is set at right angles to the magnetic field. In addition, the cooling laser and repumper beams should have a projection onto all trap oscillator axes for optimal Doppler cooling. The sigma optical pumping beam should be pointing in the direction of the magnetic field, for obvious reasons. How these constraints are met in the experimental set-up is shown in figure 3.8.

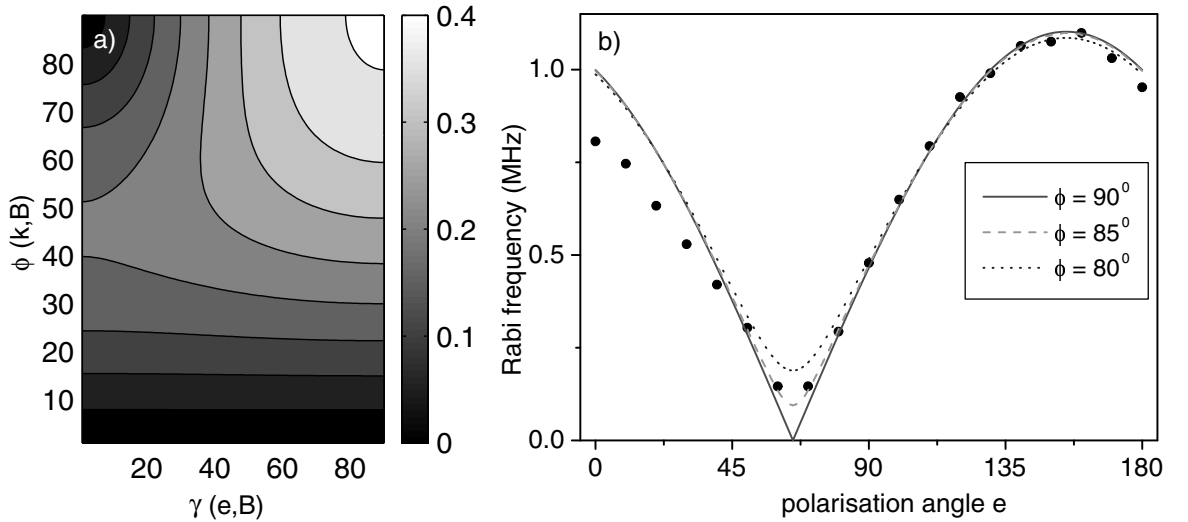


Figure 3.7: **a)** Geometrical coupling strength on the $S_{1/2} \leftrightarrow D_{5/2}$ quadrupole transition for $|\Delta m| = 2$. ϕ denotes the angle between laser beam \mathbf{k} and magnetic field \mathbf{B} . γ is the angle between polarisation \mathbf{e} and the projection of \mathbf{B} onto the plane normal to \mathbf{k} . Dark shadings correspond to low coupling. **b)** Measured coupling strength (Rabi frequency) of the ion excited by the 729 nm laser injected into the cavity as a function of polarisation angle e . Solid circles are experimental data. Included are calculations for different angles ϕ which suggest that ϕ is close to 85° . The polarisation is near-perpendicular to the magnetic field at $e = 155^\circ$ (maximum coupling).

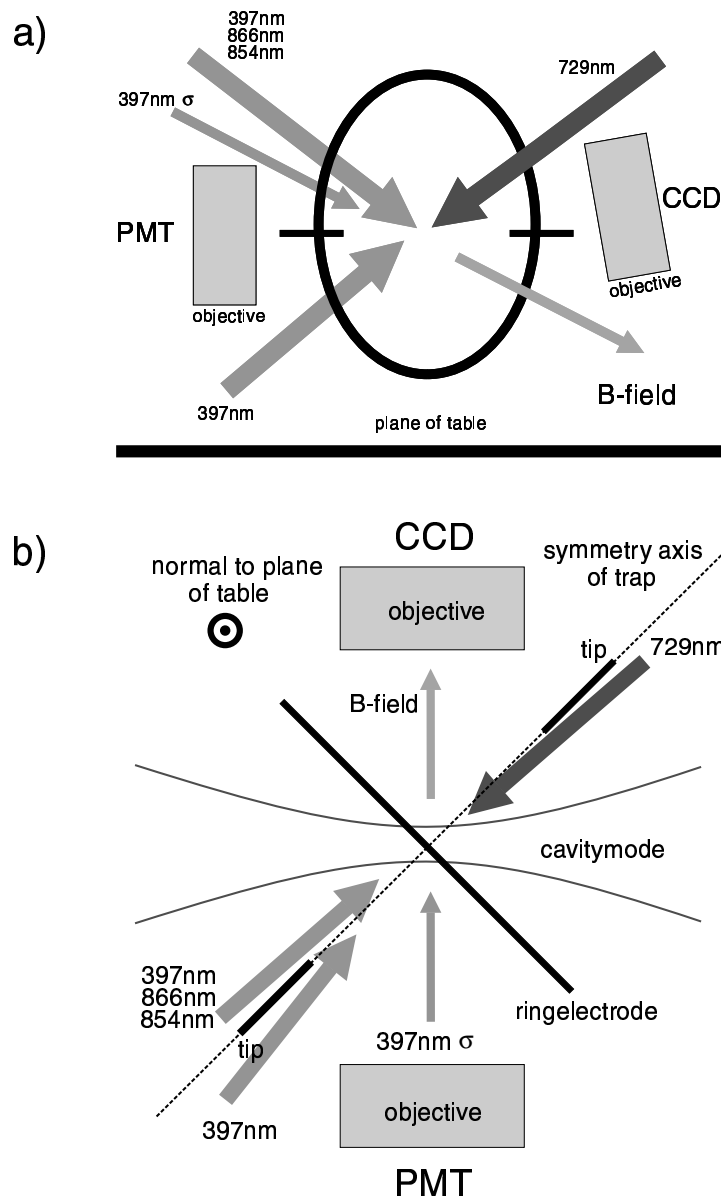


Figure 3.8: Geometry of trap axes, cavity mode, beams and magnetic field. View along the cavity axis (a) and top view (b). The trap axis is at 45° to the cavity mode. The magnetic field is approximately perpendicular to both the cavity mode and the 729 nm beam for maximum coupling to the $D_{5/2}$ $m=-5/2$ Zeeman level, the qubit transition. The cooling and repumper beams have projections onto all three trap axes. The cavity waist as well as ring and endcaps of the trap are sketched schematically.[113]

3.6 The Transfer Lock

For any deterministic ion-cavity interaction the cavity must be stabilised to the corresponding atomic transition. At the same time the lock should leave the ion unperturbed. This defines the problem that is resolved by the concept of the so-called transfer lock. It allows stabilisation of a cavity to one wavelength (the atomic) by using another (transfer) wavelength for which the cavity is also resonant, a situation called *double resonance*. In this experiment it translates to using far-detuned light at 785 nm to stabilise the cavity to the qubit transition at 729 nm.

The 785 nm diode laser is locked to the same ultra-stable reference cavity as the 729 nm laser which ensures a fixed frequency relation between the two lasers (and hence the lengths of the cavities are fixed relative to each other). For the laser set-up see section 3.4. The cavity must then fulfill a double resonance condition for both wavelengths of which one (the 729 nm) wavelength is dictated by the ion's resonance conditions. The procedure then is to scan the cavity over the 729 nm resonance where the transmission is monitored with a photodiode (and CCD camera) while finding a corresponding mode of the 785 nm laser that matches the cavity resonance. This mode can be found as follows: by tuning the current a suitable longitudinal mode of the diode laser is selected. The piezovoltage allows one to match a mode of the reference cavity which has a free spectral range (FSR) of 750 MHz. (The trap cavity has a FSR of 7.14 GHz) If that mode is close enough to the trap cavity mode by ± 100 MHz it can be fine-tuned by an AOM (in double pass configuration). The situation can be more readily visualised by considering two frequency combs with different spacing which are to be overlapped

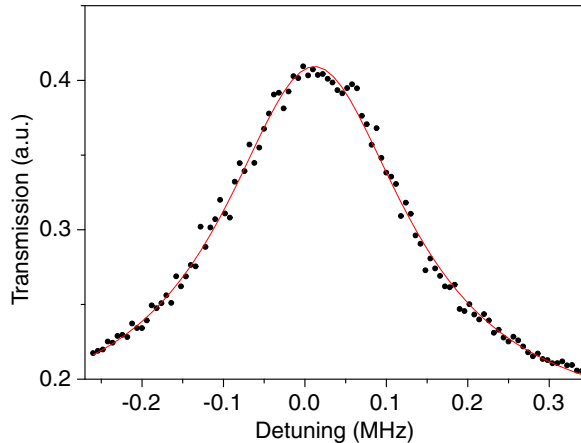


Figure 3.9: Transmission of 729 nm light through the locked cavity while the frequency of the transfer laser is scanned. The linewidth at 785 nm is ≈ 300 kHz corresponding to an *effective* finesse of $F = 22000$ at 729 nm. Note that the detunings at 729 nm and 785 nm are related by $\delta\nu_{729} = \delta\nu_{785} \cdot \frac{729}{785}$.

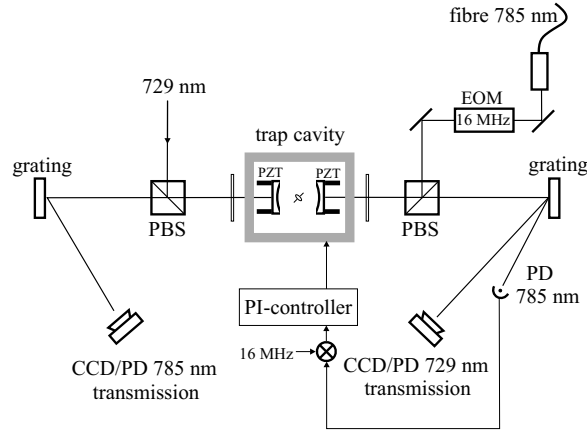


Figure 3.10: Setup of the trap cavity lock. The light at 785 and 729 nm is coupled into the cavity from opposite directions in a symmetric way. Gratings (1200/mm) on both sides separate the beams and ensure control of the transmitted power at both wavelengths without perturbation by reflections of the other light. The 785 nm light is phase modulated and with the standard techniques a Pound-Drever-Hall error signal is obtained to lock the trap cavity to the 785 nm light. Lenses are omitted for the sake of clarity. The figure is adopted from [113].

at a given point. The offset of one is fixed and the other can be moved in frequency space: discretely by jumps of 750 MHz (the FSR of the reference cavity) and several GHz (FSR of the laser diode) and continuously by 200 MHz. Using these parameters double resonance could always be found with a little experimental practice.

To characterise the cavity lock, the frequency of the transfer laser was scanned while the cavity stayed locked which is shown in fig. 3.9. The cavity transmission was detected by a photo-diode. The transmission is fitted by a Lorentz function which yields a linewidth⁵ of $\delta\nu_{785} = 302$ kHz. This translates to a finesse of $F = \delta\nu/\nu_{FSR} = 22000$ at the transition wavelength of 729 nm. The result is somewhat smaller than the finesse found independently from a direct decay measurement of the intensity. By recording, on a photodiode, the exponential decay of the output light field after the input light had been switched off $F = 35000$ was found [113]. This is interpreted as an inhomogeneous broadening of the natural cavity linewidth by acoustical and electrical noise that limits the cavity lock and produces a lower *effective* finesse.

⁵Both laser linewidths (729 nm and 785 nm) are below 2 kHz and can be neglected here.

3 *Experimental Set-Up*

4 Characterisation of a Single Ion

The experimental prerequisites that are needed for the lifetime measurements are presented here. The properties that characterise a single ion are its electronic and vibrational state. The coherent dynamics of carrier and sideband transitions are then used to, for example, gain knowledge about the ion's wavepacket extension.

4.1 Loading and Detection

All measurements within this work are done on a single ion. In the following the procedure of preparing the set-up will be outlined. The procedure is mostly identical to the one described in ref. [113]. The process starts with switching on all laser sources (see previous chapter) and electrical supplies (including trap power) and allow time (> 2 hours) for warm-up. Then, adjustments on the lasers for optimising power and the correct wavelength are done.

The principle of loading ions into an ion trap is as follows: a beam of thermal calcium atoms is produced from an oven and directed through the trap volume. The oven consists of a steel tube filled with elementary calcium and heated with a current of a few ampères. The ionisation laser beams are overlapped and directed through the trap to ionise the atoms in the trap volume.

The photoionisation used here is a two-step process. First the atom is resonantly excited to the $P_{1/2}$ level and from there to a high Rydberg state close to the continuum which is then field-ionised by the RF trap field. The photoionisation lasers replaced the old electron impact method and improved the experiment considerably. With a much higher ionisation efficiency the oven current could be decreased which implies less patch effects and basically no more compensation problems. Also, the resonant method ensures that only ^{40}Ca is loaded and no 'dark' ions. An alternative way of photoionising calcium has been demonstrated by the ion-trapping group in Åarhus [73]. They use two transitions at 272 nm to excite the atoms into the continuum.

Driving the dipole transition which couples the $S_{1/2}$ ground state to the short-lived $P_{1/2}$ state, several 10^7 photons are scattered per second¹. These photons can be detected with an objective and a PMT even with an objective that covers only a relatively small

¹this cycle is not closed and an additional repumper laser is needed to empty the $D_{3/2}$ level which is otherwise populated via the 1:16 branching ratio of the $P_{1/2}$ level

4 Characterisation of a Single Ion

solid angle and non-perfect PMT quantum efficiency². In our experiment the maximal count rate of a single ion is 25kHz with a background rate of ~ 2 kHz. In addition, the scattered light is focussed onto a CCD chip to obtain a spatial image of the ion or a cloud of ions.

Micromotion of the ion due to stray electric fields must be compensated. There are three ways of compensating which can be applied simultaneously. The three signals that are directly or indirectly related to micromotion are: PMT signal, correlation of PMT signal and trap drive phase and the CCD-camera image. The whole procedure for this type of trap has been described in great detail in ref. [118].

4.2 The Electronic State

In the theory part in chapter 2.1 a single Ca^+ ion is described as a 2-level system which forms the qubit. The real atom has, of course, a richer electronic structure and these two levels must be identified experimentally. First of all a quantisation axis is defined by applying a magnetic field of ~ 3 Gauss³ to the ion which splits the $S_{1/2}$ into two and the $D_{5/2}$ into five Zeeman sublevels, respectively. Hence the spectrum of the $S_{1/2}$ - $D_{5/2}$ transition would actually consist of ten carrier transitions each with six sidebands (SB), a blue and a red sideband⁴ for each oscillator axis. The axes are denoted x, y and z, where x and y are the radial modes (in the plane of the ring) and z the axial mode (along the tip axis). In addition micro-motion sidebands at the trap drive frequency are possible. However, identification of spectral lines is simplified due to initial preparation into the $S_{1/2}(m = -1/2)$ groundstate by optical pumping which eliminates half the spectrum. The line strength depends on the nature of the transition, i.e. carrier or sideband, the change of the magnetic quantum number Δm of the transition, i.e. the Clebsch-Gordon coefficient and finally the geometry of beams \vec{k} , polarisation \vec{e} and magnetic field \vec{B} .

Here, the 2-level system is realised by the $S_{1/2}(m = -1/2)$ and $D_{5/2}(m = -5/2)$ Zeeman levels. This transition will also be referred to as qubit transition in this work. The geometry (see section 3.5) is such that this transition is the strongest and can easily be identified in the spectrum. The magnetic field strength has been chosen such that none of the transitions coincide in frequency. To identify the qubit transition an excitation spectrum is measured by applying a sequence of laser pulses to the ion. The pulse sequence consists of three parts (fig. 4.1b).

- State preparation (Doppler cooling (397nm, 866nm, 2ms), resetting in case ion was in D-state (854nm, 2ms), optical pumping to $m=-1/2$ ground state (397nm,

²The PMT used here is an Electron Tube P25PC with quantum efficiency $\eta = 25\%$ at 397 nm

³Achieved with a current of 95 mA through the main coil

⁴Carrier transitions are transitions with no change in the phonon number ($\Delta n = 0$), sideband transitions are accompanied by an increase ($\Delta n = 1$, blue SB) or reduction ($\Delta n = -1$, red SB) of the phonon number.

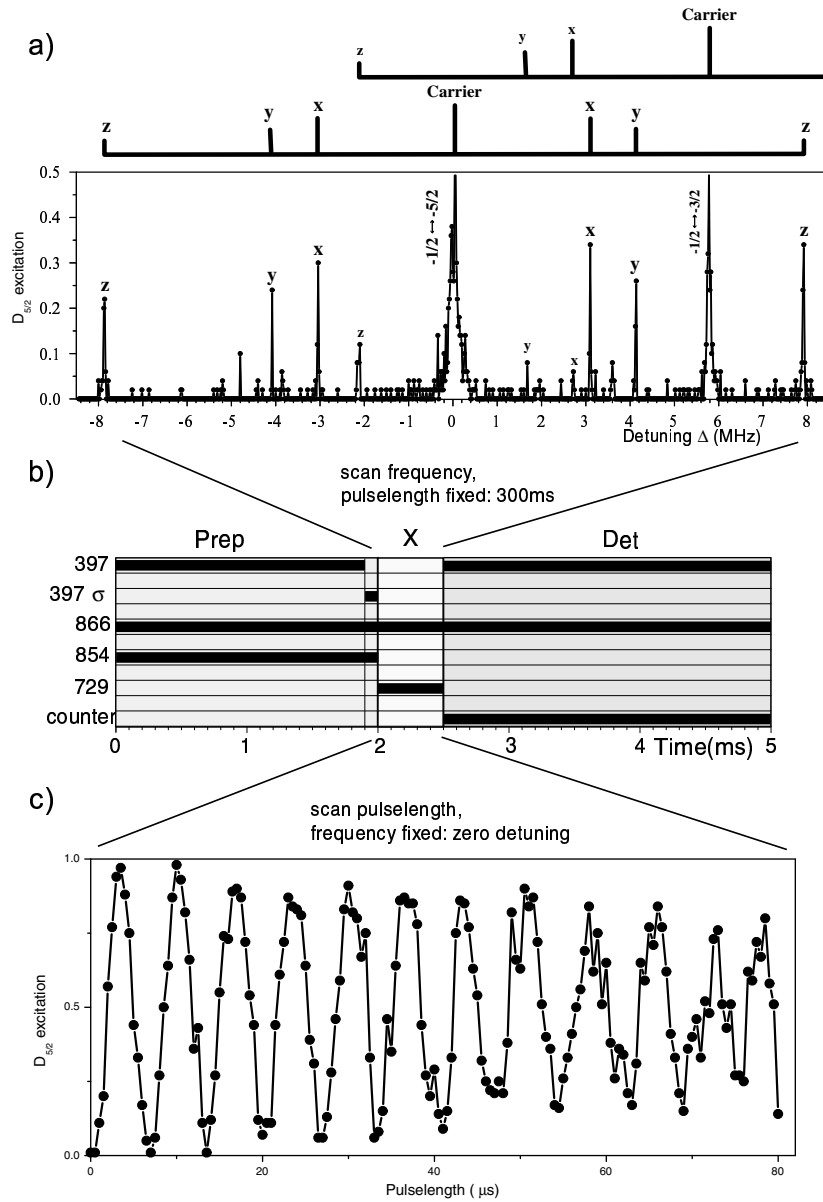


Figure 4.1: **a)** Partial spectrum of the $S_{1/2}$ - $D_{5/2}$ transition. The spectrum is centered around the qubit transition with its vibrational sidebands. The second weaker carrier is from the $m=-1/2$ to $m=-3/2$ transition. **b)** Schematic of the pulse sequence. The laser pulse at 729 nm is either scanned in frequency for the spectroscopy in a) or in pulselength for the coherent dynamics in c). More details are given in the text. **c)** Rabi oscillations on the carrier reveal coherent excitation of the two-level system.

4 Characterisation of a Single Ion

σ^- polarised, 0.1ms))

- Excitation pulse (729nm, 0-1ms)
- Detection (397nm, 866nm, 3.5ms)

This sequence is repeated 100 times to obtain the excitation probability from the detection results (one data point). A spectrum consists of many such points with the frequency of the 729 nm laser scanned in a certain frequency range. An example of a spectrum is shown in fig. 4.1a where the various transitions are indicated.

Once the frequency of the qubit transitions is determined to a precision of at least 1 kHz an arbitrary superposition of the two levels can be created by an appropriate choice of the excitation time. This coherent dynamics manifests itself in Rabi oscillations when the pulselength is scanned. An example of such Rabi oscillations on the carrier transition is depicted in fig. 4.1c.

In the next two sections the Rabi oscillation on the carrier and sideband transitions are used to gain information on the motional state of the ion.

4.3 The Motional State

4.3.1 Cooling

The ion moves in the quasiharmonical trap potential which results in the well-known harmonic energy eigenstates with equidistant energy levels with $\Delta E = \hbar\omega$. The motional states are characterised by the vibrational quantum number $n = 1, 2, 3, \dots$ also called the phonon number, analogous to the quasiparticle of acoustical excitation in solid state physics, the phonon. For the quantised motion to be apparent the quantum number n must be small which is achieved with laser cooling.

The principle of the most common type of laser cooling in ion traps, namely Doppler cooling, is the following: Depending on the detuning of the laser light each scattering event changes the energy of the ion. For cooling, the light is red-detuned with half the linewidth of the upper level ($\Delta = 1/2\Gamma \simeq 10\text{MHz}$). Then the ion experiences a decelerating velocity dependent force since the momentum of the absorbed photon is fixed by the k-vector of the laser beam while the emission recoil occurs in any direction. Furthermore, the energy of the scattered photon is, on average, higher than the energy of the absorbed photon and the ion is cooled. Physically, this is a very intuitive but over-simplified picture and the quantitative theory is far more complicated and can be read elsewhere [75, 76]. For example, the dipole emission pattern is not isotropic and has to be taken into account to find the exact resulting force. Also, the micro-motion

has to be considered. The Doppler cooling limit⁵ is given by:

$$E_{min} = \frac{1}{2}k_B T_{min} = \frac{\hbar\Gamma\sqrt{1+s}}{8}(1+\xi) \quad (4.1)$$

using a detuning $\Delta = \frac{\Gamma}{2}\sqrt{1+s}$ (s is the saturation parameter ($2|\Omega|^2/\Gamma^2$) and ξ is a geometry factor for the emission pattern, for dipole radiation $\xi = 2/5$). In the experiment the power of the Doppler beam is reduced to well below saturation so that $s < 1$. The resulting mean vibrational quantum number is given by: $E_{min} = \hbar\omega(\bar{n}_{min} + 1/2)$. Note here that for cooling it is advantageous to have high trap frequencies (stiff traps) since it implies a lower \bar{n} .

In the experiment the ion does not end up in a pure motional state but in a thermal state which is a mixture of states $|motion\rangle = \sum p_n|n\rangle$. In a thermal state the occupation probability p_n for a n phonon state follows from the Boltzmann distribution and the mean \bar{n} :

$$p_n = \frac{1}{\bar{n} + 1} \left(\frac{\bar{n}}{\bar{n} + 1} \right)^n \quad (4.2)$$

The Rabi oscillations for an ion in a thermal state consist of many frequencies, since every state contributes with its frequency $\Omega_{n,n+1}$ with amplitude p_n . Coherent excitation of the blue sideband with pulselength t is then written as:

$$p_D(t) = \frac{1}{2} \left(1 - \sum_n p_n \cos(\Omega_{n,n+1}t) \right) \quad (4.3)$$

The Rabi frequency for carrier and sideband transitions depending on the motional state is given by⁶:

$$\Omega_{car} = \Omega_{n,n} = \Omega_0(1 - \eta^2 n) \quad (4.4)$$

$$\Omega_{red} = \Omega_{n,n-1} = \eta\sqrt{n+1} \Omega_0 \quad (4.5)$$

$$\Omega_{blue} = \Omega_{n,n+1} = \eta\sqrt{n} \Omega_0 \quad (4.6)$$

Ω_0 is the Rabi frequency defined in equation 2.11. The Lamb-Dicke (LD) parameter η is defined as

$$\eta = k \cos(\phi) \sqrt{\frac{\hbar}{2m\omega}} \quad (4.7)$$

⁵Interestingly, the same cooling limit applies for the cooling of free particles [75].

⁶Ignoring higher order terms in η^2 .

4 Characterisation of a Single Ion

(ϕ being the angle between the light's wavevector k and the oscillator axis with frequency ω , m is the ion's mass.)

The measurements of carrier and sideband frequencies have been discussed already in the thesis of A.B. Mundt [113] and will only be quoted here. Since the sideband Rabi frequency depends on the squareroot of the phonon number n as evident in equations 4.4 to 4.6, one can find \bar{n} by driving carrier and sideband transition coherently and comparing the respective Rabi frequencies. The Rabi oscillation on the sidebands are composed of different frequencies $\Omega_{n,n+1}$ contributed by each vibrational state n with amplitude p_n and will damp out quickly. So the problem is to find a consistent solution for the mean n of all three oscillators given the geometry and trap frequencies and the carrier Rabi frequency Ω_0 . The method is explained in more detail in the next section. The parameters of the vibrational state were determined to be [113]

$$[\bar{n}_x, \bar{n}_y, \bar{n}_z] = [20(5), 5(1), 5(1)] \quad (4.8)$$

with the following LD-parameters

$$[\eta_x, \eta_y, \eta_z] = [0.04, 0.02, 0.03] \quad (4.9)$$

Now, the wavepacket extension w_i can be calculated using

$$w_i = \sqrt{\frac{\hbar(\bar{n}_i + \frac{1}{2})}{m\omega_i}} \quad (4.10)$$

and result in

$$[w_x, w_y, w_z] = [42(5), 17(2), 15(1)]\text{nm} \quad (4.11)$$

These numbers justify that after Doppler cooling the ion is in the LD-regime ($\eta^2 n \ll 1$) or the wavepacket extension $w \ll \lambda_{transition} = 729$ nm. This is the pre-requisite for mapping the cavity standing wave with high contrast (c.f. section 6.1.2 and 6.3).

To cool the ion to the vibrational groundstate a further cooling stage must be implemented. One example is sideband cooling. In the LD-regime and strong confinement⁷ the motional sidebands are well resolved from the carrier transition and the sideband transition can be driven selectively. Excitation on the red sideband and subsequent decay back to the ground state results in the loss of one phonon from the vibrational mode which is the general principle of sideband cooling. To make the scheme feasible the upper level is quenched by coupling it to the P-state with the repumper laser (then called quenching laser). This increases the scattering rate and hence the cooling rate. More details on the experimental techniques can be found in ref. [118]. The sideband cooling results on the axial oscillator are shown in figure 4.3 and yields a mean phonon number after sideband cooling of $\bar{n}_z = 0.2$ corresponding to a groundstate probability (GSP) of 80%. Sideband cooling to 99% GSP has been achieved in this group by C. Roos *et al.* [79].

⁷The regime where the trap frequency is much larger than the natural linewidth of the atomic transition.

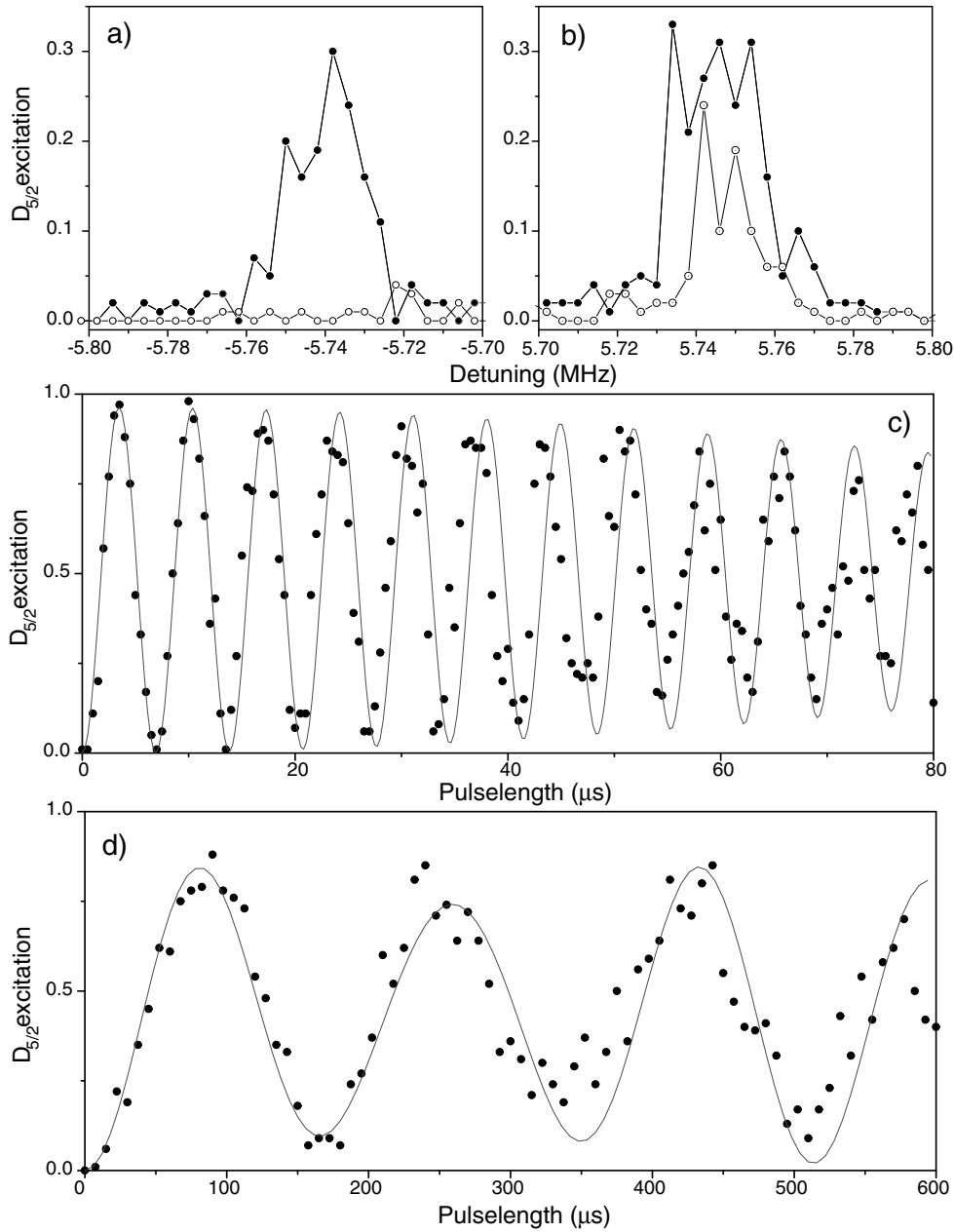


Figure 4.3: Sideband cooling results: Absorption of red **a)** and blue **b)** axial sideband before (solid circles) and after (open circles) sideband cooling. Rabi oscillations on the carrier and the blue axial sideband are shown in **c)** and **d)**, respectively. The solid lines are best-fit model calculations to the data points which yield ground state occupation probability of 0.8 for the axial oscillator.

4.3.2 Heating

The heating rate denotes the gain of vibrational energy with time. In this work the heating rate has relevance for two reasons. First, in the lifetime measurements (chapter 5) long intervals (of up to 5 seconds!) without cooling are necessary. After that time coherent excitation must not be affected. In the most severe case heating also causes a decrease in the fluorescence counts affecting the state detection. Second, for the mapping of the vacuum standing wave (chapter 6) good localisation of the ion is a prerequisite. Vibrational heating increases the wavepacket and leads to a reduced contrast of the standing wave.

Vibrational heating in ion traps has been subject to some investigations in the past (see e.g. [80] and references therein) but its origin is not completely conclusive and still under debate. A possible candidate is the electric field influence of fluctuating patch charges on the trap electrodes. Other models, for example Johnson noise in the electrodes were unable to account for the experimentally observed heating rates. However, it is evident from the results in [80] and [118] that the heating rate scales inversely with trap size, i.e. larger traps generally have smaller heating rates.

The heating rate is determined by inserting a delay time between the cooling and the coherent excitation pulse as depicted in the pulse sequence in fig. 4.4. Thus the vibrational state (\bar{n}) is measured as a function of delay time and the linear gradient $\frac{d\bar{n}}{dt}$ is the heating rate.

The mean phonon number \bar{n} is determined from the sideband and carrier Rabi oscillations (fig. 4.5). Here only the radial x-oscillator is considered. The D-state population $p_D(t)$ as a function of pulselength time in equation 4.3 is the model function for the data and the fit variable is \bar{n}_x . The corresponding amplitudes p_n (equation

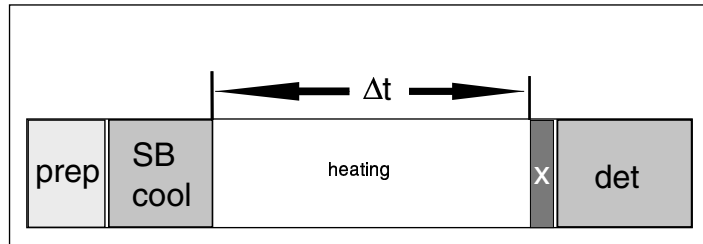


Figure 4.4: Sketched pulse scheme for the determination of heating rates. Preparation (prep), excitation (X) and detection (det) are identical to the one in section 4.2. The sideband cooling part consists of a laser pulse at 729 nm tuned to the red sideband of the carrier transition. At the same time the laser at 854 nm is switched on for quenching the transition. In addition, several short optical pumping pulses (σ polarised light at 397 nm) are included, to prevent pumping into the $m=1/2$ Zeeman groundstate.

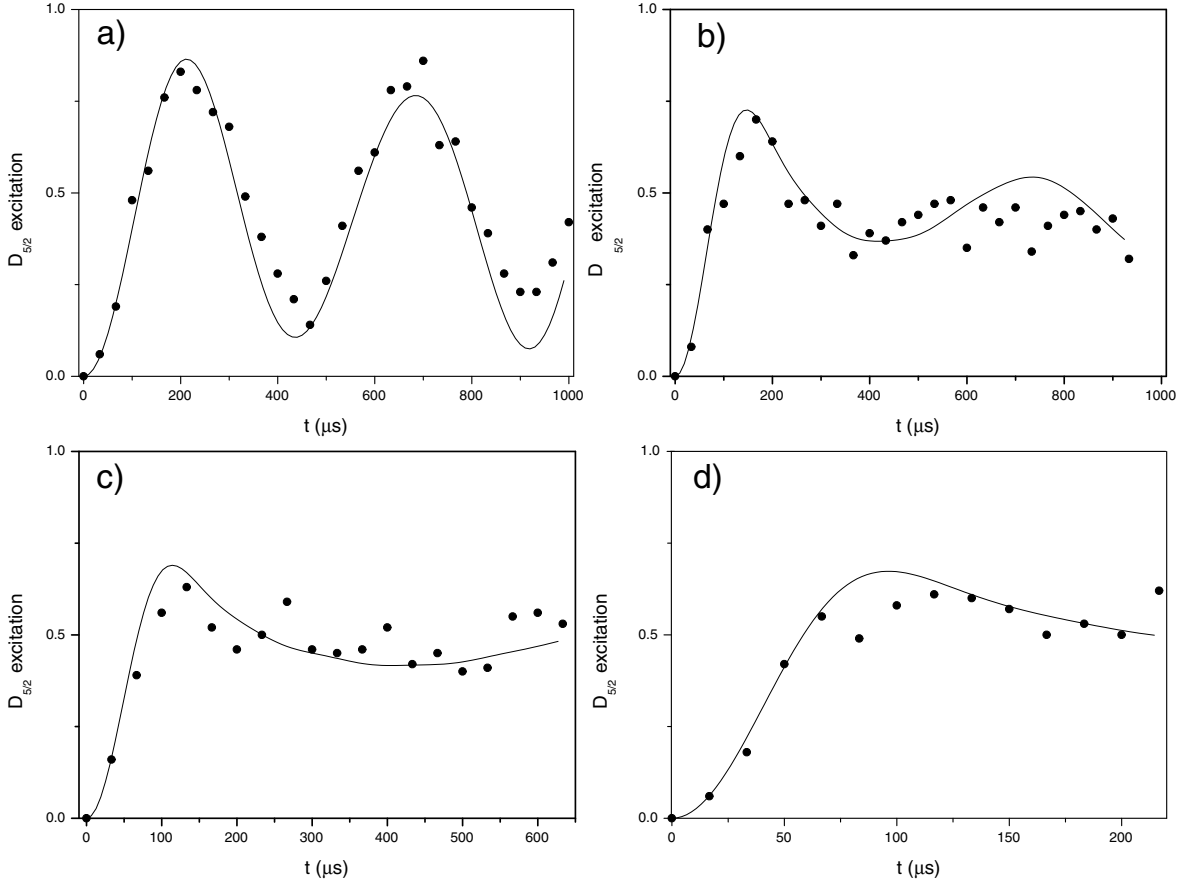


Figure 4.5: Rabi oscillations on the blue sideband of the x-axis. In a-d the waiting period has been changed (0, 20, 40 and 60 ms, respectively) to observe the heating from the groundstate. Circles are experimental points, the solid curve is the best-fit model calculation. Note the different x-scales.

4.2) for frequencies up to a cut-off are calculated and produce the model curve. The required parameters are $\eta_{x,y,z}$, and $\bar{n}_y = \bar{n}_z = 5$ known from the previous measurements in section 4.3.1. Ω_0 is determined independently from carrier Rabi oscillations. The model also includes a possible detuning Δ . Then \bar{n}_x and the detuning are varied to minimise the deviation from the experimental data.

The Rabi oscillations on the blue axial sideband are shown in fig. 4.5. For $\Delta t = (0, 20, 40, 60)$ ms the resulting vibrational quantum numbers are $\bar{n} = (0.2, 2, 4, 6)$ yielding a heating rate of 0.1 ms^{-1} . This is an unexpectedly high heating rate compared to the previous ring trap (of similar dimensions) for which that rate was measured to be 1 phonon per 190 ms or 0.005 ms^{-1} for the axial oscillator [118]. This means that 1 second after Doppler cooling the ion has heated to $\bar{n} \sim 100$ which is considerable for the carrier Rabi oscillations since $\Omega_{car} = \Omega_0(1 - \eta^2 n)$ (4.4). Then both Rabi frequency

4 Characterisation of a Single Ion

and the maximum transfer to the D-level decrease. This is, for example, a limiting factor for the lifetime measurement of the $D_{3/2}$ level. For that purpose the lifetime measurements in chapter 5 have been performed in a linear Paul trap with much lower heating rate.

If the ground state probability is close to one, \bar{n} can also be inferred from the ratio of the amplitudes of the red and blue sideband which become asymmetric. In the absolute groundstate the red sideband cannot be excited at all because no phonon can be absorbed from the empty vibrational mode. This decrease in the red sideband amplitude, compared with and without sideband cooling, is illustrated in fig. 4.3a. However, this method is less accurate.

5 Lifetime Measurements

5.1 Overview

Early experiments on the measurement of the D-level lifetimes in $^{40}\text{Ca}^+$ [81–85] used large clouds of ions and the lifetime was determined by recovery of fluorescence on the UV-transitions ($S_{1/2} - P_{1/2}$ or $S_{1/2} - P_{3/2}$, see Fig. 3.5) after electron shelving in the D-states or by observing UV fluorescence after driving transitions from the D-states to the P-states. These lifetime measurements were limited by deshelving induced by collisions with other ions or the buffer gas used for cooling. Similar results using the same techniques have been obtained in an ion storage ring [86]. More accurate results can be obtained by performing lifetime measurements with single trapped ions [87–91] or crystallised strings of few trapped ions [92] and employing the so-called quantum jump technique. This technique is based on monitoring the fluorescence on the $S_{1/2} - P_{1/2}$ dipole transition while at random times the ion is shelved to the metastable state where the fluorescence falls to the background level. Shelving is initiated by applying laser light at 850 nm ($D_{3/2} - P_{3/2}$) [87] or at 729 nm ($S_{1/2} - D_{5/2}$) [91]. The idea of observing quantum jumps of a single ion was brought forward by Dehmelt [93] and was first observed experimentally almost simultaneously by three groups [94–96].

Statistical analysis of the dark times yields the lifetime τ . The most precise measurement using this technique was carried out by Barton et al. [90] who found the result of $\tau=1168(7)$ ms. Analogous lifetime measurements exist for other higher-Z alkaline earth elements such as Strontium [97] and Barium [94] which have a very similar atomic structure as calcium.

In this work the main goal is to measure the lifetime reduction due to the coupling to the vacuum field inside a cavity. Here the quantum jump technique fails because it requires the continuous illumination of the ion by dipole coupling laser light which results in power-broadening of the $S_{1/2}$ ground state and hence the quadrupole transition. Even for low laser power this transition is broadened beyond the cavity linewidth and the cavity effect diminishes¹. To avoid that we must use a different technique that interacts as little as possible with the ion during the 'measurement'. The new measurement technique that is introduced here is based on deterministic coherent excitation

¹For the free-space lifetime the linewidth plays no role since the vacuum field density can be taken as constant over the linewidth

5 Lifetime Measurements

to the $D_{5/2}$ state or incoherent shelving in the $D_{3/2}$ state, followed by a waiting period with free spontaneous decay and finally a measurement of the remaining excitation by high-efficiency quantum state detection. During the waiting time all lasers are shut off and no light interacts with the ion which could affect the free decay of the atom. This method basically is an improved version of a technique that was used earlier to measure the $D_{3/2}$ metastable level lifetime in single Ba^+ ions [98].

Another advantage of this "state detection" method is that it allows for the measurement of the $D_{3/2}$ level lifetime which otherwise is inaccessible with the quantum jump technique. There exist only a few reported $D_{3/2}$ -level lifetime results for Calcium [83, 84, 86] but none from a single ion experiment. Since single ion measurements can be made more accurate as systematic errors, e.g. due to collisions, can be reduced to the highest possible extent. Therefore, single ion D-level lifetime measurement for Calcium are of special interest.

The lifetime measurements described in this chapter are performed in a linear Paul trap instead of the ring trap set-up described in chapter 3. Nevertheless, the experimental environment for the single ion is identical except for two advantages of the linear trap which motivated this decision: First, the vacuum with a pressure of $< 10^{-11}$ mbar is about an order of magnitude better than in the CQED set up. This allows not only longer trapping times², and hence measurement times, but also to neglect systematic errors due to collisions. Second, the low heating rates of $\sim 0.01\text{ms}^{-1}$ are a huge improvement for the $D_{3/2}$ lifetime measurement. The linear trap is situated on the same experimental table, shares the same laser sources and computer control and is designed for QC related experiments with Ca^+ ions [12, 13, 15]. It has been well characterised in the Ph.D. thesis of S. Gulde in Ref. [114]. The lifetime measurements in the ring trap in the cavity are performed to demonstrate the cavity effect and not to present an accurate value *per se* for the lifetime. Also, the results from the ring trap do not reach the precision that collisional effects have to be considered. Within the statistical error bar, the lifetime results from both traps are in agreement.

5.2 The $D_{5/2}$ Level

5.2.1 Method

The lifetime measurement consists of a repetition of a laser pulse sequence applied to the ion. The detailed pulse sequence is shown in fig. 5.1. Essentially, the sequence consists of three steps:

1. State preparation and Doppler cooling, consisting of 2 ms of Doppler cooling (397 nm and 866 nm light), repumping from the $D_{5/2}$ level (854 nm light) and optical pumping into the $S_{1/2}(m=-1/2)$ Zeeman sublevel (397 nm σ^+ polarised light).

²In the linear trap the ion stays trapped for hours without cooling, as opposed to minutes in the ring trap

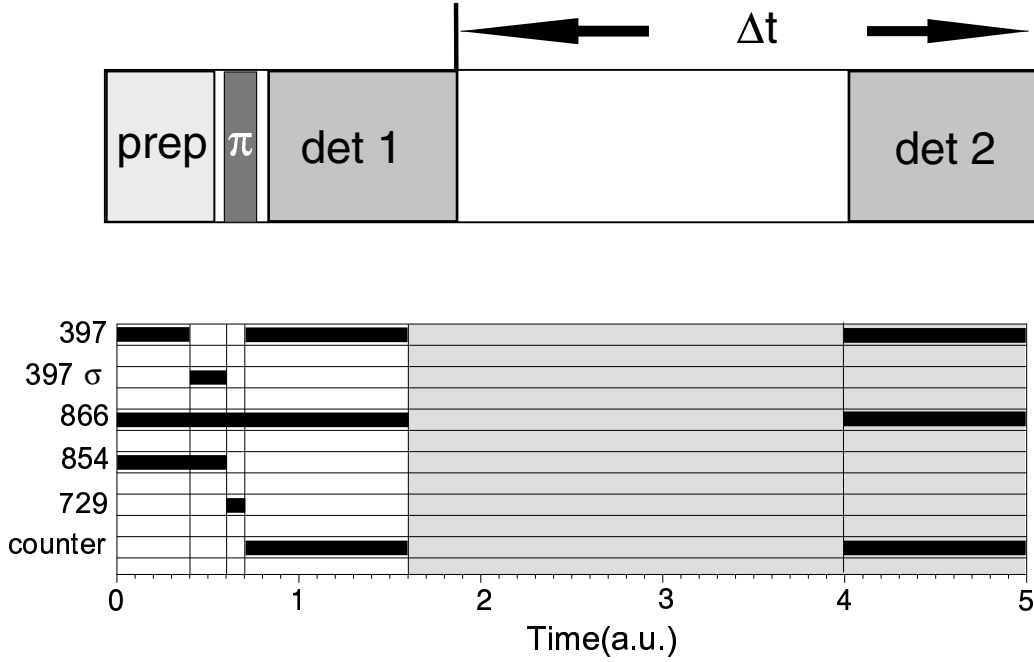


Figure 5.1: Pulse scheme for the $D_{5/2}$ lifetime measurement. The simplified sketch illustrates the essential steps: state-preparation, coherent population and two state detections separated by a waiting time Δt . This sequence is repeated typically a few thousand times to determine the mean decay probability p as a function of Δt .

2. Coherent excitation at 729 nm with pulse length and intensity chosen to obtain near unity excitation (π -pulse) to the $D_{5/2}(m = -5/2)$ Zeeman level.

3. State detection for 3.5 ms by recording the fluorescence on the $S_{1/2} - P_{1/2}$ transition with a photomultiplier. Discrimination between S and D state is achieved by comparing the fluorescence count rate with a threshold value. The state is measured before and after a fixed waiting period Δt to determine whether a decay of the excited state has happened.

This sequence is repeated typically a few thousand times to determine the mean decay probability p . In detail, p is determined as follows: each detection period yields two possible results, excitation (1) or no excitation (0), giving four possible combinations, denoted by (00),(10),(01) and (11). The first number of the pair denotes the result of the first detection, the second correspondingly. For a number of N sequences the decay probability p is then given by

$$p = \sum_N (10) / \sum_N [(10) + (11)] \quad (5.1)$$

5 Lifetime Measurements

which is the ratio of the number of decays to the number of excitations after the π pulse. The arithmetic mean of the denominator is the transfer efficiency of the π pulse which is close to unity but fluctuates due to quantum projection noise. The intensity of the 729 nm light is stabilised to 1%. On a longer time scale ($> 1\text{h}$) the transfer efficiency may decrease due to laser frequency drifts (thermal drift of the reference cavity) and intensity changes of the 729nm light (The polarization maintaining optical fiber has an optical axis that is sensitive to temperature and fiber curvature such that after a beamsplitter polarisation changes are converted into intensity changes).

5.2.2 Results and Discussion

The remaining $D_{5/2}$ population $(1-p)$ measured for several delay times ($\Delta t = 25-5000$ ms) is plotted in fig. 5.2. The delay time is defined as the time between the end of each detection period. A weighted least-squares fit to the data yields the result $\tau = 1168(9)\text{ms}$ applying the fit function $(1-p) = e^{-\Delta t/\tau}$ where p is the decay probability Δt is the delay time and τ is the only fit parameter. The resulting reduced Chi-squared parameter of $\chi^2_{\nu} = 0.47$ indicates that the experimental decay is consistent with the expected exponential decay behavior. The appropriateness of the least-squares method is justified in appendix B where also the definition and meaning of the χ^2 parameter is found. The statistical error (in brackets) is the 1σ standard deviation, a connotation used throughout this work. It should be kept in mind that the 1σ deviation is only a 68% confidence interval! A more stringent number for the error is the 2σ deviation which corresponds to a 95% confidence interval. However, it has been established in this field of science in the past decades to quote only the 1σ interval.

There are several types of systematic errors that may occur. In UHV single ion experiments the biggest source is radiation, in this case residual light at 854nm. During the delay interval it may de-excite the $D_{5/2}$ to the groundstate via the $P_{3/2}$ level (strong transition!). This additional 'decay channel' artificially shortens the observed lifetime. The obvious source for residual 854nm radiation is the 854 diode laser itself. It is eliminated by a fast mechanical shutter³ which is closed during the delay. The 40dB attenuation of the double-pass AOM which usually switches the 854 nm light was shown to be insufficient: In an earlier experiment without that shutter the lifetime was determined to be 1011(6)ms [107]. However, the result without shutter may vary ($\pm 50\mu\text{s}$) depending on the specific AOM and diode laser adjustments. Another source is background fluorescence at 854 nm from the 866 nm diode laser. To eliminate this radiation an AOM in single pass was installed in the beam path that attenuates better than 20dB, a sufficient measure since, without the AOM the systematic effect was of the order of a few percent. Note that this source of error cannot, in principle, be directly

³The best suitable shutters were found to be the Densitron, TK-CMD series. The shutters consist of a small iris with \varnothing of 1 or 3.3 mm in front of a blade driven by a solenoid plunger. Using suitable electronics for the drive closing and opening times of the order of 0.5 ms can be achieved. The jitter is on the same time scale

eliminated in the quantum-jump technique where 866 nm repumper light MUST be on continuously. This might have been a major source of systematic error in earlier measurements based on the quantum-jump method. The problem was first recognized by Block *et al.* [89]. The only way to correct for this systematic error is to measure at

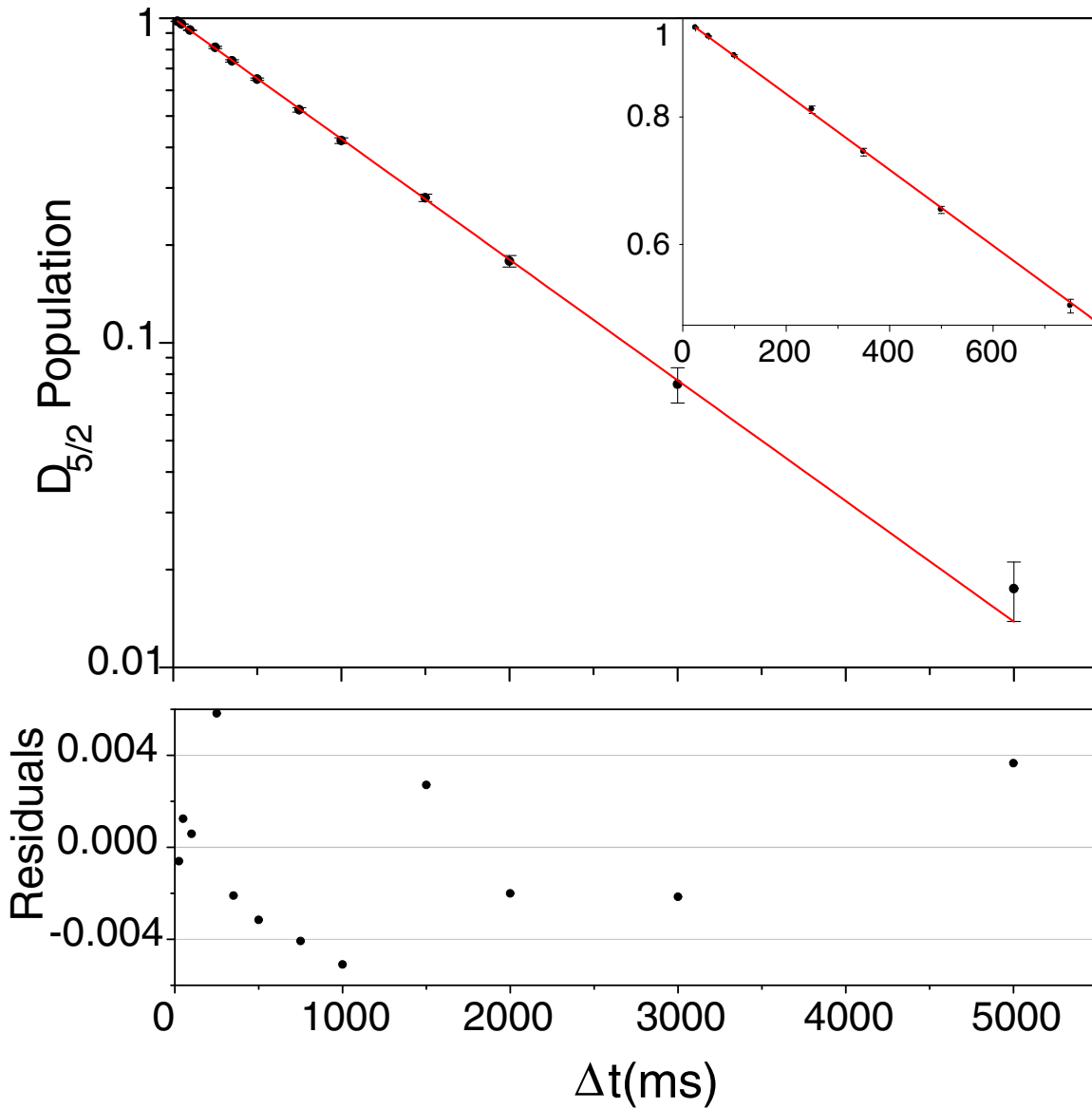


Figure 5.2: $D_{5/2}$ excitation for delay times from 50 ms to 5 s on a logarithmic scale. The solid line is a least-squares-fit to the data using the exponential fit function $(1 - p) = e^{(-\Delta t/\tau)}$. The bottom plot shows the residuals, the difference between data points and fit. No significant systematics is visible.

5 Lifetime Measurements

different repumping light powers and extrapolate linearly to zero power which in turn implies a larger statistical error (see also ref. [90]).

Also non-radiative lifetime shortening mechanisms exist, namely, inelastic collisions with neutral atoms or molecules from the background gas. Two relevant types of collisions can be distinguished: Quenching and j-mixing collisions.

Quenching collisions cause direct de-shelving of the ion into the groundstate. In the presence of high quenching rates lifetime measurements had to be done at different pressures and extrapolation to zero pressure would yield the natural lifetime. Measurement of collisional deshelling rates for different atomic and molecular species have been performed, for example, by Knoop *et al.* [84, 99]. They find specific quenching rates for Ca^+ of $\Gamma = 37 \cdot 10^{-12} \text{cm}^3 \text{s}^{-1}$ for H_2 , and $\Gamma = 170 \cdot 10^{-12} \text{cm}^3 \text{s}^{-1}$ for N_2 .

Collisions may also induce change of the atomic polarisation, a process called j-mixing or finestructure mixing. This means that a transition from the $\text{D}_{5/2}$ to the $\text{D}_{3/2}$ state or vice versa is induced (the finestructure quantum number j of the D-levels are interchanged). The rates have been measured [99] to be $\Gamma = 3 \cdot 10^{-12} \text{cm}^3 \text{s}^{-1}$ for H_2 and $\Gamma = 13 \cdot 10^{-12} \text{cm}^3 \text{s}^{-1}$ for N_2 . These collisional effects cannot be distinguished from a natural decay process. Collisional effects are most prominent in experiments with large clouds of ions or at higher background pressure. The measured lifetime is modified by additional deshelling rates γ_i as $\frac{1}{\tau_{meas}} = \frac{1}{\tau_{nat}} + \sum \gamma_i$ where $\gamma_i = n_i \Gamma_i$ (n_i being the particle density in cm^{-3}). To give an upper limit of the effect in this experiment estimates of the constituents of the background gas must be made. If a background gas composition of 50% N_2 and 50% H_2 is assumed⁴ and the pressure $p < 2 \cdot 10^{-11} \text{mbar}$ in the linear trap set up is taken an upper limit for the additional collision induced rate of $\gamma = 3 \cdot 10^{-4} \text{s}^{-1}$ is found. This effect is well below 10^{-3} relative error and can be safely neglected here. However, the pressure in the CQED setup is an order of magnitude higher ($p \simeq 2 \cdot 10^{-10} \text{mbar}$) and collisions have to be taken into account if the lifetime is measured with a precision of much better than a percent. This is not the case for the measurement of the lifetime reduction in the cavity vacuum field in chapter 6.3.

Transitions between the D-levels can in principle also be induced by a M1-transition stimulated by thermal radiation. The corresponding transition rate is given by $W_{12} = B_{12} \rho(\nu)$ with the Einstein coefficient for stimulated emission B_{12} and the energy density per unit frequency interval for thermal radiation $\rho(\nu)$. With the rate of spontaneous emission $A_{12} = (8\pi h \nu^3 / c^3) B_{12}$, W_{12} is rewritten as:

$$W_{12} = \frac{A_{12}}{e^{h\nu/kT} - 1} \quad (5.2)$$

With $\nu = 1.82 \text{ THz}$ and $A_{12} = 2.45 \times 10^{-6}$ taken from [101] we get $W_{12} = 7.23 \times 10^{-6}$ at room temperature which reduces the $\text{D}_{5/2}$ -level lifetime by much less than the statistical error.

⁴This seems a reasonable assumption according to the mass spectrometer analysis in the Åarhus ion trap experiment [92].

Finally, lifetime-prolonging systematic effects are considered. They could stem from radiation at 393nm (roomlight) or 729nm (Ti:Sa laser, double-pass AOM attenuation of ~ 40 dB) which both could achieve re-shelving. This effect, however, leads also to a different decay function. When modeled by a simple rate equation including the additional rate R with the opposite sign (see appendix C.2) the solution is of the form

$$p_D = \frac{R}{\Gamma'} + \left(1 - \frac{R}{\Gamma'}\right) \cdot e^{-\Gamma' \Delta t}. \quad (5.3)$$

where the new decay rate $\Gamma' = \Gamma + R$ (the natural decay rate is of course $\Gamma = 1/\tau$). The resulting decay curve is illustrated in figure C.3a. The initial decay is unchanged but for longer waiting times the decay approaches an offset. It is interesting to note that the additional rate requires a different exponential model whereas all shortening systematic errors due to radiation only affect the decay constant. The result from fitting the data with the modified exponential fit function from above is $\tau = 1165(10)$ ms and $R = 3(2) \cdot 10^{-3}\text{s}^{-1}$. It is shown in appendix B using simulated data that the statistical variation is $\Delta R = 3 \cdot 10^{-3}\text{s}^{-1}$. So the fitted rate is consistent with zero and not sufficiently significant to allow any conclusion about the actual rate or the model, i.e. the statistical error is too large for a data fit to resolve the small systematic error. So we obtain an upper limit for the systematic error due to a possible re-pumping rate by simulating data sets including such a rate and fitting these with a normal fit function $(1-p) = e^{-\Delta t/\tau}$. The deviation of the fit result for τ and the τ used for the simulation gives exactly the systematic error, c.f. figure C.3 in the appendix. For $R = 3 \cdot 10^{-3}\text{s}^{-1}$ the systematic error is $\Delta\tau = -3 \text{ ms}^5$.

Another systematic effect that implies a different fit model is the state detection error. Even though the efficiency is close to unity Poissonian noise in the counts and the possibility of a decay during the detection period produce a small error. In appendix C.1 these two types of error are evaluated to 10^{-5} and 10^{-3} , respectively. This error implies a model function of the form $(1-p) = (1-\varepsilon_2)e^{-\Gamma\Delta t}$. Here, only the initial decay is affected. The statistically consistent limit for this detection error is $\varepsilon_2 = 1 \cdot 10^{-3}$. Again, it cannot be resolved by a fit to the data. From the simulations an upper limit of $\Delta\tau = 7 \text{ ms}$ can be stated.

In summary, the result for the lifetime of the $D_{5/2}$ level is quoted as:

$$\tau_{(5/2)} = 1168(9)\text{ms (statistical)} - 3\text{ms (repumping rate)} + 7\text{ms (detection)}$$

⁵Meaning that the fit result is systematically 3 ms larger than expected

5.3 The $D_{3/2}$ Level

5.3.1 Method

The general strategy for the lifetime measurement of the $D_{3/2}$ and the $D_{5/2}$ level is the same (excite-wait-detect decay) however some alterations in the pulse sequence are required, see fig.5.3. To populate the $D_{3/2}$ state we use indirect shelving by driving the S-D transition at 397nm and taking advantage of the 1:16 branching ratio into the $D_{3/2}$ level. After a few microseconds the $D_{3/2}$ level is populated with unity probability. Alternatively, the quadrupole transition could be driven directly in analogy to the $D_{5/2}$ π -pulse by tuning the Ti:Sa laser from 729nm to 732nm which just implies more experimental effort with the current set-up. The only difference between the two methods is that by indirect shelving all Zeeman sublevels are populated with some probability whereas the π -pulse singles out one level. This is of no concern here since the lifetime is independent of magnetic quantum number (Wigner-Eckert theorem).

Furthermore, because that level is part of the closed 3-level fluorescence cycle used for state detection its population cannot be probed with that state detection scheme. In that sense the $D_{3/2}$ level is not a shelved state. The method used here is that prior to state detection the decayed population is transferred to the $D_{5/2}$ shelving state. The measured excitation divided by the shelving probability then corresponds to the decay from the $D_{3/2}$ level and the analysis is analogous to the one in the previous section. The shelving is achieved by coherent excitation. However, it must be taken into account that the $D_{3/2}$ state may decay into both Zeeman sublevels of the $S_{1/2}$ ground state. Hence two π -pulses from both sublevels are required to transfer all decayed population to the D-state. In this case the two $\Delta m = 2$ transitions ($m = -1/2$ to $m = -5/2$ and $m = 1/2$ to $m = 5/2$) are chosen. The combined transfer efficiency of the two pulses is determined in the first part of the pulse sequence by measuring the excitation without

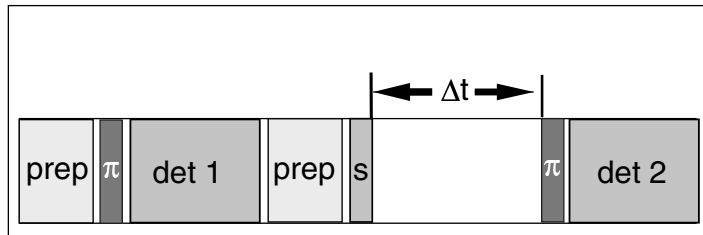


Figure 5.3: Simplified pulse scheme for the $D_{3/2}$ lifetime measurement. It consists of a measurement of the π -pulse transfer efficiency on the $S_{1/2}$ - $D_{5/2}$ transition (prep, π and det1); $D_{3/2}$ -state preparation (prep, s); waiting period Δt and state detection (π and det2). The waiting time is varied between 25 ms and 5 s. For details of the pulse sequence see text.

optical pumping into the $S_{1/2}(m_j = -1/2)$ ground state after Doppler cooling.

The complete laser pulse sequences applied to the ion for the measurement of the $D_{3/2}$ -level lifetime is composed of three steps (c.f. Fig. 5.3):

1. Measurement of transfer efficiency P_π : state preparation and Doppler cooling, consisting of 2 ms of Doppler cooling (397 nm and 866 nm light), repumping from the $D_{5/2}$ level (854 nm light) and spontaneous decay into the $S_{1/2}(m=-1/2)$ or ($m=+1/2$) Zeeman sublevel; π -pulses on the $S_{1/2}$ to $D_{5/2}$ transitions ($m_j = -1/2$ to $m_j = -5/2$ and $m_j = 1/2$ to $m_j = 5/2$); state detection for 3.5 ms by recording the fluorescence on the $S_{1/2} - P_{1/2}$ transition with a photomultiplier.

2. State preparation and shelving in the $D_{3/2}$ -level: 2 ms of Doppler cooling (397 nm and 866 nm light), repumping from the $D_{5/2}$ level (854 nm light) and optical pumping into the $S_{1/2}(m=-1/2)$ Zeeman sublevel (397 nm σ^+ polarised light); shelving pulse at 397 nm for a few μs .

3. Measurement of decay probability: free decay for a variable delay time; π -pulses on the $S_{1/2}$ to $D_{5/2}$ transitions ($m_j = -1/2$ to $m_j = -5/2$ and $m_j = 1/2$ to $m_j = 5/2$); state detection for 3.5 ms by recording the fluorescence on the $S_{1/2} - P_{1/2}$ transition with a photomultiplier.

Finally, it should be mentioned that one problematic issue of this scheme is its sensitivity to vibrational heating of the ion. A π -pulse only has high transfer efficiency if the ion is in the Lamb-Dicke regime. When the factor $\eta^2 n$ becomes significant both the Rabi frequency and the maximum transfer decrease. For example, given a heating rate of $0.1 ms^{-1}$ as for the ring trap the mean vibrational quantum number has increased to ≈ 100 after a delay time of 1 second (without cooling). Nevertheless, this problem is not fundamentally limiting this scheme. Either the delay time must be limited to the time scale where heating is still negligible ($\lesssim 500 ms$). Alternatively, the delay time must be inserted in the first part of the pulse sequence as well (before the π -pulse), to measure the appropriate shelving probability with the heated ion. For longer times this implies almost a doubling of the measuring time in addition to fewer successful experiments due to inefficient shelving. For faster data acquisition and hence higher precision in the result, the $D_{3/2}$ lifetime measurement was conducted in the linear Paul trap. The heating effect is treated along with the other systematic errors.

5.3.2 Results and Discussion

The measured $D_{3/2}$ excitation is plotted against delay time in fig.5.4. Again, the data have been fitted using the least squares method and the fit function $(1 - p) = e^{-\Delta t/\tau}$. Here, p denotes the corrected decay probability $p = P_{ex}/P_\pi$, the detected excitation of the $D_{5/2}$ level P_{ex} corrected for the near-unity shelving probability P_π directly after Doppler cooling. It is typically 0.98-0.99 on average. It should be noted that the actual P_π for each P_{ex} cannot be known exactly. It lies within the quantum projection noise

5 Lifetime Measurements

(QPN) limited error of the P_π measured in the first part of the pulse sequence⁶. In that sense there is no correlation between the two. Hence it is more appropriate to use the average of P_π over the whole dataset for one delay time. The output variables from the fit are $\tau = 1176(11)\text{ms}$ with $\chi^2_\nu = 0.68$. The reduced Chi-squared parameter indicates consistency with an exponential decay.

Again, systematic errors due to residual light have to be investigated. The shortening effects include residual light during the delay interval at 866nm or 850nm which de-excites via the $P_{1/2}$ and $P_{3/2}$ respectively and results in a faster effective rate. The main source of light at 866nm is the corresponding diode laser itself. Since the single pass AOM attenuation of 20dB was wholly insufficient (see figure 5.5) a fast mechanical shutter has been installed which remains closed throughout the entire waiting period. The fluorescence background of the 854nm diode laser at 866nm was found to be negligible.

Light at 850nm would mainly originate from the fluorescence background of the 854nm diode laser (repumper). The double pass AOM attenuation was proven to be sufficient, no effect could be measured within a 5% error even if the laser was on at full intensity during the whole waiting time.

The shortening effects are not obviously detectable because they only increase the decay rate while the functional shape of the decay curve remains the same. The main concern here is the 866nm light and extreme care has been taken to ensure that the shutter was indeed closed during the delay time. Before the 397nm shelving pulse and between the π pulse and the second detection a 1 ms period has been inserted to allow for shutting time and jitter. During the lifetime measurements the correct shutting was checked on photodiodes behind beamsplitters in the beampath. In fact, the shutters close fast in about $400\mu\text{s}$ but the start time is not well defined and jitters by about $500\mu\text{s}$. To show the sensitivity of the measurement to residual 866 nm light the lifetime was measured with the shutter opened some time before the π -pulse, fig. 5.5.

Amongst the prolonging effects is residual blue light at 397 nm which might re-excite the ion after it has already decayed. The same applies for light at 729 nm. This re-pumping rate is inherent as an offset as pointed out already in $D_{5/2}$ lifetime analysis (section 5.2.2). The 397nm light is switched by two single pass AOM's in series (one before a fiber) with attenuation of $\approx 55\text{dB}$ attenuation plus 160 MHz detuning. To suppress the influence of 397nm laser light to the largest possible extent a mechanical shutter was installed in the beampath even though the lifetime was unchanged within a 4% errorbar compared to the one measured without a shutter. To give a limit on the systematic effect of any re-pumping source the same method as in section 5.2.2 is applied. The experimental data is fitted with the rate model function yielding a rate of $R = 3(10) \cdot 10^{-3}\text{s}^{-1}$. The variation for an simulated ideal data set is $\Delta R = 1.5 \cdot 10^{-2}\text{s}^{-1}$, so again it is hidden in the statistical error. From the simulation an upper limit for the

⁶The QPN noise is given by the binomial error $\Delta p = \sqrt{p(1-p)/N}$, e.g. $\Delta p = 0.014$ for $p = 0.98$ and 100 experiments

systematic error of $\Delta\tau = -2\text{ms}$ is obtained. More details on the simulations are found in appendix C.2.

Another source of systematic error is vibrational heating. Heating during the waiting time causes the transfer efficiency of the π -pulse P_π to decrease. Hence it is less than

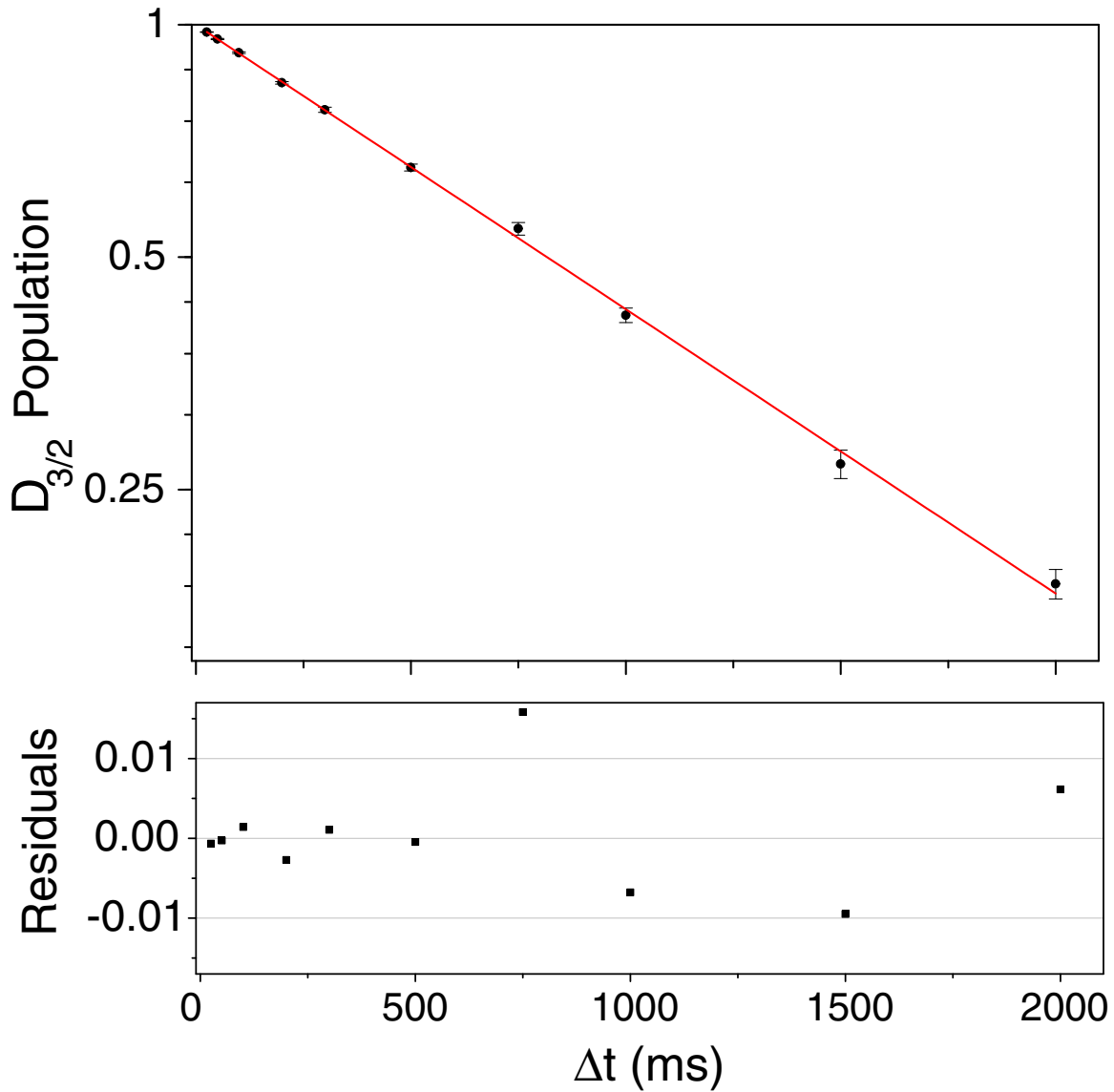


Figure 5.4: $D_{3/2}$ excitation for delay times from 50 to 2000 ms on a logarithmic scale. The solid line is a least-squares fit to the data using the exponential fit function $(1 - p) = e^{(-\Delta t/\tau)}$. The bottom plot shows the residuals, the difference between data points and fit. No significant systematics is noticeable.

5 Lifetime Measurements

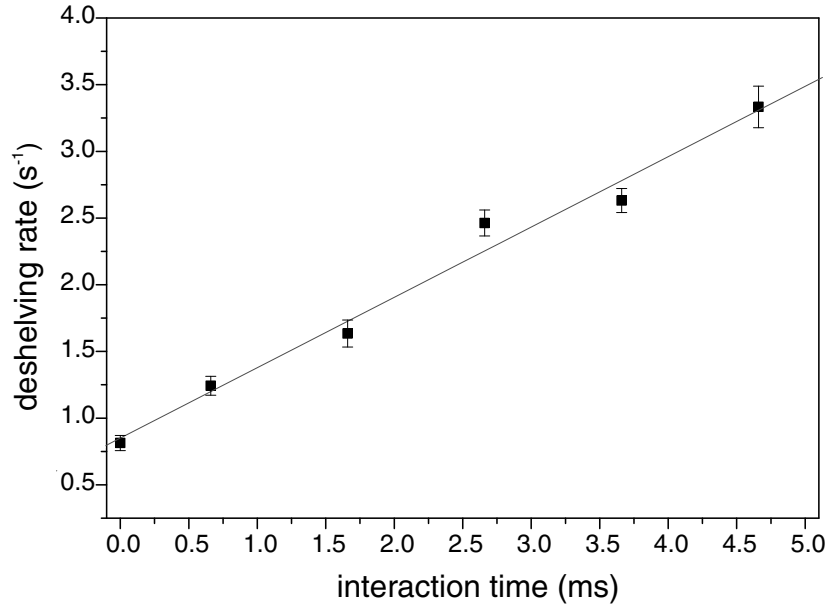


Figure 5.5: Effect of residual radiation at 866 nm: $D_{3/2}$ decay rate as a function of interaction times of 866nm light during the delay time. During the interaction time the shutter is open and the 866 nm beam is only attenuated by the AOM.

the one determined in the first part of the pulse sequence and the decay correction is too small, i.e. the real decay is higher than measured. This has been checked experimentally by recording the excitation after the π -pulse as function of waiting time. The average of all scans is shown in fig. 5.6. For hundred experiments the decrease of the excitation after 2 s lies within the QPN. If the efficiency P_π is written as $P_\pi(\Delta t) = 1 - a \cdot \Delta t$ the slope is determined $a = -4(2) \cdot 10^{-3} \text{s}^{-3}$. For this slope the systematic error computes to $\Delta\tau = -7\text{ms}$ (appendix C.3).

Finally, the detection error is considered, analogous to section 5.2.2. From simulated data sets with a detection error of $\varepsilon_2 = 1 \cdot 10^{-3}$ a systematic error for the lifetime of $\Delta\tau = +8\text{ms}$ is found (appendix C.1).

Collisional effects (quenching and j-mixing) and M1 transitions are neglected on grounds discussed in section 5.2.2.

Summarising the analysis, the lifetime for the $D_{3/2}$ level is given as:

$$\tau_{(3/2)} = 1176(11)\text{ms (statistical)} - 2\text{ms (repumping rate)} - 7\text{ms (heating)} + 8\text{ms (detection error)}$$

5.4 Comparison with other Experimental and Theoretical Results

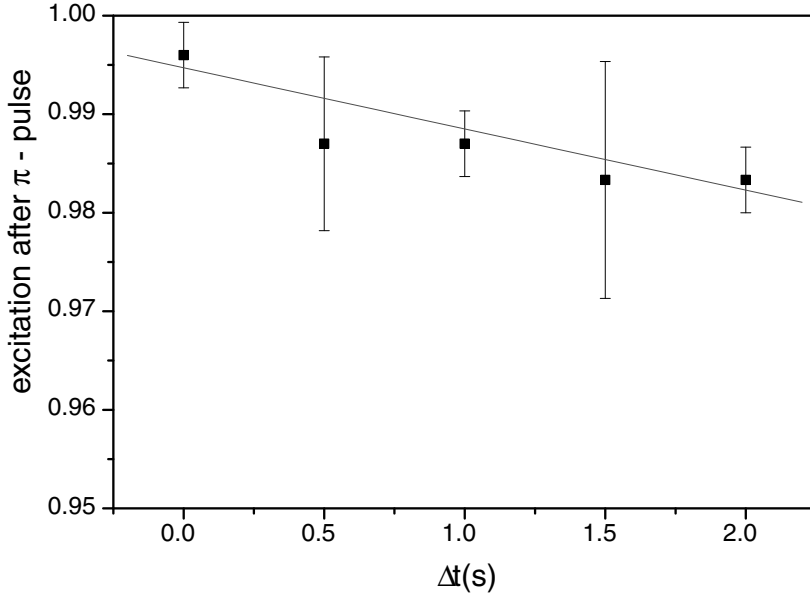


Figure 5.6: Vibrational heating causes a decrease in the transfer efficiency of the π -pulse: Average transfer efficiency of the π -pulse as a function of waiting time Δt . The linear slope is determined as $a = -4(2) \cdot 10^{-3}\text{s}^{-1}$.

5.4 Comparison with other Experimental and Theoretical Results

Due to the scientific interest of the calcium lifetimes several theoretical and experimental works have been published. Figure 5.7 shows an overview over all experimental and theoretical results for the lifetime of the $D_{5/2}$ and $D_{3/2}$ states, respectively [100–106]. It is remarkable that the theoretical predictions scatter rather widely, with no visible convergence while the experimental results show a trend towards longer lifetimes in the recent years as more systematic errors are identified and minimised. In general, the theoretical problem can be stated as calculating the D and S electron wavefunctions to find the reduced transition matrix element for the quadrupole operator between the S and D states. Many different methods with various approximations and higher order corrections have been developed. Here, just three different representative methods that yield a comparably short, long and intermediate value, respectively, for the lifetime of the $D_{5/2}$ level are briefly described.

Kim and Ali [101] apply the multiconfiguration Dirac-Fock (MCDF) method and obtain as a result a relatively short lifetime of $\tau = 950$ ms. The relativistic configuration wavefunctions are generated by minimising the energy of the radial Dirac-Fock functions for each level separately. Core-electron correlations are not considered in this

5 Lifetime Measurements

model.

Vaeck *et al.* [104] include valence correlations in a multiconfiguration Hartree-Fock (MCHF) approach and find a reasonable value of $\tau = 1140$ ms.

Guet and Johnson [102] use relativistic many-body perturbation theory (MBPT) up to third order including semi-empirical scaling of orbitals and predict $\tau = 1236$ ms. By solving the Dirac-Hartree-Fock (DHF) equation the frozen-core HF potential is found. This is used as the effective potential for the valence electron which can then

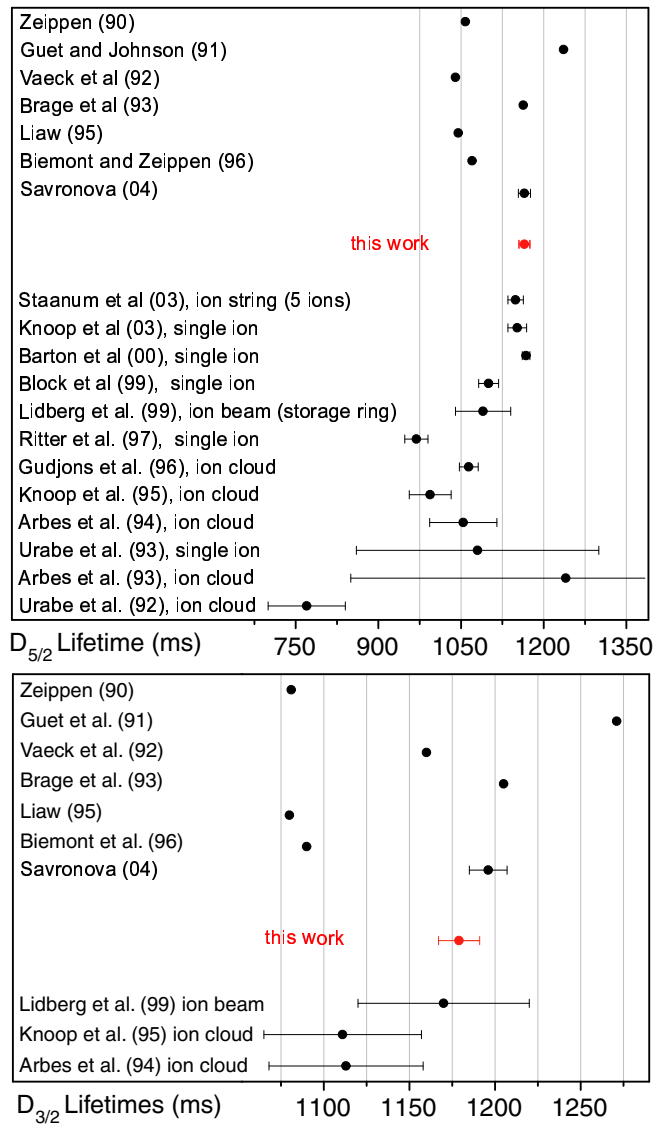


Figure 5.7: All experimental and theoretical results for the lifetime of the $D_{5/2}$ (top) and $D_{3/2}$ (bottom) states, respectively.

5.4 Comparison with other Experimental and Theoretical Results

be described with a one- electron Hamiltonian.

Note that the publication of the lifetime results (see Appendix F) was done in collaboration with the theoretian M. Safronova. She calculates a lifetime of $\tau = 1165$ (11) ns using a relativistic all-order MBPT method (ab initio). A good review on the status of the Ca^+ lifetime theory can be found in Ref.[100].

In comparison with previous work it can be concluded here that our lifetime result for the $D_{5/2}$ level agrees with and thereby confirms the most precise value of Barton *et al.* using an alternative measurement approach. In addition, the result for the $D_{3/2}$ level represents the first single ion measurement and reduces the statistical uncertainty of the previous value for the lifetime by a factor of four.

5 *Lifetime Measurements*

6 Enhanced Spontaneous Emission

6.1 Ion-Cavity Coupling

6.1.1 Coherent Coupling

Perhaps the most stringent characterisation of a cavity stabilisation is to coherently excite a single ion with the cavity light field. Perturbations or oscillations of the cavity length induced by electronic or acoustical noise are observable in the light transmission signal of the cavity output. During coherent excitation these fluctuations are translated to phase fluctuations of the light inside the cavity, equivalent to a broadening of the laser linewidth reducing the coherent interaction time. Rabi oscillations on the carrier transition driven by light coupled into the cavity are shown in fig. 6.1. The damping is considerably higher than for simple laser excitation, compare with fig. 4.1c, nonetheless the population transfer probability for a π -pulse is still 90%. Care must be taken to determine the carrier transition frequency while the cavity is locked to include the ac-Stark shift which is discussed in section 6.2.

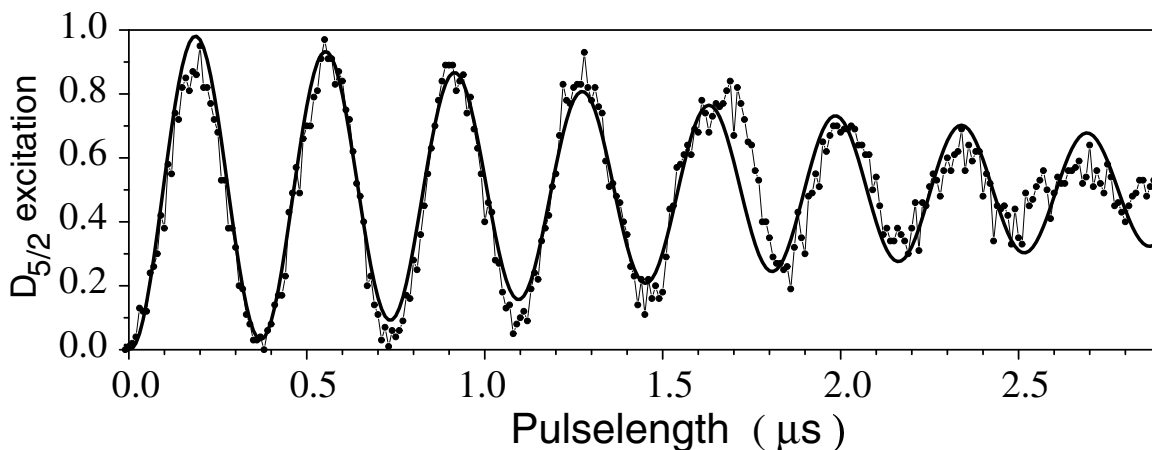


Figure 6.1: Fast Rabi oscillations driven by the cavity light field.

6.1.2 Standing Wave Pattern

A doppler-cooled ion in the Lamb-Dick regime has a wavepacket extension of much less than the excitation wavelength and can thus be used as a nanoscopic probe of the standing wave (SW) field spatial variation. This was first shown in [33]. The SW pattern has previously been mapped with the same set-up by a cavity scanning technique before the cavity stabilization was implemented [34, 46]. Excitation spectra were recorded by scanning the laser detuning over the carrier resonance. The offset voltage of both scan PZT and offset PZT was then varied simultaneously in such a way that the SW in the cavity is shifted longitudinally with respect to the location of the ion. The position-dependent excitation probability was determined by fitting each spectra with a Lorentzian and adopting the peak value. From fitting a \sin^2 function to the datapoints a very high contrast ratio or so-called visibility V of $V = 96.3(2.6)\%$ is obtained. The maximum of the excitation corresponds to the node of the optical field since the atomic quadrupole moment couples to the gradient of the electric field. See [46] or the thesis of A.B. Mundt [113] for all details. That procedure, however, is very time consuming in both the experiment and analysis since each datapoint is an

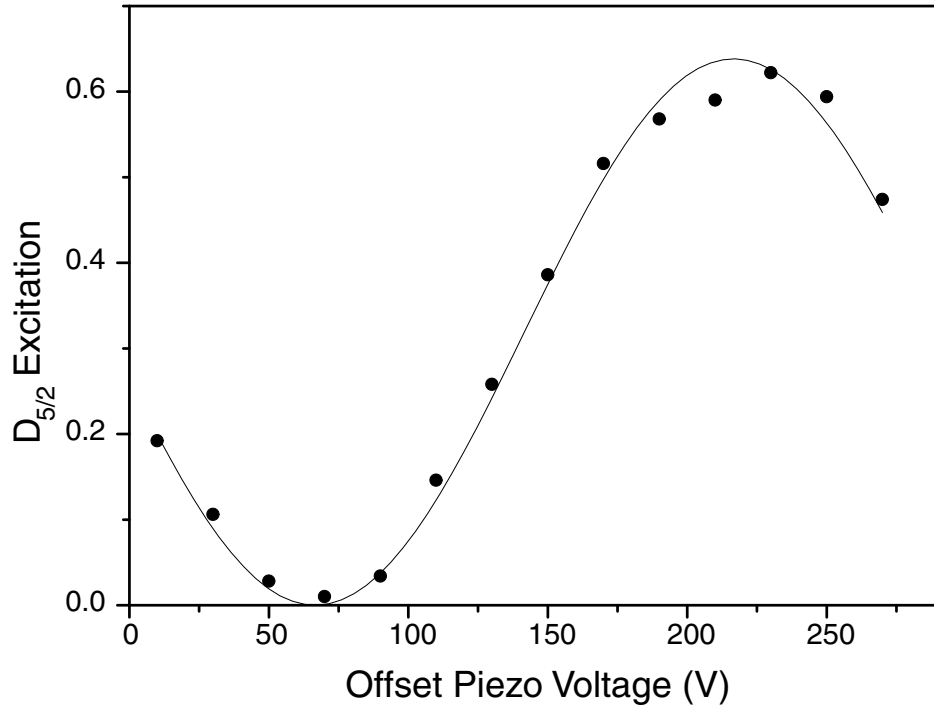


Figure 6.2: SW pattern of the intra cavity field mapped by recording the coherent excitation after a short light pulse. Due to good localisation of the ion the visibility is close to unity.

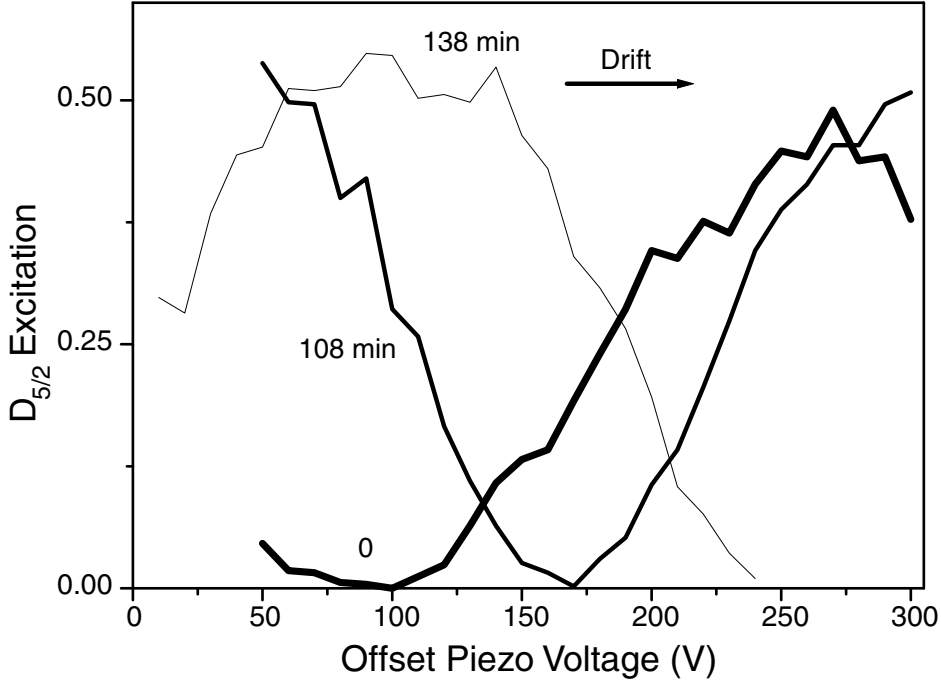


Figure 6.3: Cavity drift: Example of SW-patterns shifting over time.

amplitude derived from a spectrum comprising 60 points. Driving Rabi flops through the locked cavity allows the SW to be mapped much faster by simply recording the excitation probability after a short pulse while varying one PZT offset voltage. (Note that the cavity stays resonant because the integrator on the locking PZT compensates for the offset and the cavity is shifted longitudinally.) The exact pulse length should be set to the $\pi/2$ time of the maximum Rabi frequency in the node to ensure a pure \sin^2 position dependence. It will become clear in the next chapter that a fast and precise mapping of the SW is crucial when drifts and other experimental imperfections threaten to conceal the small cavity effect on the spontaneous emission rate.

In fig. 6.2 the SW pattern determined by the coherent excitation technique is shown. The visibility is close to unity. The main reason for non-unity contrast is the wavepacket extension discussed below in 6.4. The thermal drift of the cavity can be neglected here when the measurement duration is small enough¹. The thermal drift of the cavity has been measured over several hours during the lifetime measurements. Examples of three SW patterns recorded approximately $1\frac{1}{2}$ hours apart are depicted in fig. 6.3.

In fig. 6.4 the phase (i.e. the voltage at which the minimum occurs) of the fitted SW curves is plotted against time and a straight-line fit to the linear part of the data yields

¹Here the measurement time T was $T = 20 \text{ points} \times (500 \text{ experiments/point} \times 5 \text{ ms/experiment} + \approx 2 \text{ s to change offset voltage by hand}) \approx 90 \text{ s}$.

6 Enhanced Spontaneous Emission

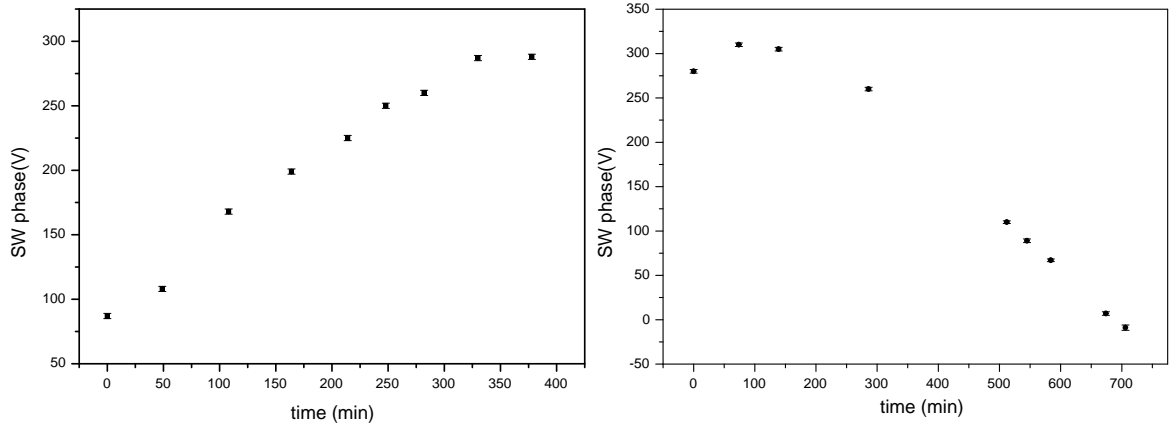


Figure 6.4: Cavity drift over several hours on two different days: The phase of each SW-pattern is plotted against time. The drift is typically about $\lambda/4$ in 4 hours.

a slope of $0.62(1)\text{V}/\text{min}$ corresponding to a drift of $\lambda/4$ in 3.9 hours. The drift varies from day-to-day operation but was always found around that order of magnitude. For the lifetime measurements which take more time the drift must be taken into account to find the corrected average position in the phase the SW. (The voltage range of the offset PZT unfortunately barely covers one FSR of the cavity. This means that if the turning point of the drift (around 300 V in fig. 6.4) is slightly larger the mode is out of reach of the PZT offset (305 V max) and a new mode of the transfer laser for double resonance must be found.

6.1.3 Lateral Positioning

The atom-cavity coupling g depends not only on the longitudinal position (SW phase) but also on the transverse position in the (gaussian) waist of the cavity mode². Because the cavity-trap set up cannot be assembled to that precision and, in any case, misalignment during bakeout would not be controllable the trap is mounted on a 3-point mirror-holder-style-mount to allow relative positioning of the ion with respect to the cavity mode, see setup figure 3.3. For the optimization of the lateral position the trap was moved in the lateral plane by the micrometer screws and the Rabi frequency which is proportional to the coupling strength was measured. The plot is displayed in fig 6.5.

The exact position in the lateral plane was determined by shining a He-Ne laser beam through the cavity and monitoring the image of the trap behind the cavity on a digitised CCD-camera. Four points on the ring projection of the trap were used

²the longitudinal envelope of the SW can be neglected here since the confocal parameter of the cavity mode ($b=2.5\text{ cm}$) is larger than the cavity length

as markers to trace its position. An independent check was done by calculating the trap's relative position from the reading on the micrometerscrew's scale taking the dimensions of the mount into account.

For each point it was first ensured that the ion was kept at the node by maximising the Rabi frequency with the PZT offset. In addition all laser beams (Doppler cooling, repumper and 729 beams) plus the PMT and CCD-camera objectives had to be re-aligned after each trap movement which makes the whole procedure extremely time-consuming and tedious and thereby limits the spatial resolution. From the error in Rabi frequency (shot-to-shot variation compared to the variation at adjacent positions) and

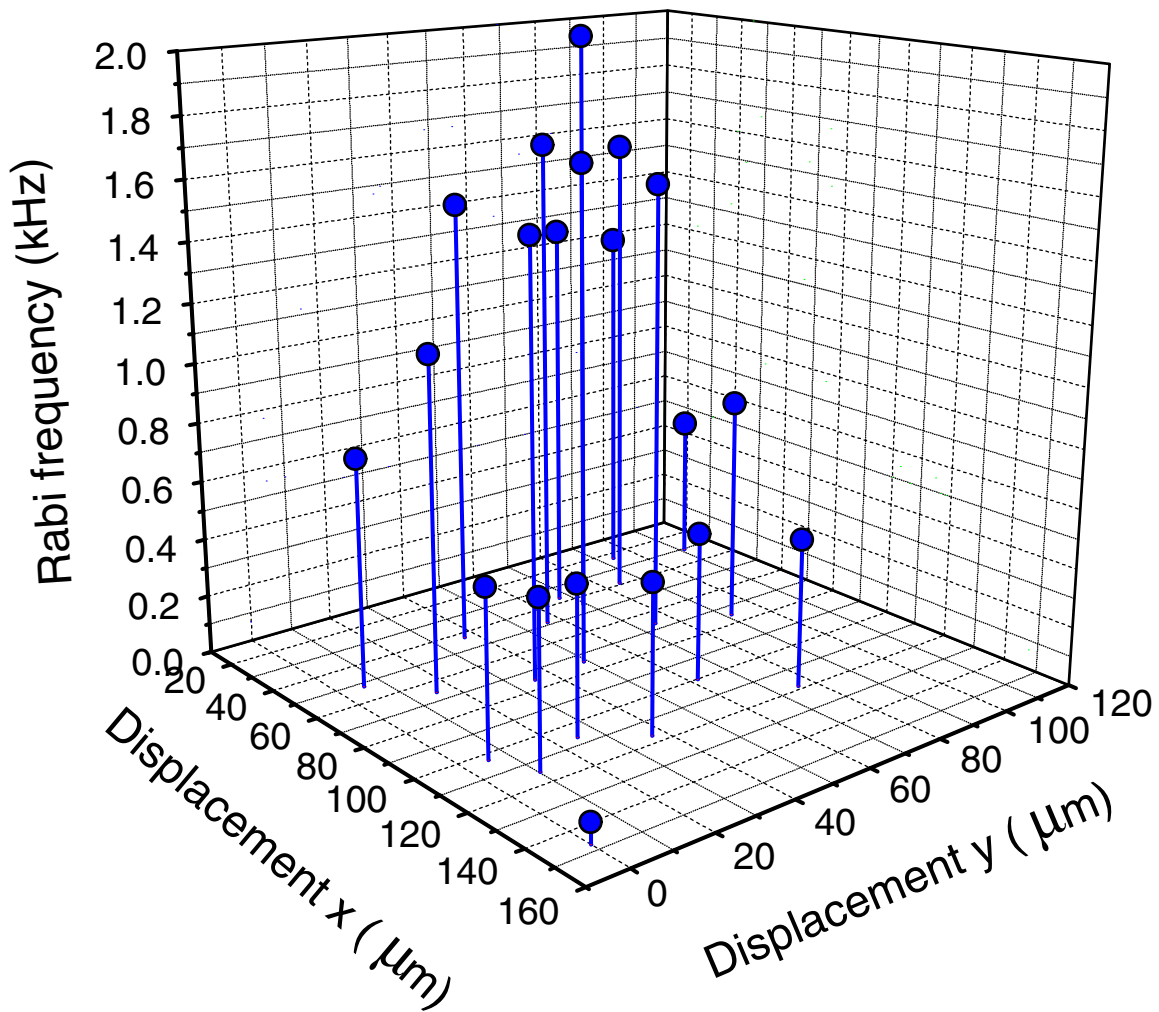


Figure 6.5: Transverse position in the TEM_{00} cavity mode: The measured Rabi frequency is plotted against position of the ion in the lateral x-y plane. The ion trap was shifted by micrometer screws on the mount

6 Enhanced Spontaneous Emission

the error in the measured position of the trap, the precision of the lateral positioning is estimated as $20\mu\text{m}$.

6.2 AC-Stark Shift

Although the transfer light inside the cavity is far-detuned, coupling to the P-levels (dipole) or the D-level (quadrupole) results in an ac-stark shift of the S-D transition frequency. It has to be kept in mind that even though only little power is required for the stabilisation (minimum power is about $5\mu\text{W}$ in transmission) the power inside the cavity is enhanced by a factor of $F/\pi \simeq 4100$ implying a maximum intensity of $2.3 \cdot 10^{-4} \text{mW}/\mu\text{m}^2$ at the ion. Of course, the ac-Stark shift is also modulated sinusoidally in the SW. At a fixed phase of the standing wave the ac-Stark shift has been measured by spectroscopy on the $S_{1/2} - D_{5/2}$ transition as a function of the transfer light power. The linear dependence is verified in fig.6.6a.

Unfortunately, the transfer wavelength cannot be chosen arbitrarily far-detuned. A compromise must be made between detuning and cavity finesse at the transfer laser wavelength. Away from the design wavelength of the transition it drops considerably. At 785 nm the cavity finesse is about 13000 which is still good enough for a narrow linewidth stabilisation.

The ac-Stark shift originates from coupling to other transitions which implies off-resonant excitation to the short lived P-levels. This increases the measured natural decay from the $D_{5/2}$ level, shown in fig. 6.6b. It is therefore desired to use the minimum possible power for the transfer lock during the lifetime measurements. In this experiment the minimum power is $5\mu\text{W}$ in transmission corresponding to a maximum

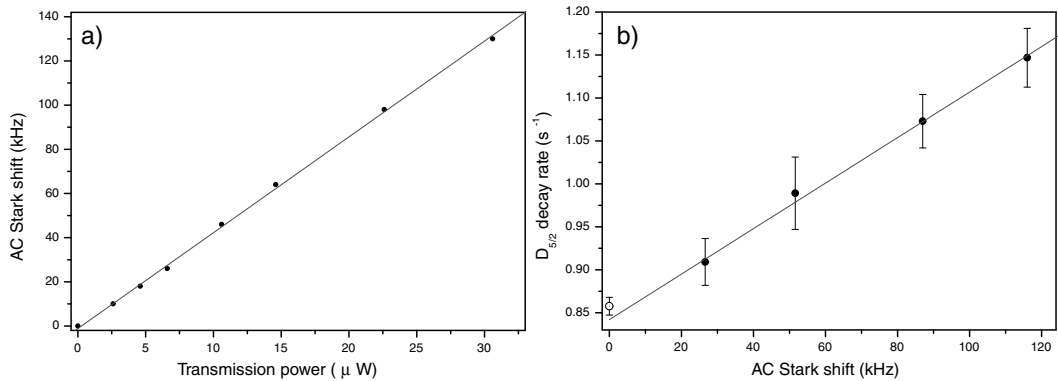


Figure 6.6: **a)** Linear dependence of ac-Stark shift against transmission power of the transfer light. The ion's relative position in the SW was kept constant. **b)** The ac-Stark shift induces an additional decay rate by off-resonant excitation to the short lived P-levels.

ac-Stark shift of 16 kHz or an additional deshelling rate of $\gamma = 0.04\text{s}^{-1}$ which amounts to $\approx 5\%$ lifetime reduction in the antinode of the transfer light SW.

6.3 Mapping the Cavity Vacuum Field

It is described in section 2.3 that spontaneous emission is maximally enhanced by the Purcell factor $(2C + 1)$ at the node of the vacuum SW in the cavity: $\gamma \rightarrow \gamma_0(1 + 2C)$. Since the coupling parameter g and hence C depends on the phase of the vacuum SW (like $\sin^2(\phi)$) the decay rate is modulated accordingly. By measuring the $D_{5/2}$ lifetime of the ion placed at different phases along the standing wave the enhanced vacuum field inside the cavity is mapped. The lifetime is determined by measuring the decay for a single delay time only ($\Delta t = 50\text{ms}$) and using the exponential law verified in the previous chapter: $\tau = \frac{-\Delta t}{\ln(1-p)}$. Considerations on the optimal delay time for which the statistical error decreases the fastest with measurement time are formulated in the appendix. The lifetime measurements at different positions in the vacuum SW are shown in fig. 6.8.

Each data point in fig. 6.8 consists of an average of up to four points each comprised of 20000 individual decay measurements shown in fig. 6.7. During the 19 min for

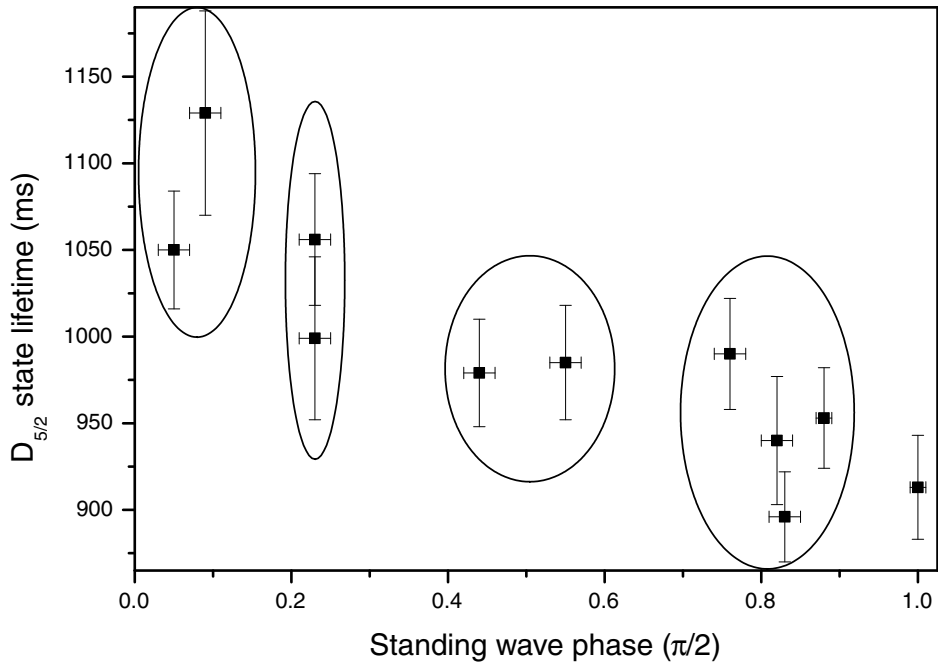


Figure 6.7: All individual lifetime measured at various points in the vacuum SW. The circles indicate the points that are binned to yield figure 6.8

6 Enhanced Spontaneous Emission

20000 experiments the cavity drift is about 15 nm ($\lambda/50$). This position drift is not a systematic error in the phase but corresponds to an averaging over the sinusoidal variation and a loss of contrast. The maximum lifetime reduction in the node of the vacuum SW is $15 \pm 5\%$.

6.4 Discussion

The results in fig. 6.8 leave two significant points for discussion: On the one hand is the maximal lifetime reduction of 15% in the node of the SW less than the calculated effect of 52%, on the other hand, the lifetime in the antinode τ_a is less than the expected free-space lifetime ($\tau_{fs} = 1168(9)\text{ms}$) determined in chapter 5.2.

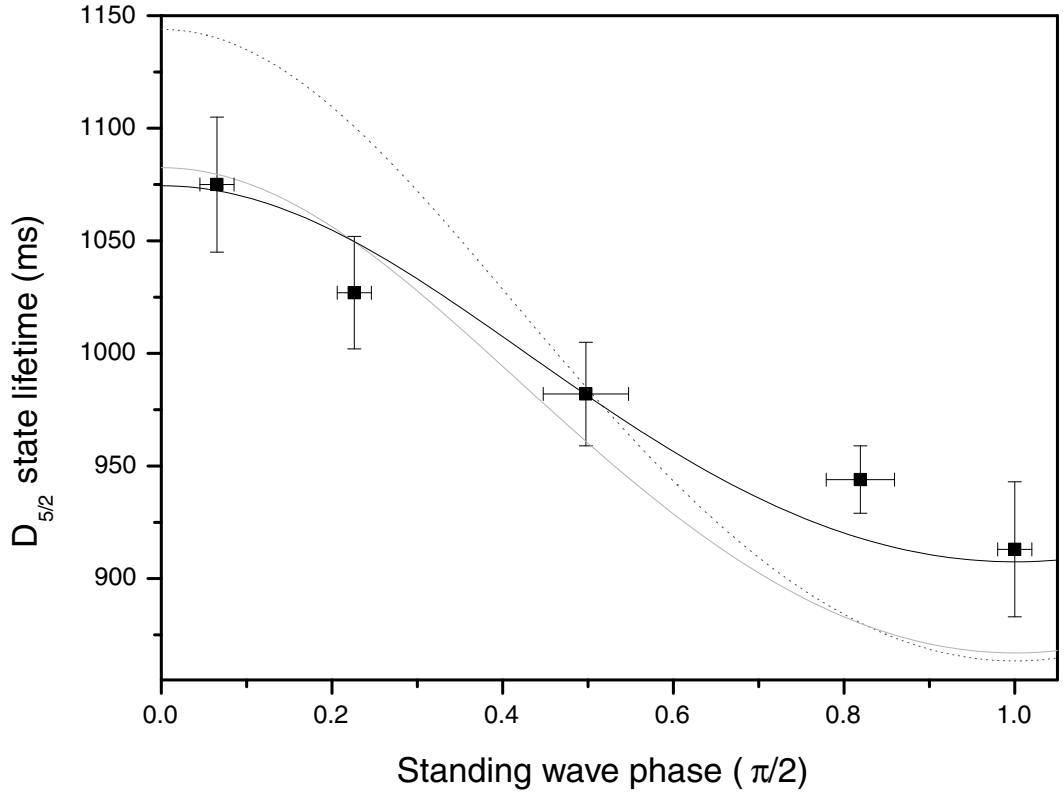


Figure 6.8: Combined experimental $D_{5/2}$ lifetimes at five different points in the vacuum SW. The dotted line shows a simulation of the effective Purcell effect neglecting the additional transfer light deshelving. The light grey solid line includes the additional deshelving of $\gamma_{add} = 0.04 \text{ s}^{-1}$ using equation 6.1. The black solid line is a simulation assuming $C_{eff}=0.15$.

The non-unity visibility V of the SW³ considers cavity drift and wavepacket extension that smear out the sinusoidal variation: $\sin^2 \rightarrow [\frac{(1-V)}{2} + V \sin^2(\phi)]$. For a Gaussian envelope of width a the visibility decreases as $V = \exp(-2(2\pi a/\lambda))$ [110] which is derived from a convolution integral of a Gaussian with a \sin^2 function. The effective envelope consists of the instantaneous wavepacket extension and the drift. The wavepacket extension is of the order of 20 nm, considering a heating rate of 0.1 ms^{-1} during the 50 ms delay time, whereas the drift during one measurement amounts to 15 nm. Hence, the SW visibility reduces to 90%.

Furthermore, C_0 is replaced by an effective C_{eff} due to several experimental imperfections reducing the Purcell factor: First, disturbance of the cavity lock (acoustical or electrical) leads to an inhomogeneous broadening of the cavity linewidth, recall fig. 3.9 in section 3.6. The resulting effective finesse is 22000 which reduces the cooperativity to $0.62C_0$. Second, a suboptimal transverse position of the ion in the waist of the cavity mode reduces the coupling g , see section 6.1.3. The positioning achieves an estimated precision of $20\mu\text{m}$ reducing the cooperativity further to $0.57C_0$. The effective cooperativity then computes to $C_{eff} = 0.62 \times 0.57 \times C_0 = 0.184$.

This implies that in the antinode ($\phi = 0$) $\gamma_a = 1.02\gamma_0$, i.e. $\tau_a = 0.98\tau_0$, whereas in the node ($\phi = \pi/2$) $\gamma_n = 1.35\gamma_0$, i.e. $\tau_n = 0.74\tau_0$, corresponding to a 26% lifetime reduction.

Finally, the influence of the transfer light on the lifetime due to the ac-Stark shift is considered (see section 6.2). The phase of the transfer SW ϕ' in the cavity was not determined independently but is, in general, different than the vacuum SW ϕ . The short lifetime in the antinode of $\tau = 1075(30)\text{ms}$ suggests the following case scenario: The transfer light SW phase is such that it decreases the lifetime in the antinode by 5% due to the additional deshelling rate of 0.04 s^{-1} and leaves the minimum lifetime in the SW node unchanged: $\phi' = \phi + \pi/2$. The total expected experimental enhancement is now written as (c.f equation 2.25):

$$\gamma = (\gamma_0 + 0.04 \times [\frac{(1-V)}{2} + V \cos^2(\phi)]) \times [1 + 2C_{eff}\{\frac{(1-V)}{2} + V \sin^2(\phi)\}] \quad (6.1)$$

This resulting expected lifetime variation from equation 6.1 is included in figure 6.8 (grey line). So including the influence of the transfer laser the maximum lifetime reduction is expected to be $\tau_n = 0.74 \cdot 0.95 \cdot \tau_0$ corresponding to 22% which is in reasonable agreement with the experimental result.

³Defined as $V = (\text{max} - \text{min}) / (\text{max} + \text{min})$

6 *Enhanced Spontaneous Emission*

7 Summary and Conclusion

In summary, this work reports on an experiment that explores the deterministic interaction of a single trapped Ca^+ ion with the modified vacuum field inside a high finesse optical resonator. Such a system could be the basic building block for, e.g. a quantum information interface, interconverting atomic and photonic qubits. The experimental requirements and challenges for controlled ion-cavity coupling are described. Furthermore, the single ion was well characterised by spectroscopy and coherent dynamics. After Doppler cooling, the ion is well localised in the cavity standing wave. Problems like vibrational heating were analysed before the CQED experiments could be performed. The spatial variation of the spontaneous emission rate has been investigated by measuring the lifetime of the $\text{D}_{5/2}$ level at different points in the vacuum standing wave of the cavity. In the node a maximal lifetime reduction of 15(5)% was observed (Purcell effect). Various experimental imperfections lead to the reduction of the theoretically expected effect from 50% to 22%.

For the lifetime measurement a novel technique based on deterministic excitation and quantum state detection has been introduced. This new method has two distinct advantages. It allows the precise lifetime measurement of both metastable D-levels, $\text{D}_{5/2}$ and $\text{D}_{3/2}$, using a single ion. In addition, systematic errors can be eliminated to the largest possible extent because no light interacts with the ion during the decay. Residual systematic effects, such as detection errors, have been precisely accounted for by using error models and simulations. Using this method, a lifetime of $\tau = 1168(9)$ ms for the $\text{D}_{5/2}$ level was found which agrees well with previous high precision measurements. The $\text{D}_{3/2}$ lifetime result of $\tau = 1176(11)$ ms is the first from a single ion and exceeds previous results by a factor of four in precision.

Currently, the next generation experiment is being assembled in the laboratory for the investigation of further CQED effects, based on the experience and expertise developed in the experiment characterised here. The new design will incorporate a linear Paul trap to allow for the coupling of two or more ions to a common cavity mode. An important technical detail is that the cavity assembly is maneuverable instead of the trap assembly. This will allow a simplified lateral positioning of the ion with respect to the cavity mode. Furthermore, a near-concentric cavity ($< 20\mu\text{m}$ waist) and higher reflectivity mirrors ($F \approx 80000$) produce a higher coupling so that CQED effects are more pronounced. The cavity will be resonant to the $\text{P}_{3/2}$ - $\text{D}_{5/2}$ dipole transition at 854 nm. The coupling parameters (g, κ, Γ) all shift towards higher frequencies in the MHz

7 Summary and Conclusion

regime, resulting in the 'weak coupling regime'. A major goal would be the realisation of a single photon source and an atom-photon interface, both using a stimulated rapid adiabatic passage (STIRAP) process. Detailed theoretical studies for using STIRAP in the new set-up to produce single photons have already been done [120].

This symbiosis of both, cavity and linear trap technology developed in this group will provide an improved, versatile tool for exploring CQED at the most refined level.

A Loading a Single Ion: Tricks and Hints

As a summary for loading ions the following checklist must be considered:

- all required power supplies must be on, including all GPIB-devices, start LabView programme on PC.
- 397nm and 866nm lasers on correct wavelength and locked.
- ionization lasers on resonance (hollow cathode signal) and both beams overlapped at the trap
- light at the experiment and focussed through the trap,
- trap RF-power $\approx 0.5W$ on RF-powermeter, no RF-reflection
- switch oven on ($I \sim 2.1A$)
- PMT shutter closed (and camera shutter) closed to protect against stray light from ionization lasers

When all beams are well aligned and on resonance loading takes of the order of minutes but minor deadadjustments might easily lead to an extention of the loading process beyond 10 min. Often more than ion is loaded. Then by blocking the repumper or blue-detuning the 397 nm doppler light ions can be heated out of the trap until one single ion is left. An indication for the number of ions is given by various measures: the PMT countrate, the $S_{1/2} - P_{1/2}$ lineshape, the image on the CCD-camera or quantum jump levels. More than 2 ions cannot crystallise in the small trap and they form a hot cloud. Hence PMT counts are rather low, the lineshape is broad and the image on the camera is a fuzzy cloud. When the 729 nm light is present at the ions quantum jumps can be induced. When an ion is exited to the $D_{5/2}$ it is decoupled from the fluorescence cycle ('shelved') and the fluorescence level changes. For a few, e.g. 3, ions then 4 distinct fluorescence levels can be identified corresponding to 0,1,2 and 3 excited ions.

A Loading a Single Ion: Tricks and Hints

B Statistical Methods for Data Analysis

Every experiment consists of only a finite number of measurements, so every measured physical quantity is associated with a statistical error bar that accounts for an uncertainty in the measuring process due to non-perfect measuring equipment or fluctuations in the physical system itself. In the language of statistics the measured data is a subset of a parent distribution. Translated back into the language of physics, the parent distribution is an imaginary 'ideal' data set obtained from infinitely many measurements assuming a certain model function. One task of statistics is to estimate certain parameters that best match the one of the parent distribution (if the parent distribution is known). This is usually done by fitting a model function to the data using an appropriate fit method and find the best-fit model parameters. Another question is whether the measured data really *is* a subset of the expected parent distribution, i.e. whether the model is correct.

Transferred to the specific case in this work the statistical questions are: Is the measured decay indeed a purely exponential decay and what is the decay constant and its statistical error. Before the data can be fitted with a model function the relevant fit method must be found. The most common method is a least-squares fit which works on minimising χ^2 , defined as the sum of the squares of differences of data (x_i, y_i) and a model function $y(x_i)$, weighted by the experimental uncertainties σ_i [108]:

$$\chi^2 \equiv \sum_i \left\{ \frac{1}{\sigma_i^2} [y_i - y(x_i)]^2 \right\} \quad (\text{B.1})$$

It is crucial to note here that this method is based on the assumption that the parent set of each data point is distributed normally (Gauss distribution). If this is verified the fit procedure is a straight-forward numerical problem. An important parameter of a least-squares fit is the so-called reduced χ_ν^2 which can be written as

$$\chi_\nu^2 = \frac{\chi^2}{\nu} = \frac{s^2}{\langle \sigma^2 \rangle} \quad (\text{B.2})$$

where ν is denotes the degrees of freedom of the fit (number of data points minus number of fit parameters) and s^2 is the variance of the fit. $\langle \sigma^2 \rangle$ is the weighted average

B Statistical Methods for Data Analysis

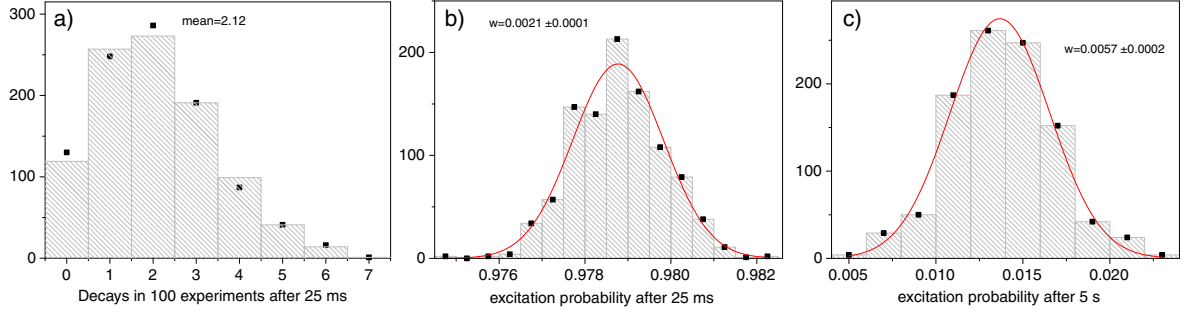


Figure B.1: 'Monte-Carlo' simulation results. **a)** Individual probabilities of finding a certain number of decays are distributed according to the binomial distribution, which is indicated by the square points. The total number of simulated decays in the histogram was 1000. The mean decay probability after 25 ms is 0.021. **b)** and **c)** The central limit theorem: the distribution of the means of a set of variables with arbitrary distribution is a Gaussian distribution. This is verified for the extreme cases of small and close to unity excitation probabilities. The binomial distribution is symmetric (Gaussian) only for $p = 0.5$.

of the individual variances. In this form the meaning of χ_ν^2 is most obvious: it is the ratio of the estimated variance to the parent variance which makes it a convenient measure for the goodness of the fit. For a reasonable fit χ_ν^2 is expected to be around 1. However, the interpretation of χ_ν^2 per se can be somewhat ambiguous, e.g. a large spread in the data cannot be distinguished from a bad choice of the parent function if χ_ν^2 is too large.

One way to answer statistical questions is to simulate random experimental data sets following the Monte-Carlo idea. In this case random data are generated using the fact that the decay probability for a given waiting time is distributed binomially¹ around a mean that is given by an exponential function. So for the particular experimental waiting times and number of measurements (the exact number used in section 5 for the $D_{3/2}$ and $D_{5/2}$ levels, respectively. Model lifetimes of $\tau = 1179\text{ms}$ and $\tau = 1165\text{ms}$ have been taken) an 'ideal' random data set is created from the parent function. The data set is *ideal* in the sense that it is known to be free of systematics and *random* in the sense that it is truly statistical. From an ensemble of such sets one can deduce many statistical properties, e.g. standard deviation, χ^2 distribution and the distribution of other parameters. One important result is the verification of the Gaussian distribution of the individual mean decay probabilities which is shown by the histogram plot in figure

¹The binomial probability distribution is the adequate description for physical processes involving exponential decay. It gives the probability P_{bino} of observing ν events in n trials. In one trial each event has probability p to occur, then $P_{bino} = \frac{n!}{\nu!(n-\nu)!} p^\nu (1-p)^{n-\nu}$.

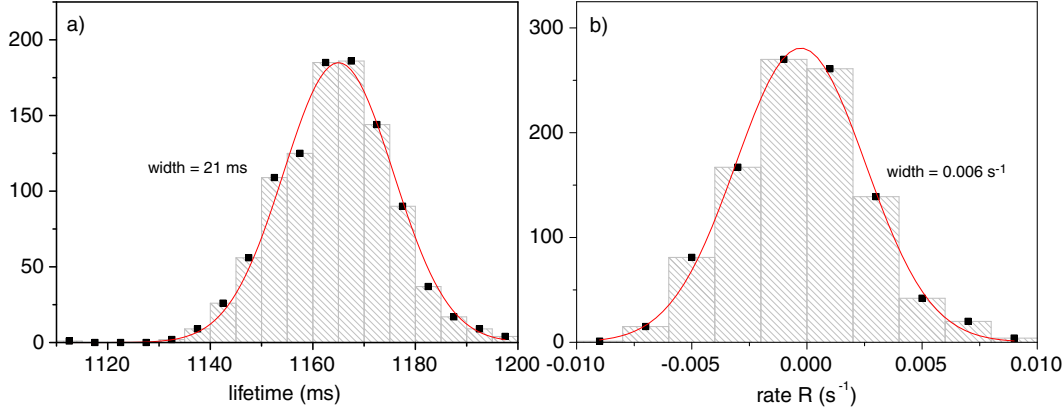


Figure B.2: Distribution of fit results from an ensemble of simulated data sets. Ideal parent distributions $1 - p = e^{-\Delta t/1165ms}$ were fitted with a model function $p_D = B + Ae^{-\Gamma'\Delta t}$ where $B = R/\Gamma'$, $A = 1 - R/\Gamma'$ and $\Gamma' = R + \Gamma$. $\bar{\tau} = 1165ms$ with standard deviation $\Delta\tau = 10ms$ and $\Delta R = 3 \cdot 10^{-3}s^{-1}$.

B.1 b,c. This is a result of the *central limit theorem* and justifies the least-squares fit to the decay probabilities. This also shows, for example, that a least-squares fit of a straight line to the logarithm of the decay is not appropriate. Another interesting result is the distribution of the fitted parameters τ and R . An ensemble of simulated data sets is fitted with an exponential function $p_D = B + Ae^{-\Gamma'\Delta t}$, where $B = R/\Gamma'$, $A = 1 - R/\Gamma'$ and $\Gamma' = R + \Gamma$, a model that includes a repumping rate, c.f. section C.2. As expected both distributions for $\tau (= 1/\Gamma)$ and R are Gaussian with mean $\bar{\tau} = 1165ms$ and $\bar{R} = 0s^{-1}$, the means of the parent distribution (fig. B.2 a,b). The scatter of the values, i.e. half the widths of the Gaussians, are the errors (1σ standard deviation) in each parameter for a single simulated data set fit. The standard deviation of the rate is $\Delta R = 3 \cdot 10^{-3}s^{-1}$. This implies also that a fitted rate of such magnitude for the experimental data is statistically consistent with zero; A real rate that is present but smaller than this ΔR is hidden in the statistical fluctuations and cannot be extracted from a fit.

Finally, it is mentioned that for the statistical analysis in the quantum jump technique the least-squares method is inappropriate. The bins at longer times have only few events the distribution of which deviates strongly from a Gaussian because of the binomial distribution. These points are weighted incorrectly when fitted with the least squares method. A relevant method in such a case is the more general maximum-likelihood-estimation method which is independent of the distribution, see e.g. [108].

B Statistical Methods for Data Analysis

C Systematic Errors

Systematic errors are inherent to most physical measurement processes. Often they can be avoided by a careful experimental procedure or detected by a deviation of the data from the expected model. But if the deviation is within the statistical noise, data simulations are an elegant way to estimate limits for systematic errors. The relevant question here is how do e.g. detection errors translate into a systematic error of the measured decay probability p and what is the effect on the resulting lifetime?

C.1 Detection Error

The state detection is based on the discrimination of two fluorescence levels. If the ion is in the D-state: no fluorescence = counts C_D (=background counts). If the ion is in the S-state: fluorescence = counts C_S . The state is determined by comparing the counts C

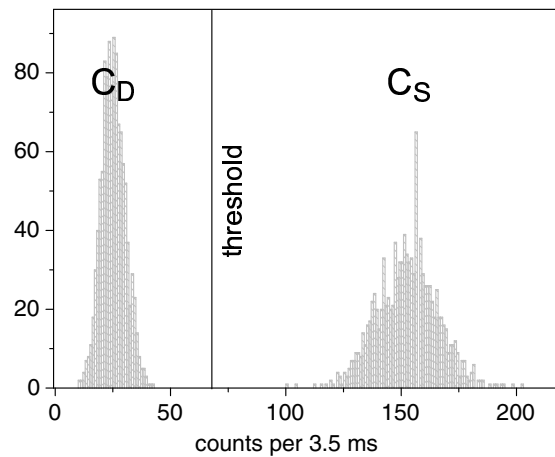


Figure C.1: Histogram of fluorescence counts of a single ion in the detection interval of 3.5 ms. The Poissonian distribution of counts is visible. The excitation probability is approximately 0.5. The threshold for discrimination is indicated by the vertical line. The signal-to-background ratio is about 6.5 at an average countrate of 45 kHz when the ion is fluorescing.

C Systematic Errors

to a threshold Θ ($C_D < \Theta < C_S$). An example of the distribution of fluorescence counts in the detection interval of 3.5 ms is shown in a histogram in figure C.1. Detection errors may occur due to the Poissonian distribution of counts (width= \sqrt{C}) and the possibility of spontaneous emission during the detection. In the following, these two classes of errors will be referred to as type 1 and type 2, respectively.

Type 1 errors are of pure statistical nature. They can happen both ways: measuring state S while the ion was actually in state D and vice versa¹. For a proper threshold these possibilities are equal in magnitude (ε_1). The probability of measuring D instead S can be expressed as

$$\varepsilon_1 = \text{prob}(C_S < \Theta) = \frac{1}{2} (1 - \text{prob}(\bar{C}_S - \Theta < C_S < \bar{C}_S + \Theta)). \quad (\text{C.1})$$

The second probability on the right hand side is calculated by integrating over the probability density function of C_S which can well be approximated by a Gaussian:

$$\text{prob}(\bar{C}_S - \Theta < C_S < \bar{C}_S + \Theta) = \frac{1}{\sqrt{2\pi}} \int_{\bar{C}_S - \Theta}^{\bar{C}_S + \Theta} e^{-\left(\frac{C_S - \bar{C}_S}{\sqrt{2\bar{C}_S}}\right)^2} dC \quad (\text{C.2})$$

This value of the integral in C.2 can be found in tables e.g. in the appendix of ref. [108]. For $\frac{\bar{C}_S - \Theta}{\sqrt{\bar{C}_S}} \approx 7$ (the threshold is seven standard deviations away from the mean) the type 1 error is negligibly small: $\varepsilon_1 < 10^{-6}$.

Type 2 errors occur when the ion decays during the interval T of the detection. If such an event happens at time t after the start the mean detected counts C'_D are

$$C'_D(t) = \bar{C}_D \frac{t}{T} + \bar{C}_S \left(1 - \frac{t}{T}\right). \quad (\text{C.3})$$

At time $t = t_\varepsilon = T \left(\frac{C_S - \Theta}{\bar{C}_S - \bar{C}_D}\right)$ the number of counts are equal to the threshold, $C'_D(t_\varepsilon) = \Theta$. Hence the error is the probability that the ion decays in the interval $(0, t_\varepsilon)$ [118]:

$$\varepsilon_2 = \frac{t_\varepsilon}{\tau} = \frac{T}{\tau} \left(\frac{\bar{C}_S - \Theta}{\bar{C}_S - \bar{C}_D}\right) \quad (\text{C.4})$$

With the experimental values this produces an error of $\varepsilon_2 = 2 \cdot 10^{-3}$. Clearly, the error also depends on the population. For example, if the ion is in the S state with 98% probability then this error is negligible. Hence it only affects the measured initial decay. The systematic error in the measured excitation probability p_{meas} can be written as:

$$p_{meas} = (1 - \varepsilon_2)p_{actual} \quad (\text{C.5})$$

¹Note that this is referred to as type 1 and type 2 error, respectively in reference [118].

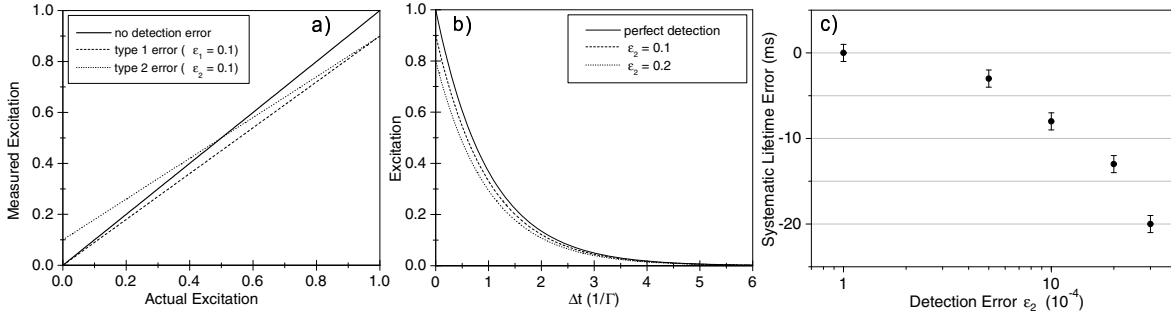


Figure C.2: **a)** Two models for the detection error: Type 1 errors are due to Poissonian noise in the detection counts. This error is less than 10^{-6} and can safely be ignored here. Type 2 errors are due to spontaneous decay during the detection period. It is of the order of 10^{-3} and the dominating error. Exaggerated 10% errors of both types are shown to illustrate the effect on the measured excitation as a function of the actual excitation. **b)** Effect of type 2 detection error in the measured excitation as a function of waiting time. **c)** The systematic error in the lifetime due to detection error: Data is simulated including a detection error and fitted with a pure exponential curve $(1 - p) = e^{-\Delta t/\tau}$. The systematic error is the deviation of the fitted lifetime from the real lifetime used for the simulations.

This error model is illustrated in fig. C.2 with an exaggerated error. The systematic error on the resulting lifetime is then found by simulating data as in section B using the error model in equation C.5. The data is then fitted with a normal exponential function $(1 - p) = e^{-\Delta t/\tau}$. The results are shown in fig. C.2c as a function of the detection error ε_2 . For $\varepsilon_2 = 1 \cdot 10^{-3}$ a systematic error of the lifetime result is determined to be $\Delta\tau = +8\text{ms}$.

A detailed mathematical analysis of the detection error can also be found in the PhD thesis of C. Roos [118].

C.2 Rate Error

A repumping rate leads to a different exponential decay. This can be modeled by a simple rate equation including the additional rate R with the opposite sign. The differential equation for the excited state population p_D is then written as:

$$\dot{p}_D = -\Gamma p_D + R(1 - p_D) \quad (\text{C.6})$$

C Systematic Errors

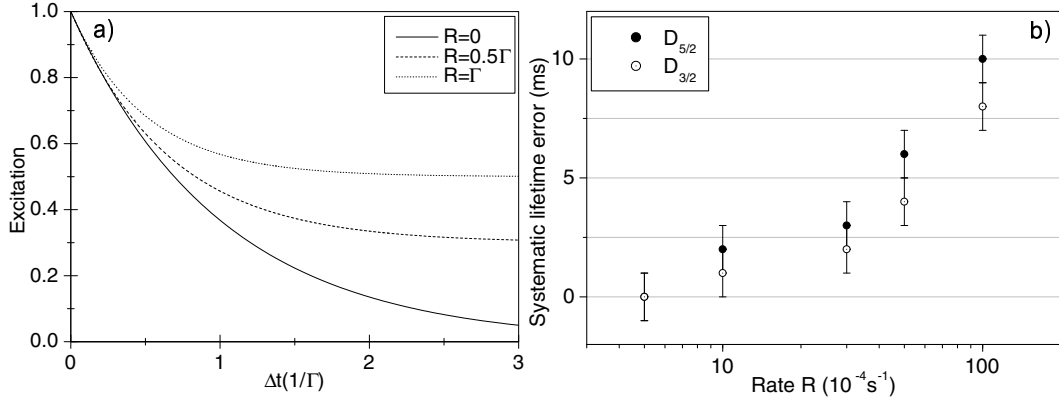


Figure C.3: The effect of a repumping rate R : **a)** Solutions of the rate equation, $p_D = B + Ae^{-\Gamma't}$, a modified exponential model. **b)** Systematic error of the fitted lifetime to simulated data.

and by substituting the ansatz $p_D = B + Ae^{-\Gamma't}$ it follows for the parameters A , B , and Γ' :

$$B = \frac{R}{\Gamma'}, \quad A = 1 - \frac{R}{\Gamma'}, \quad \Gamma' = \Gamma + R \quad (\text{C.7})$$

The solution is graphically depicted in fig. C.3a. In the initial decay behaviour the rate is not significant but for longer times the decay probability approaches an offset, the equilibrium point of decay and repumping. This offset leads to systematic error towards longer lifetimes which again is investigated by the use of simulated data. For different rates model data are simulated and fitted with the normal exponential model. The dependence is shown in fig.C.3b. When the experimental data is fitted with the rate model $p_D = B + Ae^{-\Gamma't}$ resulting in $R = 6 \cdot 10^{-3} \text{ s}^{-1}$ and $\tau = 1172 \text{ ms}$. Using the normal exponential fit function $p_D = e^{-\Delta t/\tau}$ (c.f section 5.3) $\tau = 1176 \text{ ms}$ was found. The fits to the simulated data for a rate of $R = 5 \cdot 10^{-3} \text{ s}^{-1}$ yield lifetimes for both $D_{3/2}$ and $D_{5/2}$ that are systematically larger by $\Delta\tau = +4 \text{ ms}$ (fig. C.3c), the same discrepancy as the experimental fits. This is an impressive indication that the simulations produce reliable results.

It should be noted that in this case the systematic error is hidden in the natural statistical error of the rate and cannot be resolved directly, c.f. figure B.2b.

C.3 π Pulse Error

The decay of the $D_{3/2}$ level p_{dec} is measured by transferring the decayed population to the $D_{5/2}$ level via a π pulse and determining its excitation probability p_D . Due to heating of the ion the transfer efficiency η_π decreases with waiting time and leads to a

C.3 π Pulse Error

systematic error in the measured excitation probability p_D , see fig. C.4b.

$$p_{dec} = 1 - \frac{p_D}{\eta_\pi}, \quad \eta_\pi = 1 - a \cdot \Delta t \quad (\text{C.8})$$

The decrease of the π pulse transfer efficiency was measured independently in the experiment as $a = 4(2) \cdot 10^{-3} \text{s}^{-1}$ (fig.C.4a). This value for a implies a systematic error in the $D_{3/2}$ lifetime of $\Delta\tau = -7\text{ms}$. Simulating data according to C.8 and fitting the normal exponential model yields $\tau = 1186\text{ms}$ (fig. C.4c).

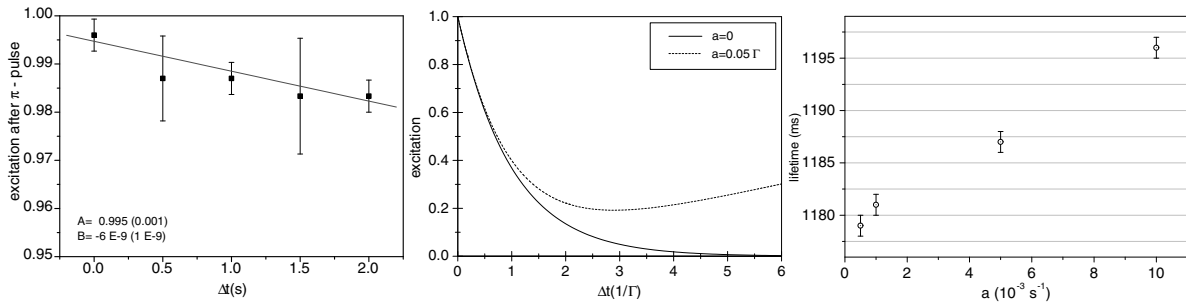


Figure C.4: The effect of decreasing π pulse efficiency. **a)** The efficiency decreases linearly with slope $a = 4(2) \cdot 10^{-3} \text{s}^{-1}$: $\eta_\pi = 1 - a \cdot \Delta t$. **b)** For longer waiting times Δt the measured excitation is systematically higher than the actual excitation (exaggerated illustration). **c)** Systematic error on the $D_{3/2}$ lifetime as a function of slope a .

C Systematic Errors

D Lifetime Measurement Strategy at a Single Delay Time

In chapter 6 the lifetime is determined by measuring the decay for a single waiting time Δt only. This is sufficient since the decay follows the exponential law, for which:

$$\tau = \frac{-\Delta t}{\ln(1-p)}. \quad (\text{D.1})$$

The remaining problem is to find the optimal waiting time such that the relative error in the resulting lifetime decreases fastest with measurement time.

Consider first the error of the decay probability Δp which is results from quantum projection noise:

$$\Delta p = \sqrt{p(1-p)/N} \quad (\text{D.2})$$

where N is the total number of experiments. This transforms into a relative lifetime error

$$\frac{\Delta \tau}{\tau} = -\frac{\sqrt{p(1-p)}}{\ln(1-p)(1-p)\sqrt{N}} \quad (\text{D.3})$$

by error propagation $\Delta \tau = \frac{d\tau}{dp} \Delta p$. The total measurement time T is $T = N(\Delta t + \varepsilon)$ where ε is the time overhead in the pulse sequence due to state preparation and detection, here $\varepsilon = 5.5$ ms, recalling fig. 5.1. The relative error in the lifetime after a fixed measuring time T can then be written as a function of p only when Δt is replaced by $-\tau \ln(1-p)$:

$$\frac{\Delta \tau}{\tau} = \frac{\sqrt{p(1-p)}}{\ln(1-p)(1-p)} \sqrt{\frac{-\tau[\ln(1-p) + \varepsilon]}{T}} \quad (\text{D.4})$$

A plot of the relative error $\Delta \tau/\tau$ against p for a lifetime of $\tau = 1165$ ms and a measurement time of $T = 10$ min is shown in fig. D.1. A relatively flat minimum is identified at 9% decay which corresponds to a delay time of 110 ms. For the lifetime measurements in chapter 6 a fixed delay of 50 ms was chosen as a compromise between fast data aquisition and minimum heating of the ion during the delay. Also, for short delays the timing of the mechanical shutter (for the 854 nm beam) becomes more critical.

D Lifetime Measurement Strategy at a Single Delay Time

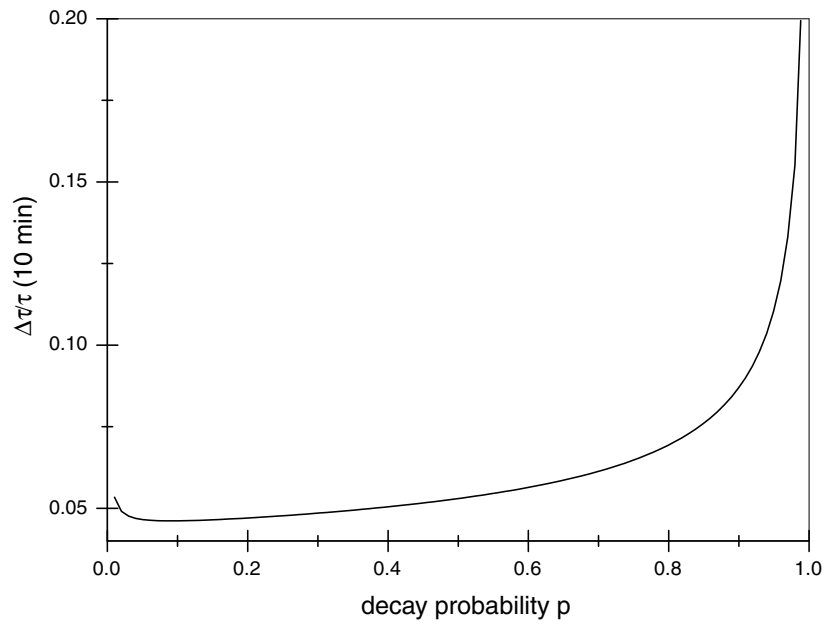


Figure D.1: Relative lifetime error after a measurement time of 10 min as a function of the decay probability. The relatively flat minimum is at 9% decay which corresponds to a waiting time $\Delta t = 110$ ms.

E Spontaneous emission lifetime of a single trapped Ca^+ ion in a high finesse cavity

Published in Phys. Rev. Lett. **92**, 203002 (2004)

Spontaneous Emission Lifetime of a Single Trapped Ca^+ Ion in a High Finesse CavityA. Kreuter, C. Becher,* G. P.T. Lancaster, A. B. Mundt, C. Russo, H. Häffner, C. Roos, J. Eschner,[†]
F. Schmidt-Kaler, and R. Blatt*Institut für Experimentalphysik, Universität Innsbruck, Technikerstraße 25, A-6020 Innsbruck, Austria*
(Received 22 December 2003; published 19 May 2004)

We investigate the spontaneous emission lifetime of a single trapped $^{40}\text{Ca}^+$ ion placed at different positions in the vacuum standing wave inside a high finesse cavity which is stabilized to the atomic transition. The lifetime is measured by quantum state detection after π -pulse excitation. The result for the natural lifetime of the $D_{5/2}$ metastable state of 1161(22) ms agrees, within 1 standard deviation, with the most precise published value. We observe a reduction of the spontaneous emission lifetime of $\approx 15\%$ in the node of the vacuum field.

DOI: 10.1103/PhysRevLett.92.203002

PACS numbers: 32.70.Cs, 03.67.Lx, 42.50.Pq

The rapid and promising development in the field of quantum information processing in recent years is based on the ability to control and manipulate single quantum systems. Among these, trapped ions have proven to constitute a model system for storing and processing quantum information. The transport of this information within distributed quantum networks [1] requires an interface between trapped ions and photons operating as moving quantum bits. Such an interface could be based on the deterministic coupling of a single atom or ion to a high finesse optical cavity [2,3], which requires the ability to precisely and stationary place the atom at a fixed position within the cavity field. So far, such deterministic coupling has been demonstrated only for intense light fields [2,3]. However, the transport of quantum information implies coupling of an atomic quantum bit to the cavity vacuum field, which in turn modifies the spontaneous emission properties of the atom. To demonstrate the feasibility of this approach, we investigate the stationary interaction of a single trapped Ca^+ ion with the vacuum field inside an optical cavity by measuring the modification of the spontaneous emission lifetime of the metastable $D_{5/2}$ level (≈ 1 s) at various positions within the cavity. Because of the good localization of the ion we are able to map the standing-wave vacuum field.

The enhancement or inhibition of spontaneous emission due to the modification of the vacuum field by a resonator has long been predicted by Purcell [4] and Kleppner [5]. There have been experimental demonstrations with *ensembles of emitters* coupled to resonant structures [6,7] and with few or *single emitters* coupled to cavities: a single electron trapped in a microwave cavity [8], Rydberg atoms traversing microwave cavities [9,10], dilute atom beams traversing optical resonators [11,12], a single trapped ion interacting with a single mirror [13], and a single semiconductor quantum dot coupled to a microcavity [14,15]. Among these, only the experiments with ions and quantum dots have been carried out with one and the same single quantum emitter. In addition, besides the work involving a trapped ion [13],

these experiments lack either the stationary coupling or the deterministic control of the emitter position with respect to the resonator mode. In our experiment, the motional wave packet of a laser-cooled trapped ion is confined to a region much smaller than the optical wavelength λ (to approximately $\lambda/50$), and its position within a cavity standing-wave (SW) field is controlled with a precision of up to 7 nm [3].

The lifetimes of the metastable D levels of $^{40}\text{Ca}^+$ have been subject to several investigations, both theoretical and experimental, because of their high relevance to frequency standards [16] and atomic structure theory. All previous lifetime measurements of the $D_{5/2}$ level of single $^{40}\text{Ca}^+$ ions employed the quantum jump technique (see [17], and references therein). This technique is based on monitoring the fluorescence on the $S_{1/2}$ - $P_{1/2}$ dipole transition [see Fig. 1(a)], while at random times the ion is shelved to the metastable state where the fluorescence falls to the background level. Statistical analysis of these dark times yields the lifetime τ . The most precise measurement using this technique resulted in $\tau = 1168(7)$ ms [17].

Here, we introduce a new measurement technique based on coherent excitation and quantum state detection. The quantum jump method is not appropriate in our experiment as the 397 nm light that is used to monitor the fluorescence would broaden the $S_{1/2}$ ground state by dipole coupling to far beyond the linewidth of the cavity, and hence the vacuum effect would become negligible. Instead, we use an improved version of a technique that was used to measure the $D_{3/2}$ metastable level lifetime of single Ba^+ ions [18]. The method is to first excite the ion deterministically with a π pulse and then measure the remaining excitation after a fixed waiting period, during which all lasers are shut off. The main advantage of this “state detection” method is that no residual light is present during the measurement which could affect the free decay of the atom. Thus we are able to measure the free-space lifetime with high precision. For the measurement of the cavity-modified lifetime, however, we cannot

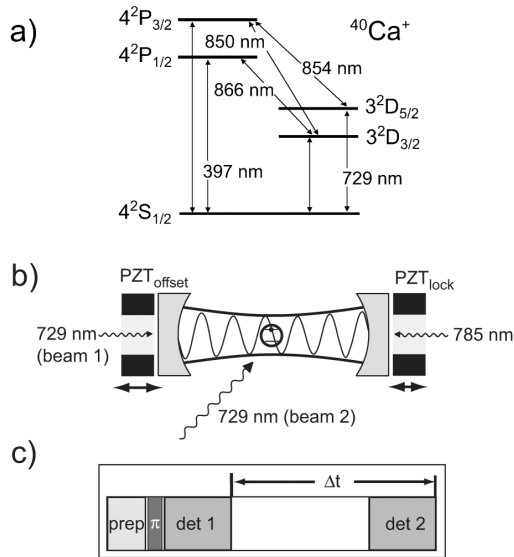


FIG. 1. (a) Ca^+ -level scheme with relevant transitions. (b) Sketch of the experimental setup with a single ion in the standing wave of a two-mirror near-confocal cavity at 729 nm. Laser beam 1 is used to measure the ion's position in the SW; beam 2 prepares the ion in the D state by a π pulse. (c) Schematic pulse sequence of one experimental cycle for the lifetime measurement (see text for details).

avoid residual light. The far off-resonant transfer laser light that is needed to keep the cavity frequency locked causes additional deshelling of the $D_{5/2}$ state by admixing a small fraction of the fast-decaying $P_{3/2}$ level. This effect has been carefully measured and is described below.

The experimental setup is shown schematically in Fig. 1 and is described in detail elsewhere [3,19]. The general experimental procedure starts with loading a single $^{40}\text{Ca}^+$ ion into a spherical Paul trap with radial and axial secular frequencies $(\omega_{r1}, \omega_{r2}, \omega_{ax}) = 2\pi(1.9, 2.6, 4.5)$ MHz. The trap is located inside a near-confocal resonator with a finesse of $\mathcal{F} \approx 35000$ at 729 nm and a waist of $54 \mu\text{m}$. The mirrors are both mounted on piezoelectric translators (PZT) to allow for independent movement. The cavity is frequency stabilized using the Pound-Drever-Hall technique to a transfer laser (extended cavity diode laser at ≈ 785 nm) [19]. The transfer laser is frequency stabilized to the same ultrastable reference cavity as the Ti:Sapphire laser used to drive the 729 nm transitions. By an appropriate frequency tuning of the transfer laser with an acousto-optical modulator (AOM), the cavity is made resonant for both the transfer laser and the 729 nm laser [beam 1 in Fig. 1(b)]. This ensures that the cavity is resonant with the quadrupole transition without using resonant light.

The lifetime measurements described here consist of a repetition of a laser pulse sequence applied to the ion. The

sequence generally is composed of three steps [see Fig. 1(c)]: (i) state preparation and Doppler cooling consisting of 2 ms of Doppler cooling (397 and 866 nm light), repumping from the $D_{5/2}$ level (854 nm light), and optical pumping into the $S_{1/2}(m = -1/2)$ Zeeman sublevel (397 nm σ^+ polarized light), (ii) coherent excitation at 729 nm [beam 2 in Fig. 1(b)], with pulse length and intensity chosen to obtain near unity excitation (π pulse) to the $D_{5/2}(m = -5/2)$ Zeeman level, and (iii) state detection for 3.5 ms by recording the fluorescence on the $S_{1/2}-P_{1/2}$ transition with a photomultiplier to discriminate between the states S and D . The state is measured before and after a fixed waiting period Δt between 10 and 500 ms to determine whether a decay of the excited state has occurred. This three-step cycle [steps (i)–(iii)] is repeated typically several thousand times to yield the decay probability p . For the calculation of the lifetime τ we use an exponential fit function $1 - p = A \exp\{-\Delta t/\tau\}$. For Δt we use the time interval between the ends of the two detection periods. Poissonian noise of the count rate or decay of the atom during the detection period can lead to a small error in the quantum state detection [20]. We model this error as a deviation of the fit parameter A from its ideal value of one.

As a first step, the natural free-space lifetime of the $D_{5/2}$ level is determined without the cavity influence to assure the accuracy of our measuring scheme and to exclude possible inconsistencies and systematic errors. The results for various waiting periods between 10 and 500 ms, based on several 10^5 decay measurements each, are displayed in Fig. 2. The exponential fit function described above yields a lifetime of 1161(22) ms, in good agreement with earlier results [17] (the number in parentheses being the 1σ confidence level). The fit also verifies that the decay probability satisfies an exponential law. For the data in Fig. 2 we find $A = 0.99939(50)$, indicating that the error in quantum state detection for the given length of detection periods is only $6(5) \times 10^{-4}$. We stress that this lifetime measurement is an independent check of earlier results since we used a different measurement technique.

We note that the lifetime measurement was found to be extremely sensitive to any background radiation at the repump wavelength of 854 nm, which can either originate from residual light of the 854 nm diode laser itself, background fluorescence of the 866 nm diode laser, or residual light from the laboratory environment. Great care was taken to avoid these sources of systematic error. The 854 nm light is switched by a mechanical shutter in the beam path (40 dB attenuation by an AOM in double pass configuration was found not to be sufficient) and the 866 nm beam is shut off by an AOM in single pass (attenuation >30 dB) during the waiting time. Other possible effects that result in a lifetime reduction include collisional effects, such as quenching and J -mixing [21,22]. Collisional quenching effects are neglected on

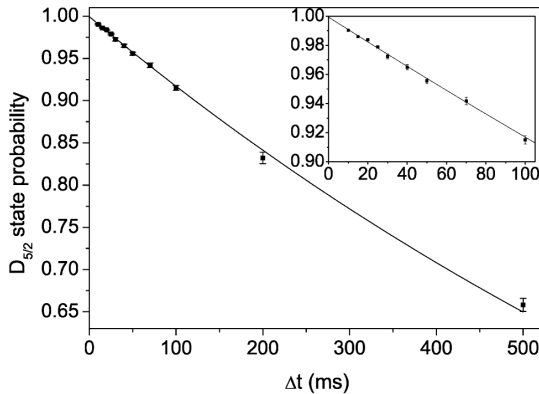


FIG. 2. Decay of the $D_{5/2}$ level as a function of waiting time. An exponential fit (solid line) yields the natural lifetime.

grounds of low pressures ($< 3 \times 10^{-10}$ mbar). J -mixing is neglected as measurements using coherent excitation and deexcitation after 100 ms did not indicate any decoherence beyond the expected spontaneous decay.

As our state detection technique yields consistent lifetime results, we can now use it to investigate the influence of the cavity vacuum field on the atomic lifetime. For lifetime measurements with the frequency-stabilized cavity, the largest systematic error is due to the presence of transfer laser light at 785 nm. To investigate its influence, the $D_{5/2}$ decay rate was measured as a function of the ac Stark shift of the $D_{5/2}$ level induced by the transfer laser (Fig. 3). We determined the ac Stark shift by excitation spectroscopy on the $S_{1/2}$ - $D_{5/2}$ transition and use it as a measure for the intracavity power of the transfer laser since the latter is difficult to determine. The linear fit in Fig. 3 yields the additional deshelling rate of $0.0027 \text{ s}^{-1}/\text{kHz}$ on the $D_{5/2}$ - $P_{3/2}$ transition due to the transfer laser light.

To measure the spatial dependence of the enhanced spontaneous emission, we frequency stabilize the cavity as described above, using the minimum possible transfer laser power (approximately 20 mW intracavity power) to keep the frequency lock stable. The SW pattern is measured by exciting the ion with short pulses at 729 nm (pulse length approximately equal to the $\pi/2$ time at the node) through the locked cavity [beam 1 in Fig. 1(b)] and varying the voltage of the offset PZT, resulting in the phase of the SW being shifted with respect to the spatially fixed ion (see inset of Fig. 4). To place the ion at a specific position in the SW, we then apply the corresponding offset voltage. This procedure is done before and after each lifetime measurement (a few 1000 sequences) to account for thermal drifts. Several measurements over around 15 h showed that the drift is linear over several hours and corresponds to a displacement by $\lambda/4$ in 3.9 h. Each measurement was limited to 19 min (2×10^4 single experiments), yielding a position uncertainty of $\approx \lambda/50$.

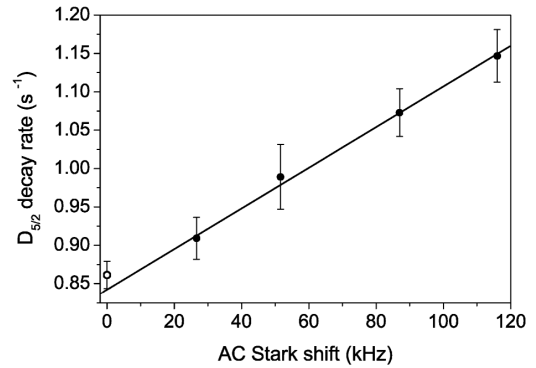


FIG. 3. Total decay rate from the $D_{5/2}$ state versus ac Stark shift on the $S_{1/2}$ - $D_{5/2}$ transition induced by the transfer laser. The open dot represents the decay rate in free space measured without transfer laser.

The measurements of the cavity-modified lifetime were performed with a fixed waiting time $\Delta t = 50$ ms. The raw data from many experimental runs are combined to yield the results of the lifetime measurement at five different points in the vacuum SW, shown in Fig. 4. The indicated lifetime errors are the 1σ statistical errors, while the errors in the phase result from the deviation of the SW phase in the individual measurements. Note that the drift during the time of the measurement (15 nm in 19 min) is not a systematic error but corresponds to an averaging over the sinusoidal variation and a loss of contrast. In addition, the spatial extension of the ion's wave packet (on the order of 20 nm, taking into account a heating rate of 0.1 ms^{-1} during 50 ms) also leads to a loss of contrast [23]. The combined effect yields a visibility of the SW of $V \approx 90\%$. To exclude any residual

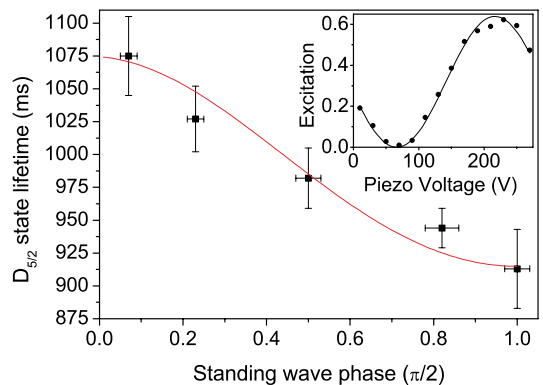


FIG. 4 (color online). $D_{5/2}$ state lifetime measured at various positions in the cavity vacuum standing-wave field. The solid line shows a simulation of the Purcell effect, assuming $\tau = 1075$ ms, a Purcell factor $F = 1.175$, and a visibility of $V = 0.9$. The inset shows a measurement of an intense cavity standing wave by coherent excitation (c.f. [3,19]).

systematic errors (lifetime reduction due to effects other than the cavity field), the lifetime is also measured off resonance with the cavity shifted more than ten linewidths away from resonance by changing the frequency of the transfer laser by 2 MHz. This off-resonance lifetime was 1069(37) ms. The ac Stark shift for these measurements was maximally 16 kHz, which results in an additional deshelling rate of 0.04 s^{-1} . This appears as a $<5\%$ lifetime reduction, which varies sinusoidally with the transfer laser SW in the cavity. This transfer laser SW has, in general, a different phase than the vacuum SW, which was not determined independently for the cavity lifetime measurement. Thus each data point in Fig. 4 has an additional error of $\pm 5\%$ due to the additional deshelling induced by the transfer laser. It is important to point out that the observed lifetime reduction is a genuine cavity QED effect, consistent with the measured phase of the vacuum SW, and can not be explained only by the deshelling effect of the transfer laser.

The observed maximum lifetime reduction in the node of the vacuum field is $15 \pm 5\%$. With our experimentally determined parameters, i.e., ion-field coupling constant $g = 2\pi \times 120 \text{ Hz}$, cavity decay rate $\kappa = 2\pi \times 102 \text{ kHz}$, and spontaneous emission rate $\gamma = 1/\tau = 2\pi \times 0.137 \text{ Hz}$, we calculate the cooperativity parameter [24] $C_0 = g^2/2\kappa\gamma = 0.52$ and a Purcell factor [24] $F = 2C_0 + 1 = 2.04$, which should yield a 50% lifetime reduction [3]. However, there are several experimental imperfections that contribute to the reduction of the expected effect. First, disturbance (acoustical, etc.) of the cavity lock leads to an inhomogeneous broadening of the cavity linewidth. The resulting effective finesse found from scanning the 729 nm laser slowly over the locked cavity resonance is $\mathcal{F}_{\text{eff}} \approx 22000$, which reduces the cooperativity to $0.62C_0$. Second, the coupling is reduced by a suboptimal lateral position of the ion in the waist of the cavity mode. This position has been optimized by moving the trap mount with micrometer screws and recording Rabi oscillation frequencies driven through the cavity field at every position. This positioning achieves an estimated precision of $20 \mu\text{m}$, resulting in a reduced cooperativity of $0.57C_0$. Taking into account the SW visibility $V = 90\%$, as discussed above, the total effective cooperativity is $C_{\text{eff}} = 0.62 \times 0.57 \times 0.9 \times C_0 = 0.165$, corresponding to an expected 25% lifetime reduction. In the antinode of the cavity SW (SW phase = 0 in Fig. 4), the lifetime τ_a should be approximately equal to the free-space lifetime ($\tau_a = 0.98\tau = 1138 \text{ ms}$). However, in our experiment we measure a maximum lifetime of $\tau_a = 1075(30) \text{ ms}$ in the cavity SW. Therefore we assume the following worst-case scenario: the transfer laser deshelling rate of 0.04 s^{-1} leads to a reduction of the maximum observable lifetime in the SW antinode by $\approx 5\%$ (expected $\tau_a = 1089 \text{ ms}$) and leaves

the minimum lifetime in the SW node unchanged, yielding an expected 21% lifetime reduction.

In summary, we have demonstrated the deterministic coupling of a single ion to the vacuum field inside a high finesse cavity over an extended time. The spatial variation of the spontaneous emission rate has been investigated by measuring the $D_{5/2}$ state lifetime with a new method based on deterministic excitation and quantum state detection. As the position in the standing wave and the lifetime are measured independently, our experiment is a genuine demonstration of single-atom cavity QED.

This work is supported by the Austrian ‘‘Fonds zur F6rderung der wissenschaftlichen Forschung’’ (SFB15), by the European Commission: IHP network ‘‘QUEST’’ (HPRN-CT-2000-00121), IST/FET Program ‘‘QUBITS’’ (IST-1999-13021), and the Marie-Curie-Program (H. H.), and by the ‘‘Institut f6ur Quanteninformation GmbH.’’ C. Russo acknowledges support by Funda7ao para a Ci4ncia e a Tecnologia, Portugal, Grant No. SFRH/BD/6208/2001.

*Electronic address: Christoph.Becher@uibk.ac.at

[†]Present address: Institut for Photonic Sciences (ICFO), C/ Jordi Girona, 29, 08034, Barcelona, Spain.

- [1] J. I. Cirac *et al.*, Phys. Rev. Lett. **78**, 3221 (1997).
- [2] G. R. Guth6rlein *et al.*, Nature (London) **414**, 49 (2001).
- [3] A. B. Mundt *et al.*, Phys. Rev. Lett. **89**, 103001 (2002).
- [4] E. M. Purcell, Phys. Rev. **69**, 681 (1946).
- [5] D. Kleppner, Phys. Rev. Lett. **47**, 233 (1981).
- [6] K. H. Drexhage, in *Progress in Optics*, edited by E. Wolf (North-Holland, Amsterdam, 1974), Vol. 12, p. 163.
- [7] F. DeMartini *et al.*, Phys. Rev. Lett. **59**, 2955 (1987).
- [8] G. Gabrielse and H. Dehmelt, Phys. Rev. Lett. **55**, 67 (1985).
- [9] P. Goy *et al.*, Phys. Rev. Lett. **50**, 1903 (1983).
- [10] R. G. Hulet, E. S. Hilfer, and D. Kleppner, Phys. Rev. Lett. **55**, 2137 (1985).
- [11] W. Jhe *et al.*, Phys. Rev. Lett. **58**, 666 (1987).
- [12] D. J. Heinzen *et al.*, Phys. Rev. Lett. **58**, 1320 (1987).
- [13] J. Eschner *et al.*, Nature (London) **413**, 495 (2001).
- [14] A. Kiraz *et al.*, Appl. Phys. Lett. **78**, 3932 (2001).
- [15] G. S. Solomon, M. Pelton, and Y. Yamamoto, Phys. Rev. Lett. **86**, 3903 (2001).
- [16] R. J. Rafac *et al.*, Phys. Rev. Lett. **85**, 2462 (2000).
- [17] P. A. Barton *et al.*, Phys. Rev. A **62**, 032503 (2000).
- [18] N. Yu, W. Nagourney, and H. Dehmelt, Phys. Rev. Lett. **78**, 4898 (1997).
- [19] A. B. Mundt *et al.*, Appl. Phys. B **76**, 117 (2003).
- [20] C. Roos, Ph.D. thesis, University of Innsbruck, 2000.
- [21] M. Knoop, M. Vedel, and F. Vedel, Phys. Rev. A **52**, 3763 (1995); **58**, 264 (1998).
- [22] P. Staanum *et al.*, Phys. Rev. A **69**, 032503 (2004).
- [23] J. Eschner, Eur. Phys. J. D **22**, 341 (2003).
- [24] Q. A. Turchette, R. J. Thompson, and H. J. Kimble, Appl. Phys. B **60**, 1 (1995).

E Spontaneous emission lifetime of a single trapped Ca^+ ion in a high finesse cavity

F New experimental and theoretical approach to the 3d 2D -level lifetimes of $^{40}\text{Ca}^+$

Submitted to Phys. Rev. A, online version on arXiv-server: physics/0409038

New experimental and theoretical approach to the $3d\ ^2D$ -level lifetimes of $^{40}\text{Ca}^+$

A. Kreuter, C. Becher,* G.P.T. Lancaster, A.B. Mundt, C. Russo,
H. Häffner, C. Roos, W. Hänsel, F. Schmidt-Kaler, and R. Blatt†
Institut für Experimentalphysik, Universität Innsbruck, Technikerstraße 25, A-6020 Innsbruck, Austria

M.S. Safronova
Department of Physics and Astronomy, University of Delaware, Newark, Delaware 19716, USA
(Dated: September 7, 2004)

We report measurements of the lifetimes of the $3d\ ^2D_{5/2}$ and $3d\ ^2D_{3/2}$ metastable states of a single laser-cooled $^{40}\text{Ca}^+$ ion in a linear Paul trap. We introduce a new measurement technique based on high-efficiency quantum state detection after coherent excitation to the $D_{5/2}$ state or incoherent shelving in the $D_{3/2}$ state, and subsequent free, unperturbed spontaneous decay. The result for the natural lifetime of the $D_{5/2}$ state of 1168(9) ms agrees excellently with the most precise published value. The lifetime of the $D_{3/2}$ state is measured with a single ion for the first time and yields 1176(11) ms which improves the statistical uncertainty of previous results by a factor of four. We compare these experimental lifetimes to high-precision *ab initio* all order calculations and find a very good agreement. These calculations represent an excellent test of high-precision atomic theory and will serve as a benchmark for the study of parity nonconservation in Ba^+ which has similar atomic structure.

I. INTRODUCTION

The lifetime of the metastable D-levels in Ca^+ is of high relevance in various experimental fields such as optical frequency standards, quantum information and astronomy. Trapped ion optical frequency standards [1] and optical clocks [2] are based on narrow absorption lines in single laser-cooled ions. With transition linewidths in the 1 Hz range [3], Q-values (frequency of the absorption divided by its spectral width) of $\approx 10^{15}$ can be achieved. As the lifetimes of the D-levels in Ca^+ are on the order of 1 s, yielding sub-Hz natural linewidths of the D-S quadrupole transitions, Ca^+ has long been proposed as a promising candidate for a trapped ion frequency standard [4]. Such long lifetimes together with the ability to completely control the motional and electronic degrees of freedom of a trapped ion [5] make it ideally suited for storing and processing quantum information [6]. In Ca^+ a quantum bit (qubit) of information can be encoded within the coherent superposition of the $S_{1/2}$ ground state and the metastable $D_{5/2}$ excited state [7] with very long coherence times [8, 9]. In astronomy, absorption lines of Ca^+ ions are used to explore the kinematics and structure of interstellar gas clouds [10, 11] and the D-level lifetimes are required for interpretation of the spectroscopic data. On the other hand, in theoretical atomic physics Ca^+ is an excellent benchmark problem for atomic structure calculations owing to large higher-order correlation corrections and its similarity to Ba^+ . The size and distribution of the correlation correc-

tions make it ideal for the study of the accuracy of various implementations of the all-order method. The properties of Ba^+ are of interest due to studies of parity nonconservation in heavy atoms and corresponding atomic-physics tests of the Standard model of the electroweak interaction [12].

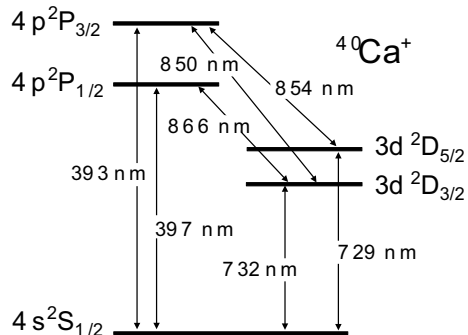


FIG. 1: Ca^+ -level scheme with relevant transitions.

Experimental investigations of long atomic lifetimes have profited enormously from the development of ion trap technology and laser spectroscopy. Early experiments on the measurement of the D-level lifetimes in $^{40}\text{Ca}^+$ [13–17] used large clouds of ions and the lifetime was determined by recovery of fluorescence on the UV-transitions ($S_{1/2} - P_{1/2}$ or $S_{1/2} - P_{3/2}$, see Fig. 1) after electron shelving in the D-states or by observing UV fluorescence after driving transitions from the D-states to the P-states. Shelving in this context means that the electron for a certain time remains in a metastable atomic level which is not part of a driven fluorescence cycle. These lifetime measurements were limited by deshelling induced by collisions with other ions or the buffer gas

*Electronic address: Christoph.Becher@uibk.ac.at
†also with: Institut für Quantenoptik und Quanteninformation, Österreichische Akademie der Wissenschaften, Technikerstraße 25, A-6020 Innsbruck, Austria

used for cooling. Similar results using the same techniques have been obtained in an ion storage ring [18].

Much more accurate results can be obtained by performing lifetime measurements with single trapped ions [19–23] or strings of few trapped ions [24] and employing the quantum jump technique. This technique is based on monitoring the fluorescence on the $S_{1/2} - P_{1/2}$ dipole transition while at random times the ion is shelved to the metastable $D_{5/2}$ -state where the fluorescence falls to the background level. For observing fluorescence both the $S_{1/2} - P_{1/2}$ (397 nm) and the $D_{3/2} - P_{1/2}$ (866 nm) transition have to be driven to prevent the ion from residing in the metastable $D_{3/2}$ -state. Shelving to the $D_{5/2}$ -state is initiated by applying laser light at 850 nm ($D_{3/2} - P_{3/2}$) [19] or at 729 nm ($S_{1/2} - D_{5/2}$) [23]. Statistical analysis of the fluorescence dark times yields the lifetime τ . The most precise measurement using this technique was carried out by Barton et al. [22] who found the result of $\tau=1168(7)$ ms.

Here, we introduce a measurement technique [25] based on deterministic coherent excitation to the $D_{5/2}$ state or incoherent shelving in the $D_{3/2}$ state, followed by a waiting period with free spontaneous decay and finally a measurement of the remaining excitation by high-efficiency quantum state detection. During the waiting time all lasers are shut off and no light interacts with the ion. This method basically is an improved version of a technique that was used earlier to measure the $D_{3/2}$ metastable level lifetime in single Ba^+ ions [26]. The main advantage of this "state detection" method is that no residual light is present during the measurement which could affect the free decay of the atom. In addition, it allows for the measurement of the $D_{3/2}$ level lifetime which otherwise is inaccessible with the quantum jump technique. There exist only a few reported $D_{3/2}$ -level lifetime results for Calcium [15, 16, 18] but none from a single ion experiment.

Figs. 2 and 3 compare the different experimental [13–24] and theoretical [27–32] methods and results for the $D_{5/2}$ - and $D_{3/2}$ -level lifetimes. From Fig. 2 it is evident that the single ion measurements are the most accurate ones. Generally, lifetime measurements on single ions or crystallized ion strings are more accurate as systematic errors, e.g. due to collisions, can be reduced to the highest possible extend. Therefore, single ion D-level lifetime measurements for Calcium are of special interest. The existence of accurate D-state lifetime values is of special interest for theory as well since most studies of alkali-metal atoms were focused on the measurements of the lowest nP -state lifetimes and D-states are much less studied. The properties of D-states are also generally more complicated to accurately calculate owing to large correlation corrections.

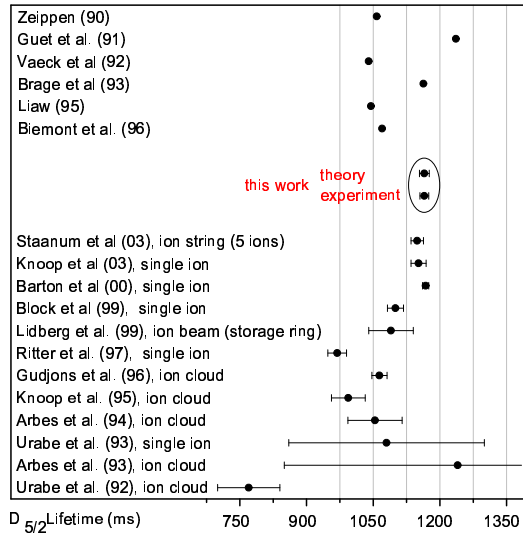


FIG. 2: Theoretical and experimental results for the $D_{5/2}$ -level lifetime.

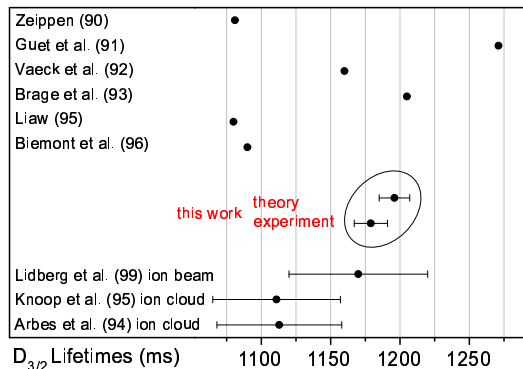


FIG. 3: Theoretical and experimental results for the $D_{3/2}$ -level lifetime.

II. EXPERIMENTAL SETUP AND METHODS

For the experiments, a single $^{40}\text{Ca}^+$ ion is stored in a linear Paul trap in an ultra high vacuum (UHV) environment (10^{-11} mbar range). The Paul trap is designed with four blades separated by 2 mm for radial confinement and two tips separated by 5 mm for axial confinement. Under typical operating conditions we observe radial and axial motional frequencies $(\omega_{r1}, \omega_{r2}, \omega_{ax}) = 2\pi(4.9, 4.9, 1.7)$ MHz. $^{40}\text{Ca}^+$ ions are loaded into the trap using a 2-step photoionization procedure [33]. The trapped $^{40}\text{Ca}^+$ ion has a single valence electron and no hyperfine structure (see Fig. 1). Doppler-cooling on the $S_{1/2} - P_{1/2}$ transition at 397 nm puts the ion in the Lamb-Dicke regime [5, 6]. Diode lasers at 866 nm and 854 nm

prevent optical pumping into the D states during cooling and state preparation. For coherent excitation to the $D_{5/2}$ state we drive the $S_{1/2}$ to $D_{5/2}$ quadrupole transition at 729 nm. A constant magnetic field of 3 G splits the 10 Zeeman components of the $S_{1/2} - D_{5/2}$ multiplet. We detect whether a transition to $D_{5/2}$ has occurred by applying the laser beams at 397 nm and 866 nm and monitoring the fluorescence of the ion on a photomultiplier (PMT), i.e. using the electron shelving technique [34]. The internal state of the ion is discriminated with an efficiency close to 100% within approximately 3 ms [35]. The following stabilized laser sources are used in the experiment: two frequency-stabilized diode lasers at 866 nm and 854 nm with linewidths of ≈ 10 kHz and two Ti:Sa lasers at 729 nm (< 100 Hz linewidth) and 794 nm (< 100 kHz linewidth), of which the 794 nm laser is externally frequency doubled to obtain 397 nm. The experimental setup and the laser sources are described in more detail elsewhere [7, 36].

III. MEASUREMENT OF THE $D_{5/2}$ STATE LIFETIME

A. Measurement procedure and results

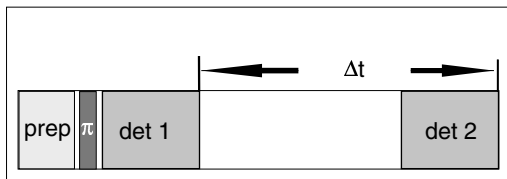


FIG. 4: Simplified pulse scheme for the $D_{5/2}$ lifetime measurement: the preparation consists of Doppler cooling, repumping, and optical pumping (2ms); followed by a π -pulse (few μs) and a detection periods (3.5 ms). The waiting time is varied between 25 ms and 5 s.

The measurements consist of a repetition of laser pulse sequences applied to the ion. The sequence generally is composed of three steps (see Fig. 4):

1. State preparation and Doppler cooling, consisting of 2 ms of Doppler cooling (397 nm and 866 nm light), repumping from the $D_{5/2}$ level (854 nm light) and optical pumping into the $S_{1/2}(m=-1/2)$ Zeeman sublevel (397 nm σ^- polarized light).

2. Coherent excitation at 729 nm with pulse length and intensity chosen to obtain near unity excitation (π -pulse) to the $D_{5/2}(m = -5/2)$ Zeeman level.

3. State detection for 3.5 ms by recording the fluorescence on the $S_{1/2} - P_{1/2}$ transition with a photomultiplier. Discrimination between S and D state is achieved

by comparing the fluorescence count rate with a threshold value. The state is measured before and after a fixed waiting period Δt to determine whether a decay of the excited state has happened.

This three-step cycle is repeated typically several thousand times. The decay probability p is then determined as the ratio of D-state results in the second and the first state detections. For the calculation of the $D_{5/2}$ -state lifetime $\tau_{(5/2)}$ we use an exponential fit function $(1 - p) = \exp\{-\Delta t/\tau_{(5/2)}\}$. For Δt we use the time interval between the ends of the two detection periods.

Fig. 5 shows the measured $D_{5/2}$ -level excitation probability $(1 - p)$ after several delay times ranging from 25 ms up to 5 s. A weighted least squares fit to the data yields the lifetime $\tau_{(5/2)} = 1168(9)$ ms using the fitting function described above, where the only fitting parameter is $\tau_{(5/2)}$. The statistical error (in brackets) is the 1σ standard deviation. The fit yields $\chi^2_\nu = 0.47$, indicating that the experimental decay is consistent with the expected exponential decay behavior. The least-squares method is justified by the normal distribution of the mean decay probabilities which is a result of the 'central limit theorem' of statistics. This was also verified using simulated data sets (see next section).

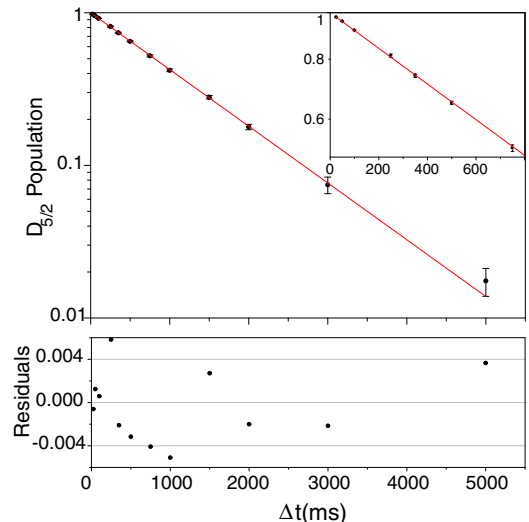


FIG. 5: $D_{5/2}$ -level excitation probability after delay times from 25 ms to 5 s plotted on a logarithmic scale. The solid line is a least squares fit to the data yielding $\tau_{(5/2)} = 1168(9)$ ms. The residuals (difference of data points and fit curve) of the fit are shown in the lower diagram.

B. Systematic errors

There are several types of systematic errors that may affect the lifetime result. In UHV single ion experiments

the biggest error source is usually radiation which irradiates the ion due to insufficient shielding of room light or insufficient shut-off of laser beams. In our experiment, the strongest influence stems from residual light at 854 nm. The influence of this radiation on the $D_{5/2}$ -level lifetime has been investigated extensively in [22]. If radiation at 854 nm is present during the delay interval it may de-excite the $D_{5/2}$ -level to the ground state via the strongly coupled $P_{3/2}$ -level. This additional "decay channel" artificially shortens the observed lifetime. The obvious source for residual 854 nm radiation is the 854 nm diode laser itself. In our experiment, it is eliminated by a fast mechanical shutter [37] which is closed during the delay interval. The 40 dB attenuation of the double-pass AOM which usually switches the 854 nm light was shown to be insufficient: In an earlier experiment without the shutter the lifetime was determined to 1011(6) ms [8]. In addition, the results observed without shutter were found to fluctuate by approximately ± 50 ms depending on the specific AOM and diode laser adjustments.

Another source for 854 nm radiation is background fluorescence at 854 nm from the 866 nm diode laser. To eliminate this radiation an AOM in single pass with an attenuation of more than 20 dB was used to shut the 866 nm beam. As the systematic lifetime error without AOM was found to be of the order of a few percent, this attenuation is sufficient. Note that this source of error cannot, in principle, be directly eliminated in the quantum-jump technique where 866 nm light must be radiated onto the ion continuously. In that case, the only way to correct for this systematic error is to measure at different light powers and extrapolate the lifetime to zero power which in turn implies a larger statistical error. In summary, radiation at 854 nm did not influence the measured $D_{5/2}$ -level lifetime at the given level of statistical uncertainty.

The $D_{5/2}$ -level lifetime could in principle be also reduced by transitions between the D-levels, i.e. by a M1-transition stimulated by thermal radiation. The corresponding transition rate is given by $W_{12} = B_{12}\rho(\nu)$ with the Einstein coefficient for stimulated emission B_{12} and the energy density per unit frequency interval for thermal radiation $\rho(\nu)$. With the rate of spontaneous emission $A_{12} = (8\pi h\nu^3/c^3)B_{12}$, W_{12} is rewritten as:

$$W_{12} = \frac{A_{12}}{e^{h\nu/kT} - 1} \quad (1)$$

With $\nu = 1.82$ THz and $A_{12} = 2.45 \times 10^{-6} \text{ s}^{-1}$ taken from [38] we get $W_{12} = 7.23 \times 10^{-6} \text{ s}^{-1}$ at room temperature which changes the $D_{5/2}$ -level lifetime by much less than the statistical error of our measurement.

Residual radiation could also induce lifetime-enhancing systematic effects. Both radiation at 393 nm (roomlight) or 729 nm (Ti:Sa laser, double-pass AOM attenuation of ≈ 40 dB) can lead to re-shelving of the ion. This effect, however, leads also to a different decay function. It is modeled by a simple rate equation for the

excited state population p_D

$$\dot{p}_D = -\Gamma p_D + R(1 - p_D) \quad (2)$$

where $\Gamma = 1/\tau$ denotes the natural decay rate and R the reshelving rate induced by laser radiation. The solution of eq. (2) is of the form

$$p_D = Ae^{-\Gamma' t} + B \quad (3)$$

with $A = 1 - R/\Gamma'$, an offset $B = R/\Gamma'$ and the new decay rate $\Gamma' = \Gamma + R$. Thus, an offset B is the signature of a re-shelving rate. The result from fitting the experimental data in Fig. 5 with the modified exponential fit function (3) is $\tau_{\text{fit}} = 1165(10)$ ms and $R_{\text{fit}} = 3(2) \times 10^{-3} \text{ s}^{-1}$.

To evaluate the systematic error due to a repumping rate R we use the following technique: We generate simulated data sets from random numbers by considering the fact that the decay probability for a given waiting time is distributed binomially around a mean that is given by an exponential function with an expected mean decay time $\tau_{(5/2)}$. For these data sets we also take into account the particular experimental waiting times and number of measurements. In this way 'ideal' data sets are created that contain a purely statistical variation of data according to the experimental settings and that are free of any systematic errors. First, a fit of Eq. (3) to such an ideal simulated data set yields an additional repumping rate $R = 0$ with a standard deviation of $\Delta R = 3 \times 10^{-3} \text{ s}^{-1}$. Thus, the above fitted repumping rate R_{fit} is consistent with zero and not sufficiently significant to allow any conclusion about the actual rate or the model, i.e. the statistical error is too large for this small systematic error to be resolved in a fit to the data. Second, to obtain an upper limit for the systematic error of the lifetime due to a possible re-pumping rate we assume that such a rate R_{sim} exists in the experiment. We then simulate data sets including the rate R_{sim} and the lifetime $\tau_{(5/2)}$ and fit these data sets with a normal exponential fit function $(1 - p) = \exp(-\Delta t/\tau_{\text{sim}})$. The deviation of the fit result τ_{sim} from $\tau_{(5/2)}$ used for the simulation gives the systematic lifetime error. For $R_{\text{sim}} = 3 \times 10^{-3} \text{ s}^{-1}$ this systematic error is $\Delta\tau = -3$ ms.

Another systematic effect that implies a different fit model is the state detection error. Even though the detection efficiency is close to unity, Poissonian noise in the PMT counts and the possibility of a spontaneous decay during the detection period produce a small error [39]. The first error, i.e. the probability ε_1 to measure the ion in the wrong state due to noise of the count rate, depends on the discrimination between S and D state in the electron shelving technique. Such discrimination is achieved by comparing the fluorescence count rate during the detection window with a threshold value. Proper choice of this threshold value leads to an error as small as $\varepsilon_1 = 10^{-5}$ which can be neglected for the following analysis. The second error, i.e. the probability ε_2 for a wrong state measurement due to spontaneous decay, also depends on the length of the detection window, fluorescent

count rates for the ion in S and D states and the threshold setting. For the chosen parameters in the experiment we evaluate $\varepsilon_2 = 10^{-3}$. The measured excitation probability is then $(1-p)_{\text{meas}} = (1-\varepsilon_2)(1-p)_{\text{real}}$ and implies a model function of the form $(1-p) = (1-\varepsilon_2)e^{-\Gamma\Delta t}$. A fit to simulated data as described above yields a statistically consistent limit for this detection error of $\varepsilon_2 = 1 \times 10^{-3}$. Again, it cannot be resolved by a fit to the measured data. From simulated data including an assumed detection error of $\varepsilon_2 = 1 \times 10^{-3}$ we get an upper limit of the systematic lifetime error $\Delta\tau = 7$ ms.

In addition to radiative effects, non-radiative lifetime reduction mechanisms exist, namely, inelastic collisions with neutral atoms or molecules from the background gas. Two relevant types of collisions can be distinguished: Quenching and j-mixing collisions. Quenching collisions cause direct shelving of the ion into the ground state. In the presence of high quenching rates lifetime measurements have to be done at different pressures. An extrapolation to zero pressure then yields the natural lifetime. Measurements of collisional deshelling rates for different atomic and molecular species have been performed in early experiments [14, 16]. Ref. [16] finds specific quenching rates for Ca^+ of $\Gamma_H^q = 37 \times 10^{-12} \text{ cm}^3\text{s}^{-1}$ for H_2 , and $\Gamma_N^q = 170 \times 10^{-12} \text{ cm}^3\text{s}^{-1}$ for N_2 . Collisions may also induce a change of the atomic polarization, a process called j-mixing or fine structure mixing where a transition from the $\text{D}_{5/2}$ to the $\text{D}_{3/2}$ state or vice versa is induced. These rates have also been determined in Ref.[16] to $\Gamma_H^j = 3 \times 10^{-10} \text{ cm}^3\text{s}^{-1}$ for H_2 and $\Gamma_N^j = 13 \times 10^{-10} \text{ cm}^3\text{s}^{-1}$ for N_2 . Such collisional effects cannot be distinguished from a natural decay process. Collisional effects are most prominent in experiments with large clouds of ions or at higher background pressure. To give an upper limit of the effect in our experiment estimates of the constituents of the background gas must be made. If a background gas composition of 50% N_2 and 50% H_2 is assumed [40] and the pressure $p < 2 \times 10^{-11}$ mbar in the linear ion trap set up is taken into account, an upper limit for the additional collision induced rate of $\gamma = 3 \times 10^{-4} \text{ s}^{-1}$ is calculated. This effect is well below a promille relative error and can be neglected here.

In summary, the result for the lifetime of the $\text{D}_{5/2}$ level can be quoted as: $\tau_{(5/2)} = 1168 \text{ ms} \pm 9 \text{ ms}$ (statistical) -3 ms (repumping rate) $+7 \text{ ms}$ (detection).

IV. MEASUREMENT OF THE $\text{D}_{3/2}$ STATE LIFETIME

A. Measurement procedure and results

For the measurement of the $\text{D}_{3/2}$ -level lifetime some alterations in the pulse sequence are required (see Fig. 6). To populate the $\text{D}_{3/2}$ state we use indirect shelving by driving the S-P transition at 397 nm and taking advantage of the 1:16 branching ratio into the $\text{D}_{3/2}$ level. After

a few microseconds the $\text{D}_{3/2}$ level is populated with unity probability.

Furthermore, because that level is part of the closed 3-level fluorescence cycle used for state detection its population cannot be probed with the state detection scheme described in the previous paragraph. In that sense the $\text{D}_{3/2}$ level is not a shelved state. The method used here is that prior to state detection the decayed population is transferred to the $\text{D}_{5/2}$ shelving state. The measured excitation probability of the $\text{D}_{5/2}$ state divided by the shelving probability then corresponds to the decay probability from the $\text{D}_{3/2}$ level and the further analysis is analogous to the one in Sec. III. Shelving in the $\text{D}_{5/2}$ state is achieved by coherent excitation (π -pulse). However, it must be taken into account that the $\text{D}_{3/2}$ state may decay into both Zeeman sublevels of the $\text{S}_{1/2}$ ground state. Hence, two π pulses from both sublevels are required to transfer all decayed population to the $\text{D}_{5/2}$ -state. In our experiment we chose the two $\Delta m_j = 2$ transitions ($m_j = -1/2$ to $m_j = -5/2$ and $m_j = 1/2$ to $m_j = 5/2$). The combined transfer efficiency P_π of the two pulses is determined in the first part of the pulse sequence (cf. Fig. 6): after Doppler cooling the ion is not optically pumped into the $\text{S}_{1/2}(m_j = -1/2)$ ground state as usual but might populate both Zeeman sublevels. The measured transfer efficiency P_π is used for calculation of the decay probability.

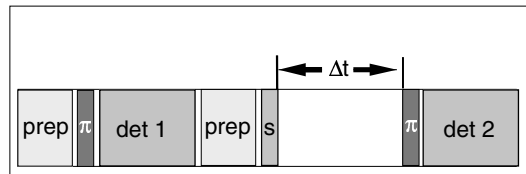


FIG. 6: Simplified pulse scheme for the $\text{D}_{3/2}$ lifetime measurement. It consists of a measurement of the π -pulse transfer efficiency on the $\text{S}_{1/2}$ - $\text{D}_{5/2}$ transition (prep, π and det1); $\text{D}_{3/2}$ -state preparation (prep, s); waiting period Δt and state detection (π and det2). For details of the pulse sequence see text. The waiting time is varied between 25 ms and 5 s.

The measurement of the $\text{D}_{3/2}$ -level lifetime $\tau_{(3/2)}$ thus consists of a repetition of the following laser pulse sequences applied to the ion. The sequence generally is composed of three steps (cf. Fig. 6):

1. Measurement of transfer efficiency P_π : state preparation and Doppler cooling, consisting of 2 ms of Doppler cooling (397 nm and 866 nm light), repumping from the $\text{D}_{5/2}$ level (854 nm light) and spontaneous decay into the $\text{S}_{1/2}(m=-1/2)$ or ($m=+1/2$) Zeeman sublevel; π -pulses on the $\text{S}_{1/2}$ to $\text{D}_{5/2}$ transitions ($m_j = -1/2$ to $m_j = -5/2$ and $m_j = 1/2$ to $m_j = 5/2$); state detection for 3.5 ms by recording the fluorescence on the $\text{S}_{1/2}$ - $\text{P}_{1/2}$ transition with a photomultiplier.

2. State preparation and shelving in the $\text{D}_{3/2}$ -level: 2 ms of Doppler cooling (397 nm and 866 nm light),

repumping from the $D_{5/2}$ level (854 nm light) and optical pumping into the $S_{1/2}(m=-1/2)$ Zeeman sublevel (397 nm σ^- polarized light); shelving pulse at 397 nm for a few μs .

3. Measurement of decay probability: free decay for a variable delay time; π -pulses on the $S_{1/2}$ to $D_{5/2}$ transitions ($m_j = -1/2$ to $m_j = -5/2$ and $m_j = 1/2$ to $m_j = 5/2$); state detection for 3.5 ms by recording the fluorescence on the $S_{1/2}$ - $P_{1/2}$ transition with a photomultiplier.

The measured $D_{3/2}$ -level excitation probability $(1 - p)$ is plotted vs. various delay times between 25 ms and 2 s in Fig. 7. Again, the data have been fitted using the least squares method and the fit function $1 - p = \exp(-\Delta t/\tau_{(3/2)})$. Here, p denotes the corrected decay probability $p = P_{ex}/P_\pi$, i.e. the detected excitation of the $D_{5/2}$ level P_{ex} corrected for the near-unity shelving probability P_π (which is typically 0.98-0.99 on average). Since there is no correlation between P_π and P_{ex} in one experiment it is more appropriate to use for the correction the average of P_π for each delay time. The output from the fit is $\tau_{(3/2)} = 1176(11)$ ms with $\chi^2_\nu = 0.68$ indicating good agreement of data and exponential model.

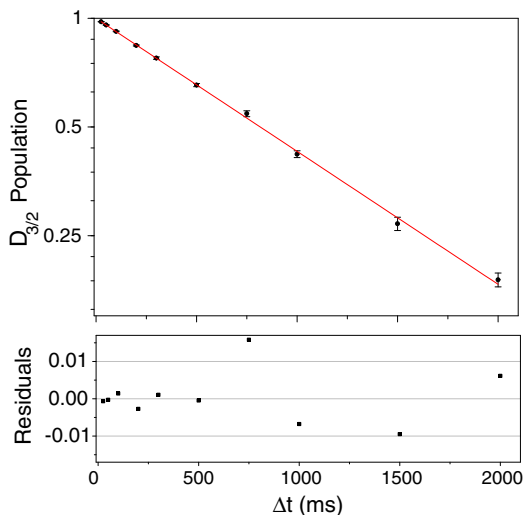


FIG. 7: $D_{3/2}$ -level excitation probability for delay times from 25 ms to 2 s plotted on a logarithmic scale. The solid line is a least squares fit to the data yielding $\tau_{(3/2)} = 1176(11)$ ms. The residuals (difference of data points and fit curve) of the fit are shown in the lower diagram.

B. Systematic errors

Also for this experiment systematic errors due to residual light have to be investigated. The measured lifetime might be reduced by residual light at 866 nm or 850 nm

present during the delay interval. This light would de-excite the $D_{3/2}$ level via the $P_{1/2}$ - or $P_{3/2}$ -levels, respectively, and results in a faster effective decay rate. The main source of light at 866 nm is the corresponding diode laser itself which is switched with a single pass AOM with an attenuation of 20 dB. As this attenuation was found to be insufficient a fast mechanical shutter (cf. Sec. III) was installed which remained closed throughout the entire waiting period. The fluorescence background of the 854 nm diode laser at 866 nm was found to be negligible. Light at 850 nm could de-shelve the ion via the $P_{3/2}$ state and is expected to mainly originate from the fluorescence background of the 854 nm diode laser. For this laser, a double-pass AOM attenuation of 40 dB was proven to be sufficient since no effect on the lifetime could be measured within a 5% error even if the laser was switched on at full intensity during the whole waiting time.

Lifetime reducing effects are not obviously detectable because they only increase the decay rate while the functional shape of the decay curve remains the same, i.e. no offset is introduced for long delay times. The main concern in our experiment is the 866 nm light and extreme care has been taken to ensure that the shutter was indeed closed during the delay time. Before the 397 nm shelving pulse and between the π pulse and the second detection a 1 ms period has been inserted to allow for shutting time and jitter. During the lifetime measurements the correct shutting was checked by monitoring the transmission on photodiodes. In fact the shutters close fast within about 400 μs but the start time is not well defined and jitters by about 500 μs .

Lifetime prolonging effects can be induced by residual light at 397 nm or 729 nm which might re-excite the ion after it has already decayed. This re-shelving process can be detected as an offset as already pointed out in Sec. III. The 397 nm laser light is switched by two single pass AOMs in series (one before a fiber, one behind it, combined attenuation ≈ 55 dB). Nonetheless, we used a shutter to exclude the influence of 397 nm laser light to the largest possible extent. To give a limit on the systematic effect of any re-pumping source the same method as in section III B is applied. The experimental data is fitted with the rate model function Eq. (3) yielding a rate of $R_{\text{fit}} = 3(10) \times 10^{-3} \text{ s}^{-1}$. The standard deviation of R for an simulated ideal data set is $\Delta R = 1.5 \times 10^{-2} \text{ s}^{-1}$ (with mean $R = 0$), so again the rate is concealed by the statistical error. From simulations an upper limit for the systematic lifetime error of $\Delta\tau = -2$ ms is obtained.

Another source of systematic error is vibrational heating of the ion during the delay time. If, due to heating, the transfer efficiency $P_\pi(\Delta t)$ is smaller after the waiting time than $P_\pi(0)$ determined in the first part of the pulse sequence the correction for the transfer efficiency is too small and the actual decay rate is higher than measured. A π pulse only has high transfer efficiency if the ion is in the Lamb-Dicke regime [5, 6], i.e. $\eta^2 \bar{n} \ll 1$ where η is the Lamb-Dicke parameter and \bar{n} is the mean phonon number. If the factor $\eta^2 \bar{n}$ becomes significant both the

Rabi frequency $\Omega_{\bar{n}}$ and the maximum transfer efficiency decrease as $\Omega_{\bar{n}} = \Omega_0(1 - \eta^2\bar{n})$, where Ω_0 is the coupling strength on the S-D transition. Taking the mean phonon number after Doppler cooling of $\bar{n} \approx 10$ and the measured heating rate in the linear ion trap of $\partial n/\partial t \approx 10 \text{ s}^{-1}$ [35] we can estimate the transfer efficiency after a waiting time of 2 s, $P_\pi(2 \text{ s}) = 0.98$ if the π -pulse time was initially chosen to fulfill $P_\pi(0) = 1$. We experimentally checked the degradation of transfer efficiency with waiting time by introducing a delay time Δt between the Doppler cooling pulse and the π -pulse in the first step of the pulse sequence and subsequently performing a state detection measurement. Figure 8 shows an average of various measurements of π -pulse transfer efficiency $P_\pi(\Delta t)$ vs. delay time Δt . A linear fit $P_\pi(\Delta t) = 1 - a\Delta t$ to the data

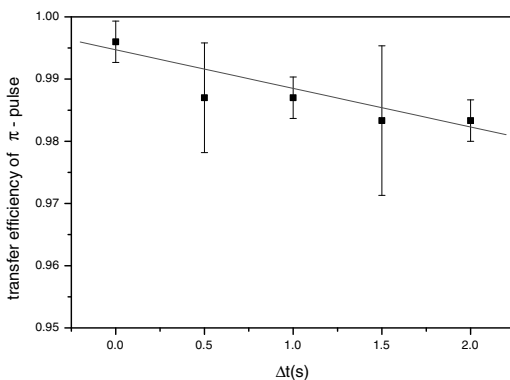


FIG. 8: Average transfer efficiency of the π -pulses on the $S_{1/2}$ to $D_{5/2}$ transition after various delay times between Doppler cooling and π -pulses.

yields $a = -4(2) \times 10^{-3} \text{ s}^{-1}$. With simulated data sets including such a decreasing transfer efficiency $P_\pi(\Delta t)$ we determine a systematic lifetime error of $\Delta\tau = -7 \text{ ms}$.

Finally, the detection error is considered, in analogy to section III B. From simulated data sets with a detection error of $\varepsilon_2 = 1 \times 10^{-3}$ a systematic error for the lifetime of $\Delta\tau = +8 \text{ ms}$ is found. Systematic errors due to collisional effects (quenching and j-mixing) can be again neglected as argued above.

Summarizing the analysis, the lifetime for the $D_{3/2}$ level is given as: $\tau_{(3/2)} = 1176 \text{ ms} \pm 11 \text{ ms}$ (statistical) -2 ms (repumping rate) -7 ms (heating) $+8 \text{ ms}$ (detection error).

V. AB INITIO ALL ORDER CALCULATION OF THE D-STATES LIFETIMES

We conducted the calculation of the 3d $^2D_{3/2}$ - 4s $^2S_{1/2}$ and 3d $^2D_{5/2}$ - 4s $^2S_{1/2}$ electric-quadrupole matrix elements in Ca^+ using a relativistic all-order method which sums infinite sets of many-body perturbation theory terms. These matrix elements are used to evaluate

the 3d-level radiative lifetimes and their ratio.

In this particular implementation of the all-order method, the wave function of the valence electron v is represented as an expansion

$$|\Psi_v\rangle = \left[1 + \sum_{ma} \rho_{ma} a_m^\dagger a_a + \frac{1}{2} \sum_{mnab} \rho_{mnab} a_m^\dagger a_n^\dagger a_b a_a + \sum_{m \neq v} \rho_{mv} a_m^\dagger a_v + \sum_{mna} \rho_{mnva} a_m^\dagger a_n^\dagger a_a a_v + \frac{1}{6} \sum_{mnrab} \rho_{mnrwab} a_m^\dagger a_n^\dagger a_r^\dagger a_b a_a a_v \right] |\Phi_v\rangle, \quad (4)$$

where Φ_v is the lowest-order atomic wave function, which is taken to be the *frozen-core* Dirac-Hartree-Fock (DHF) wave function of a state v . This lowest-order atomic wave function can be written as $|\Phi_v\rangle = a_v^\dagger |0_C\rangle$, where $|0_C\rangle$ represents DHF wave function of a closed core. In equation (4), a_i^\dagger and a_i are creation and annihilation operators, respectively. The indices m , n , and r designate excited states and indices a and b designate core states. The first two lines of Eq. (4) represent the single and double excitation terms. The restriction of the wave function to the first five terms of Eq. (4) represents a single-double (SD) approximation. The last term of Eq. (4) represents a class of the triple excitations and is included in the calculation partially as described in Ref. [41]. We carried out the all-order calculation with and without the partial addition of the triple term; the results of those two calculations are labeled SD (single-double) and SDpT (single-double partial triple) data in the text and tables below. The excitation coefficients ρ_{ma} , ρ_{mv} , ρ_{mnab} , and ρ_{mnva} are obtained as the iterative solutions of the all-order equations in the finite basis set. The basis set, used in the present calculation, consists of the single-particle states, which are linear combinations of B-splines [42]. The single-particle orbitals are defined on a non-linear grid and are constrained to a spherical cavity. The cavity radius is chosen to accommodate the 4s and 3d orbitals.

The matrix element of the operator Z for the transition between the states w and v is obtained from the expansion (4) using

$$Z_{wv} = \frac{\langle \Psi_w | Z | \Psi_v \rangle}{\sqrt{\langle \Psi_v | \Psi_v \rangle \langle \Psi_w | \Psi_w \rangle}}. \quad (5)$$

The resulting expression for the numerator of the Eq. (5) consists of terms that are linear or quadratic functions of the excitation coefficients. We refer the reader to Refs. [41, 43, 44] for further description of the all-order method.

The numerical implementation of the all-order method requires to carry out the sums over the entire basis set. We truncate those sums at some value of the orbital angular momentum l_{max} ; $l_{max} = 6$ in the current all-order calculation. The contributions of the excited states with higher values of l which are small but significant for the considered transitions, are evaluated in the third-order

TABLE I: Electric-quadrupole reduced matrix elements $E2$ in Ca^+ (in a.u.) calculated using different approximations: Dirac-Hartree-Fock (DHF), third-order many-body perturbation theory (Third order), single-double all-order method (SD), and single-double all-order method including partial triple excitation contributions (SDpT). The all-order data calculated with $l_{\text{max}} = 6$ are listed separately. The contribution of basis set states with orbital angular momentum $l = 7 - 10$ calculated using third-order MBPT is listed in rows labeled “Extr.”. This correction is added to obtain the values listed in rows labeled “SD” and “SDpT”.

Transition	Method	Value
$3d\ ^2D_{3/2} - 4s\ ^2S_{1/2}$	DHF	9.767
	Third order	7.364
	$SD_{l_{\text{max}}=6}$	7.788
	$SDpT_{l_{\text{max}}=6}$	7.971
	Extr. ^a	-0.038
	SD	7.750
	SDpT	7.934
$3d\ ^2D_{5/2} - 4s\ ^2S_{1/2}$	DHF	11.978
	Third order	9.046
	$SD_{l_{\text{max}}=6}$	9.562
	$SDpT_{l_{\text{max}}=6}$	9.786
	Extr. ^a	-0.046
	SD	9.516
	SDpT	9.740

^aThis value is the difference of the third-order result obtained with the same basis set as the all-order calculation (the number of splines $N = 35/40$ and $l_{\text{max}} = 6$) and third-order result with $N = 70$ and $l_{\text{max}} = 10$.

many-body perturbation theory (MBPT). To evaluate those contributions, we carried out a third-order MBPT calculation with the same basis set and l_{max} , used the all-order calculation and then repeated the third-order calculation with larger basis set containing the orbitals with l up to $l_{\text{max}} = 10$. The difference between these two results is added to the *ab initio* all-order results. The convergence of the MBPT terms with l is rather rapid; the differences between the third-order calculations with $l_{\text{max}} = 4, 6, 8, 10$ are 1.8%, 0.4%, and 0.1%, respectively. The last number is well below the expected uncertainty of the current calculation. Thus, the contribution from orbitals with $l_{\text{max}} > 10$ can be omitted at the present level of accuracy. The contribution from the excited states with $l_{\text{max}} > 6$ relative to the total value of the matrix elements is significantly larger for $4s - 3d$ electric-quadrupole transitions (about 0.5%) than for the primary $ns - np$ electric-dipole transitions in alkali-metal atoms. We note that while the all-order matrix elements contain the entire third-order perturbation theory contribution there is no straightforward and simple way to directly separate it out (see Ref. [45] for the all-order vs.

perturbation theory term correspondence issue). Thus, we have conducted a separate third-order calculation following Ref. [46]. The results of the third-order and the all-order calculations (with and without partial inclusion of the triple excitations) are listed in Table I. The contribution from the excited states with orbital angular momentum $l > 6$ calculated as described above is listed in the row labeled “Extr.”. The all-order values corrected for the truncation of the higher partial waves are listed in rows labeled “SD” and “SDpT”.

We also investigated the effect of the Breit interaction to the values of the electric-quadrupole matrix elements. The Breit interaction arises from the exchange of a virtual photon between atomic electrons. The static Breit interaction can be described by the operator

$$B_{ij} = -\frac{1}{r_{ij}} \boldsymbol{\alpha}_i \cdot \boldsymbol{\alpha}_j + \frac{1}{2r_{ij}} [\boldsymbol{\alpha}_i \cdot \boldsymbol{\alpha}_j - (\boldsymbol{\alpha}_i \cdot \hat{\mathbf{r}}_{ij})(\boldsymbol{\alpha}_j \cdot \hat{\mathbf{r}}_{ij})] \quad (6)$$

where the first part results from instantaneous magnetic interaction between Dirac currents and the second part is the retardation correction to the electric interaction [47]. In Eq. (6), $\boldsymbol{\alpha}_i$ are Dirac matrices. The complete expression for the Breit matrix elements is given in [48]. To calculate the correction to the matrix elements arising from the Breit interaction, we modified the generation of the B-spline basis set to intrinsically include the Breit interaction on the same footing as the Coulomb interaction and repeated the third-order calculation with the modified basis set. The difference between the new values and the original third-order calculation (conducted with otherwise identical basis set parameters) is taken to be the correction due to Breit interaction. We give the breakdown of the third-order calculation with and without inclusion of the Breit interaction in Table II. The Dirac-Hartree-Fock values are given in column DHF. The random-phase approximation (RPA) values, iterated to all orders, are listed in column RPA. The third-order Brueckner-orbital, structure radiation and normalization terms are listed in the columns BO, SR, and Norm, respectively. The breakdown of the third-order calculation to RPA, BO, structure radiation and normalization terms follows that of Ref. [46]. The reader is referred to Ref. [46] for the detailed description of the third-order MBPT method and the formulas for all of the terms. We find the Breit correction to the DHF contribution to be dominant, with the contributions from all other terms being insignificant. The total Breit correction is very small and below the estimated uncertainty of our theoretical values discussed below. However, the Breit contribution to the ratio of the matrix elements is found to be small but significant owing to higher accuracy of the ratio.

The procedure described above does not include a class of the Breit correction contributions referred to in Ref. [49] as two-body Breit contribution [50]. To conduct the study of the possible size of the two-body Breit contribution we calculated the Breit contribution to 10 different electric-dipole matrix elements ($6s - 6p$, $6s - 7p$, $7s - 7p$, $7s - 6p$, and $5d_{3/2} - 6p$) in Cs using the method

TABLE II: The Breit correction to the third-order values of the $4s\ ^2S_{1/2} - 3d\ ^2D_{3/2}$ and $4s\ ^2S_{1/2} - 3d\ ^2D_{5/2}$ electric-quadrupole matrix elements. The Dirac-Hartree-Fock values are given in column DHF. The random-phase approximation (RPA) values, iterated to all orders, are listed in column RPA. The third-order Brueckner-orbital, structure radiation, and normalization terms are listed in the columns BO, SR, and Norm, respectively.

Transition		DHF	RPA	BO	SR	Norm	Total
$4s\ ^2S_{1/2} - 3d\ ^2D_{3/2}$	no Breit	9.7673	-0.0553	-2.2136	0.0621	-0.1588	7.4018
	with Breit	9.7611	-0.0552	-2.2131	0.0621	-0.1589	7.3961
	Difference	-0.0062	0.0001	0.0005	0.0000	-0.0001	-0.0057
$4s\ ^2S_{1/2} - 3d\ ^2D_{5/2}$	no Breit	11.9782	-0.0662	-2.7006	0.0756	-0.1945	9.0926
	with Breit	11.9672	-0.0662	-2.7001	0.0756	-0.1946	9.0820
	Difference	-0.0110	0.0000	0.0005	0.0000	-0.0001	-0.0106

described above and compared those values with the results from [49]. Cs is chosen as “model” atom as it is a similar system compared to Ca^+ . The Breit contribution to Cs properties was studied in detail owing to its importance for the interpretation of Cs parity nonconservation experiments. In Ref. [49], both one-body and dominant two-body Breit contributions have been taken into account. We find the largest difference between our data and that of [49] to be 25%. For most of the transitions, we either agree to all the digits quoted in [49] or differ by 10% or less. Therefore, the two-body contribution was not significant for any of the Cs electric-dipole transitions that we could compare with. We agree with the values of the Breit correction to the DHF matrix elements given in Ref. [49] exactly, as expected, since the two-body Breit contribution only affects the correlation part of the calculation. Thus, we found no evidence that the two-body Breit correction may exceed the already calculated one-body correction, especially considering the fact that the Breit correction to the lowest-order DHF value dominates the one-body Breit correction to the $4s - 3d$ matrix elements in Ca^+ . Therefore, we assume that the two-body Breit contribution does not exceed the already calculated part. In summary, the omission of the two-body Breit interaction introduces an additional uncertainty in our calculation and we take the uncertainty to be equal to the value of the correction itself. Most likely, it is an overly pessimistic assumption based on the comparison with the calculation of the Breit correction to Cs electric-dipole matrix elements carried out in Ref. [49].

Next, we use a semi-empirical scaling procedure to evaluate some classes of the correlation correction omitted by the current all-order calculation. The scaling procedure is described in Refs. [44, 45]. Briefly, the single-valence excitation coefficients ρ_{mv} are multiplied by the ratio of the corresponding experimental and theoretical correlation energies and the calculation of the matrix elements is repeated with those modified excitation coefficients. This procedure is especially suitable in this particular study since the matrix element contribution containing the excitation coefficients ρ_{mv} overwhelmingly dominates the correlation correction for the considered here transitions. We conduct this scaling procedure for both

SD and SDpT calculations; the scaling factors are different in these two cases as SD method underestimates and SDpT method overestimates the correlation energy.

Table III contains the summary of the resulting matrix elements; the Breit correction is included in all values. We note that the scaled values only include DHF part of the Breit correction to avoid possible double counting of the terms (because of the use of the experimental correlation energy in the scaling procedure). The final values are taken to be scaled SD values based on the comparisons of similar calculations in alkali-metal atoms with experiment [41, 45, 51]. The uncertainty is calculated as the spread of the scaled values and *ab initio* SDpT values. The uncertainty in the Breit interaction calculation is also included; it is negligible in comparison with the spread of the values.

 TABLE III: Electric-quadrupole reduced matrix elements $E2$ in Ca^+ (a.u.)

Transition	Method	<i>ab initio</i>	scaled
$3d\ ^2D_{3/2} - 4s\ ^2S_{1/2}$	SD	7.744	7.939
	SDpT	7.928	7.902
	Final		7.939(37)
$3d\ ^2D_{5/2} - 4s\ ^2S_{1/2}$	SD	9.505	9.740
	SDpT	9.729	9.694
	Final		9.740(47)

We use our final theoretical results to calculate the lifetimes of the $D_{3/2}$ and $D_{5/2}$ states in Ca^+ . The transition probabilities A_{vw} are calculated using the formula [52]

$$A_{vw} = \frac{1.11995 \times 10^{18}}{\lambda^5} \frac{|\langle v || Q || w \rangle|^2}{2j_v + 1} s^{-1}, \quad (7)$$

where $\langle v || Q || w \rangle$ is the reduced electric-quadrupole matrix element for the transition between states v and w and λ is corresponding wavelength in Å. The lifetime of the state

v is calculated as

$$\tau_v = \frac{1}{\sum_w A_{vw}}. \quad (8)$$

In both $D_{3/2}$ and $D_{5/2}$ lifetime calculations we consider a single transition contributing to each of the lifetimes. The transition probabilities of other transitions (M1 $D_{3/2} - S_{1/2}$, M1 $D_{5/2} - D_{3/2}$, and E2 $D_{5/2} - D_{3/2}$) have been estimated in Ref. [38] and have been found to be 6 to 13 orders of magnitude smaller than the transition probabilities of the $D_{3/2} - S_{1/2}$ and $D_{5/2} - S_{1/2}$ E2 transitions. Thus, we neglect these transitions in the present study. The experimental energy levels from Ref. [53] are used in our calculation of the lifetimes. From the calculations we yield $\tau_{(3/2)} = 1196(11)$ ms for the $D_{3/2}$ -state and $\tau_{(5/2)} = 1165(11)$ ms for the $D_{5/2}$ -state. These lifetime values are compared with experimental and other theoretical results in Figs. 2 and 3.

The all-order calculation is in agreement with the present experimental values and recent experiments [22–24] within the uncertainty bounds. The present calculation includes the correlation correction, which is large (23%) for the considered transitions, in the most complete way with comparison to all other previous calculations [27–29, 31, 38] and is expected to give the most accurate result. It is also the only calculation which gives an estimate of the uncertainty of the theoretical values.

In Ref. [22], the issue of the theoretical ratio of the $\tau_{(3/2)}/\tau_{(5/2)}$ lifetimes was raised. It appeared that there was a disagreement between previously calculated theoretical ratios; Barton *et al.* [22] quotes the values 1.0283 [28], 1.0175 [29], and 1.0335 [31]. Such a disagreement appears to be rather puzzling since this particular ratio is far less sensitive to the correlation correction than the values of the corresponding matrix elements. Thus, we studied the value of the ratio and its uncertainty in detail. We list the values of the ratio of the $D_{3/2}$ and $D_{5/2}$ lifetimes calculated in various approximations in Table IV. The experimental energy levels from Ref. [53] are used in all our calculations of the lifetimes for consistency. We include results with and without the addition of the Breit correction. As mentioned before, we find that the ratio does not change substantially with the addition of the correlation correction; in fact, the correlation only contributes about 0.15% to the final value. Thus, we calculate the uncertainty in the ratio by considering the spread of the high-precision values of the ratio itself (SD_{sc} , SD_{pT} , and $SD_{pT_{sc}}$), rather than calculating the uncertainty in the ratio from the uncertainties in the individual matrix elements. We also find that while the Breit correction to the values of the matrix elements was insignificant at the current level of accuracy this is not the case for the ratio. In fact, the shift of the ratio values with the addition of the Breit interaction is of the same order of magnitude as the spread of the high precision values as demonstrated in Table IV. We take the SD_{sc} value to be our final result for consistency with the calculation of the matrix elements. The uncertainty

of the final value includes both the uncertainty in the correlation correction contribution and the uncertainty in the Breit interaction. As in the case of the individual matrix elements, the uncertainty in the Breit interaction is taken to be equal to the contribution itself. The Breit correction to the ratio is determined as the shift in the final ratio value due to addition of the Breit interaction.

We compare our final theoretical value of the lifetime ratio with the experiment and other theory in Table V. The ratios of the other theoretical values [27–29, 31, 38] are calculated from the numbers in the original publications; care was taken to keep the number of digits in the ratio consistent with the number of digits in the values of the lifetimes or transition rates quoted in the papers. First, we discuss the above mentioned discrepancy of the theoretical ratios. Ref. [22] lists the following ratios: 1.0283 [28], 1.0175 [29], and 1.0335 [31]. We have listed the data from the original publications in Table V which shows that the actual numbers with taking into account the number of digits quoted in the original papers should have been $1271/1236=1.028$ [28], $1.16/1.14=1.02$ [29], and $1080/1045=1.033$ [31]. The first result is essentially a third-order relativistic many-body perturbation theory calculation with addition of semi-empirical scaling and omission of the some classes of small but significant third-order terms. It is very close to our third-order number 1.0286 from Table IV. The next paper [29] quotes only 3 digits in the lifetime values (1.16s and 1.14s) so the accuracy is insufficient to obtain the fourth digit in the ratio. We note that the method description in [29] is that of the non-relativistic calculation and it is unclear how the separation to $D_{3/2}$ and $D_{5/2}$ lifetimes was made. The last calculation yields a larger ratio but that calculation has serious numerical issues such as taking only 20 out of 40 B-splines and including too few partial waves. It also omits all terms except Brueckner-orbital ones and possibly even third-order Brueckner orbital contributions, which are large. The paper is not clear on the subject of the treatment of the higher-order contributions. Thus, we do not consider the result of [31] to be reliable. Therefore, there are essentially no inconsistencies in the previously calculated theoretical ratios when the accuracy of the calculations is taken into account. Our theoretical value of the lifetime ratio is higher than the experimental value. The spread of all values in Table V, including even lowest-order DHF values, is so small that it does not appear probable that any omitted Coulomb correlation or two-body Breit interaction can be responsible for the discrepancy. The only transition which can actually reduce the value of the theoretical ratio is the $D_{3/2}-S_{1/2}$ M1 transition. Thus, an accurate calculation of this transition rate will be useful in search for a theoretical explanation of the discrepancy. However, the transition rate published in [38] is extremely small ($A_{M1} = 7.39 \times 10^{-11} s^{-1}$) and has to be incorrect by many orders of magnitude to affect the ratio at such a level which does not appear likely since the same calculation gives a reasonably good (within 18%) number for

TABLE IV: The ratio of the $D_{3/2}$ and $D_{5/2}$ lifetimes in Ca^+ in various approximations. The lowest-order Dirac-Hartree-Fock results are labelled “DHF”, third-order many-body perturbation theory results are in column labelled “Third”, the results of the *ab initio* all-order calculation including single and double excitations are labeled “SD”, the results of the *ab initio* all-order calculation including single and double excitations with partial addition of the triple excitations are labeled “SDpT”, and the results of the corresponding scaled calculations are given in columns labeled “SD_{sc}” and “SDpT_{sc}”, respectively.

	DHF	Third	SD	SDpT	SD _{sc}	SDpT _{sc}	Final
No Breit	1.0251	1.0286	1.0275	1.0272	1.0266	1.0267	
With Breit	1.0245	1.0278	1.0267	1.0265	1.0259	1.0260	1.0259(9)

TABLE V: Comparison of the present values of the ratio of the $D_{3/2}$ and $D_{5/2}$ state lifetimes in Ca^+ with other theory.

	Reference	Value
Theory	[38]	1.03
	[27]	1.02
	[28]	1.028
	[29]	1.02
	[31]	1.033
	Present	1.0259(9)
Expt.	Present	1.0068(122)

the $D_{3/2}$ - $S_{1/2}$ E2 transition rate.

VI. DISCUSSION

Figures 2 and 3 show an overview of the most recent experimental and theoretical results for the lifetime of the $D_{5/2}$ and $D_{3/2}$ states, respectively, in an chronological order. It is remarkable that the theoretical predictions scatter rather widely, with no noticeable convergence while the experimental results show a trend towards longer lifetimes in the recent years as more systematic errors are identified and stamped out.

In comparison with previous work it can be concluded here that our lifetime result for the $D_{5/2}$ level agrees with and thereby confirms the most precise value of Barton *et al.* We stress that this lifetime measurement is an independent check of earlier results as we used a different measurement technique. In addition, the result for the $D_{3/2}$ level represents the first single ion measurement and reduces the statistical uncertainty of the previous values for the lifetime by a factor of four.

For the calculated lifetimes we find excellent agreement of the theoretical all-order lifetimes with the experimental results. Such agreement demonstrates the necessity of including partially the triple contributions to the all-order calculations for these types of transitions and confirms that scaling of the single-double all-order results, which is significantly simpler and less time consuming calculation in comparison with *ab initio* inclusion

of partial triple excitations, is adequate for these types of transitions. This is an important result for the evaluation of the accuracy of similar theoretical calculation in Ba^+ which is important to parity violating experiments in heavy atoms. Such experiments are aimed at the tests of the Standard model of the electroweak interaction and at the study of the nuclear anapole moments. One of the features of most PNC studies in heavy atoms is the need for comparable accuracy of theoretical and experimental data. The current study is also of interest in regard to recently found discrepancy between the $5d$ lifetimes and the $6s - 6p$ Stark shifts in Cs [54]. Atomic properties of cesium were studied extensively by both experimentalists and theorists owing to a high-precision measurement of parity non-conserving amplitude in this atom. Both of these quantities depend on the values of the $5d - 6p$ matrix elements. While those matrix elements are the electric-dipole ones rather than the electric-quadrupole ones studied here, the calculation itself as well as the breakdown of the correlation correction terms is very similar to the present calculation. Thus, the current study presents an important benchmark in the field of high-precision measurements and calculations. The study of the lifetime ratio demonstrated that the Breit interaction, which produces only a very small correction to the values of the actual matrix elements, is important in high-precision calculations of the corresponding matrix element ratios.

VII. ACKNOWLEDGEMENTS

This work is supported by the Austrian ‘Fonds zur Förderung der wissenschaftlichen Forschung’ (SFB15), by the European Commission: IHP network ‘QUEST’ (HPRN-CT-2000-00121), Marie Curie Research Training network ‘CONQUEST’ (MRTN-CT-2003-505089) and IST/FET program ‘QUBITS’ (IST-1999-13021), and by the ‘Institut für Quanteninformation GmbH’. C. Russo acknowledges support by Fundação para a Ciência e a Tecnologia (Portugal) under the grant SFRH/BD/6208/2001. H. H. is funded by the Marie-Curie-program of the European Union.

-
- [1] P. Gill, G.P. Barwood, H.A. Klein, G. Huang, S.A. Webster, P.J. Blythe, K. Hosaka, S.N. Lea, and H.S. Margolis, *Meas. Sci. Technol.* **14**, 1174 (2003).
- [2] S.A. Diddams, T. Udem, J.C. Bergquist, E.A. Curtis, R.E. Drullinger, L. Hollberg, W.M. Itano, W.D. Lee, C.W. Oates, K.R. Vogel, and D.J. Wineland, *Science* **293**, 825 (2001).
- [3] R.J. Rafac, B.C. Young, J.A. Beall, W.M. Itano, D.J. Wineland, and J.C. Bergquist, *Phys. Rev. Lett.* **85**, 2462 (2000).
- [4] G. Werth in *Applied Laser Spectroscopy* (eds. W. Demtröder and M. Inguscio), NATO ASI Series B, Vol. 241, 479, (Plenum Press, New York, 1990).
- [5] D. Leibfried, R. Blatt, C. Monroe, and D.J. Wineland, *Rev. Mod. Phys.* **75**, 281 (2003).
- [6] M. Šašura and V. Bužek, *J. Mod. Opt.* **49**, 1593 (2002)
- [7] H.C. Nägerl, Ch. Roos, D. Leibfried, H. Rohde, G. Thalhammer, J. Eschner, F. Schmidt-Kaler, R. Blatt: *Phys. Rev. A* **61**, 023405 (2000)
- [8] F. Schmidt-Kaler, S. Gulde, M. Riebe, T. Deuschle, A. Kreuter, G. Lancaster, C. Becher, J. Eschner, H. Häffner, and R. Blatt, *J. Phys. B: At. Mol. Opt. Phys.* **36**, 623 (2003)
- [9] C.F. Roos, G.P.T. Lancaster, M. Riebe, H. Häffner, W. Hänsel, S. Gulde, C. Becher, J. Eschner, F. Schmidt-Kaler, and R. Blatt, *Phys. Rev. Lett.* **92**, 220402 (2004).
- [10] L.M. Hobbs, A.M. Lagrange-Henri, R. Ferlet, A. Vidal-Madjar, and D.E. Welty, *Astrophys. J.* **334**, L41 (1988).
- [11] D.E. Welty, D.C. Morton, and L.M. Hobbs, *Astrophys. J.* **106**, 533 (1996).
- [12] T.W. Koerber, M.H. Schacht, W. Nagourney, and E.N. Fortson, *J. Phys. B.* **36**, 637 (2003).
- [13] S. Urabe, M. Watanabe, H. Imajo, and K. Hayasaka, *Opt. Lett.* **17**, 1140 (1992).
- [14] F. Arbes, T. Gudjons, F. Kurth, G. Werth, F. Marin, and M. Inguscio, *Z. Phys. D* **25**, 295 (1993).
- [15] F. Arbes, M. Benzing, T. Gudjons, F. Kurth, and G. Werth, *Z. Phys. D* **29**, 159 (1994).
- [16] M. Knoop, M. Vedel, and F. Vedel, *Phys. Rev. A* **52**, 3763 (1995).
- [17] T. Gudjons, B. Hilbert, P. Seibert, and G. Werth, *Europhys. Lett.* **33**, 595 (1996).
- [18] J. Lidberg, A. Al-Khalili, L.-O. Norlin, P. Royen, X. Tordoir, and S. Mannervik, *J. Phys. B: At. Mol. Opt. Phys.* **32**, 757 (1999).
- [19] S. Urabe, K. Hayasaka, M. Watanabe, H. Imajo, R. Ohmukai, and R. Hayashi, *Appl. Phys. B* **57**, 367 (1993).
- [20] G. Ritter and U. Eichmann, *J. Phys. B: At. Mol. Opt. Phys.* **30**, L141 (1997).
- [21] M. Block, O. Rehm, P. Seibert, and G. Werth, *Eur. Phys. J. D* **7**, 461 (1999).
- [22] P.A. Barton, C.J.S. Donald, D.M. Lucas, D.A. Stevens, A.M. Steane, and D.N. Stacey, *Phys. Rev. A* **62**, 032503 (2000).
- [23] M. Knoop, C. Champenois, G. Hagel, M. Houssin, C. Lisowski, M. Vedel, and F. Vedel, *Eur. Phys. J. D* **29**, 163 (2004).
- [24] P. Staunum, I.S. Jensen, R.G. Martinussen, D. Voigt, and M. Drewsen, *Phys. Rev. A* **69**, 32503 (2004).
- [25] A. Kreuter, C. Becher, G.P.T. Lancaster, A.B. Mundt, C. Russo, H. Häffner, C. Roos, J. Eschner, F. Schmidt-Kaler, and R. Blatt, *Phys. Rev. Lett.* **92**, 203002 (2004).
- [26] N. Yu, W. Nagourney, and H. Dehmelt, *Phys. Rev. Lett.* **78**, 4898 (1997).
- [27] C.J. Zeippen, *Astron. Astrophys.* **229**, 248 (1990).
- [28] C. Guet and W.R. Johnson, *Phys. Rev. A* **44**, 1531 (1991).
- [29] N. Vaeck, M. Godefroid, and C. Froese-Fischer, *Phys. Rev. A* **46**, 3704 (1992).
- [30] T. Brage, C. Froese-Fischer, N. Vaeck, M. Godefroid, and A. Hibbert, *Physica Scripta* **48**, 533 (1993).
- [31] S.S. Liaw, *Phys. Rev. A* **51**, R1723 (1995).
- [32] E. Biemont and C.J. Zeippen, *Comments At. Mol. Phys.* **33**, 29 (1996).
- [33] S. Gulde, D. Rotter, P. A. Barton, F. Schmidt-Kaler, and R. Blatt, *Appl. Phys. B* **73**, 861 (2001).
- [34] H. Dehmelt: *Bull. Am. Phys. Soc.* **20**, 60 (1975); W. Nagourney, J. Sandberg, and H. Dehmelt, *Phys. Rev. Lett.* **56**, 2797 (1986); Th. Sauter, W. Neuhauser, R. Blatt, and P. E. Toschek, *ibid* **57**, 1696 (1986); J. C. Bergquist, R. G. Hulet, W. M. Itano, D. J. Wineland, *ibid* **57**, 1699 (1986).
- [35] Ch. Roos, Th. Zeiger, H. Rohde, H.C. Nägerl, J. Eschner, D. Leibfried, F. Schmidt-Kaler, and R. Blatt, *Phys. Rev. Lett.* **83**, 4713 (1999).
- [36] F. Schmidt-Kaler, H. Häffner, S. Gulde, M. Riebe, G.P.T. Lancaster, T. Deuschle, C. Becher, W. Hänsel, J. Eschner, C.F. Roos, and R. Blatt, *Appl. Phys. B* **77**, 789 (2003).
- [37] Densitron, TK-CMD series. Using suitable electronics for the shutter drive, closing and opening times of the order of 0.5 ms can be achieved. The timing jitter is on the same time scale.
- [38] M.A. Ali and Y.K. Kim, *Phys. Rev. A* **38**, 3992 (1988).
- [39] C. Roos, Ph.D. thesis, University of Innsbruck (2000).
- [40] Assumption based on the mass spectrometer analysis in the Aarhus ion trap experiment [24].
- [41] M.S. Safronova, W.R. Johnson, and A. Derevianko, *Phys. Rev. A* **60**, 4476 (1999).
- [42] W.R. Johnson, S.A. Blundell, and J. Sapirstein, *Phys. Rev. A* **37**, 307 (1998).
- [43] S.A. Blundell, W.R. Johnson, Z.W. Liu, and J. Sapirstein, *Phys. Rev. A* **40**, 2233 (1989).
- [44] S.A. Blundell, W.R. Johnson, and J.Sapirstein, *Phys. Rev. A* **43**, 3407 (1991).
- [45] M.S. Safronova, Ph.D. thesis, University of Notre Dame (2000).
- [46] W.R. Johnson, Z.W. Liu, and J. Sapirstein, *At. Data and Nucl. Data Tables* **64**, 279 (1996).
- [47] W.R. Johnson and K. T. Cheng, in *Atomic Inner-Shell Physics*, edited by B. Crasemann (Plenum press, New York, 1985), pp. 3-30.
- [48] W.R. Johnson, S.A. Blundell, and J. Sapirstein, *Phys. Rev. A* **37**, 2764 (1998).
- [49] A. Derevianko, *Phys. Rev. A* **65**, 012106 (2002).
- [50] The Breit interaction is a two-particle interaction just as the Coulomb interaction. The separation of the Breit contribution to “one-body” and “two-body” parts results from transforming the Breit operator in second quantization to normal form as described in Ref. [49].
- [51] M.S. Safronova, C.J. Williams, and C.W. Clark, *Phys.*

F New experimental and theoretical approach to the 3d ²D-level lifetimes of ⁴⁰Ca⁺ 13

- Rev. A **69**, 022509 (2004).
- [52] W.R. Johnson, *Lecture Notes on Atomic Physics*, <http://www.nd.edu/~johnson>
- [53] *NIST Atomic Spectra Database* Available online: http://physics.nist.gov/cgi-bin/AtData/main_asd
- [54] M.S. Safronova and C.W. Clark, Phys. Rev. A **69**, 040501 (2004).

Bibliography

- [1] E. M. Purcell, Phys. Rev. **69** 681 (1946)
- [2] D. Wineland, P. Ekstrom, and H. Dehmelt, Phys. Rev. Lett. **31**, 1279 (1973)
- [3] W. Neuhauser, M. Hohenstatt, P.E. Toschek, and H. Dehmelt, Phys. Rev. A. **22**, 1137 (1980)
- [4] R. P. Feynman, Int.J.Theor.Phys. **21**, 467 (1982)
- [5] e.g. M. Horodecki, Quantum Information and Computation, **1**, 3 (2001) or J.R. Gitting and A.J. Fischer, Phys. Rev. A **66**, 032305 (2002)
- [6] D. Deutsch and R. Josza, Proc. R. Soc. London A **439**,553 (1992)
- [7] P.W. Shor, Proc. 35th Annual Symposium on the Foundation of Computer Science (1994)
- [8] L.K. Grover, Phys. Rev. Lett, **79**, 325 (1997)
- [9] ARDA roadmap for Quantum Computation
- [10] J.I. Cirac and P. Zoller, Phys. Rev. Lett. **74**, 4091 (1995)
- [11] D.P. DiVincenzo, Fortschritte der Physik, **48**, 771 (2000)
- [12] S. Gulde, M. Riebe, G.P.T. Lancaster, C. Becher, J. Eschner, H. Häffner, F. Schmidt-Kaler, I.L. Chuang, R. Blatt, Nature **421**, 48 (2003)
- [13] F. Schmidt-Kaler, H. Häffner, M. Riebe, S. Gulde, G.P.T. Lancaster, T. Deuschle, C. Becher, C.F. Roos, J. Eschner, and R. Blatt, Nature **422**, 408 (2003)
- [14] D. Leibfried, B. DeMarco, V. Meyer, D. Lucas, M. Barrett, J. Britton, W.M. Itano, B. Jelenković, C. Langer, T. Rosenband, and D.J. Wineland, Nature **422**, 412 (2003)

Bibliography

- [15] M. Riebe, H. Häffner, C. F. Roos, W. Hänsel, J. Benhelm, G. P. T. Lancaster, T. W. Körber, C. Becher, F. Schmidt-Kaler, D. F. V. James, and R. Blatt, *Nature* **429**, 734 (2004)
- [16] M. D. Barrett, J. Chiaverini, T. Schaetz, J. Britton, W.M. Itano, J.D. Jost, E. Knill, C. Langer, D. Leibfried, R. Ozeri, and D.J. Wineland, *Nature* **429**, 737 (2004)
- [17] F. De Martini, G. Innocenti, G. R. Jacobovitz and P. Mataloni, *Phys. Rev. Lett.* **59** 2955 (1987)
- [18] M.G. Raizen, R.J. Thompson, R.J. Brecha, H.J. Kimble, and H.J. Carmichel, *Phys. Rev. Lett.* **63**, 240 (1989)
- [19] P. Goy, J. M. Raimond, M. Gross and S. Haroche, *Phys. Rev. Lett.* **50** 1903 (1983)
- [20] D. Meschede, H. Walther and G. Müller, *Phys. Rev. Lett.* **54** 551 (1985)
- [21] R. G. Hulet, E. S. Hilfer and D. Kleppner, *Phys. Rev. Lett.* **55** 2137 (1985)
- [22] D. Kleppner, *Phys. Rev. Lett.* **47** 233 (1981)
- [23] G. Gabrielse and H. Dehmelt, *Phys. Rev. Lett.* **55** 67 (1985)
- [24] D. J. Heinzen, J. J. Childs, J. E. Thomas and M. S. Feld, *Phys. Rev. Lett.* **58** 1320 (1987)
- [25] Q. A. Turchette, R. J. Thompson and H. J. Kimble, *Appl. Phys.* **B60**, 1 (1995)
- [26] R. J. Thompson, G. Rempe and H. J. Kimble, *Phys. Rev. Lett.* **68** 1132 (1992)
- [27] K. An, J. J. Childs, R. R. Dasari and M. S. Feld, *Phys. Rev. Lett.* **73**, 3375 (1994)
- [28] C. J. Hood, T. W. Lynn, A. C. Doherty, A. S. Parkins and H. J. Kimble, *Science* **287**, 1457 (2000)
- [29] P. Münstermann, T. Fischer, P. Maunz, P. W. H. Pinsky and G. Rempe, H. J. Kimble, *Phys. Rev. Lett.* **82** 3791 (1999)
- [30] J. McKeever, J.R. Buck, A.D. Boozer, A. Kuzmich, H.-C. Nägerl, D.M. Stamper-Kurn, and H.J. Kimble, *Phys. Rev. Lett.* **90**, 133602 (2003)
- [31] P. Maunz, T. Puppe, I. Schuster, N. Syassen, P.W.H. Pinkse, and G. Rempe, quant-ph/0406136 (2004), preprint

- [32] J.A. Sauer, K.M. Fortier, M.S. Chang, C.D. Hamley, and M.S. Chapman, Phys. Rev. A **69**, 051804(R), (2004)
- [33] G. R. Gutöhrlein, M. Keller, K. Hayasaka, W. Lange, and H. Walther, Nature **414**, 49 (2001)
- [34] A.B. Mundt, A. Kreuter, C. Becher, D. Leibfried, J. Eschner, F. Schmidt-Kaler, and R. Blatt, Phys. Rev. Lett. **89**, 103001 (2002)
- [35] C. Weisbuch, M. Nishioka, A. Ishikawa and Y. Arakawa Phys. Rev. Lett. **69**, 3314 (1992)
- [36] E. Yablonovitch, T. J. Gmitter and R. Bhat, Phys. Rev. Lett. **61** 2546 (1988)
- [37] J. M. Gérard, B. Sermage, B. Gayral, B. Legrand, E. Costard and V. Thierry-Mieg, Phys. Rev. Lett. **81**, 1110 (1998)
- [38] B. Gayral, J.-M. Gerard ,B. Sermage, A. Lemaître, and C.Depuis, Appl. Phys. Lett. **78**, 2828 (2001)
- [39] A. Kiraz, P. Michler, C. Becher, B. Gayral, A. Imamoglu, L. Zhang, E. Hu, W. V. Schoenfeld, and P. M. Petroff, Appl. Phys. Lett. **78**, 3932 (2001)
- [40] G. S. Solomon, M. Pelton and Y. Yamamoto, Phys. Rev. Lett. **86** 3903 (2001)
- [41] T. D. Happ, I. I. Tartakovskii, V. D. Kulakovskii, J.-P. Reithmaier, M. Kamp and A. Forchel, Phys. Rev. B. **66** 041303(R) (2002)
- [42] Y.Z. Wang, B.L. Lu, Y.Q. Li, and Y.S. Liu, Opt. Lett. **20**, 770 (1995)
- [43] S. Götzinger, L. de S. Menezes, O. Benson, D.V. Talapin, N. Gaponik, H. Weller, A.L. Rogach, and V. Sandoghdar, J.Opt.B **6**, 154 (2004)
- [44] H. J. Carmichael, R. J. Brecha, M. G. Raizen, H. J. Kimble and P. R. Rice, Phys. Rev. A **40**(10), 5515(1989).
- [45] P. W. H. Pinkse, T. Fischer, P. Maunz and G. Rempe Nature **404**, 365 (2000)
- [46] A.B. Mundt, A. Kreuter, C. Russo, C. Becher, D. Leibfried, J. Eschner, F. Schmidt-Kaler, and R. Blatt, Appl. Phys. B **76**, 117 (2003)
- [47] K. Tanaker, T. Nakamura, T. Takamatsu, M. Yamanishi, Y. Lee, and T. Ishihara, Phys. Rev. Lett. **74**, 3380 (1995)
- [48] L. Tian, P. Rabl, R. Blatt, and P. Zoller, Phys. Rev. Lett. **92**, 2479021 (2004)
- [49] J.I. Cirac, P. Zoller, H.J. Kimble, H. Mabuchi: Phys. Rev. Lett. **78**, 3221 (1997)

Bibliography

- [50] R. Loudon, The quantum theory of light, Oxford University Press, second edition (1983)
- [51] P. Meystre, M. Sargent III, Elements of quantum optics, Springer University Press, third edition (1998)
- [52] P.W. Milonni, The Quantum Vacuum, Academic Press (1994)
- [53] D. Meschede, W. Jhe, and E.A. Hinds, Phys. Rev. A **41**, 1587 (1990)
- [54] E.T. Jaynes and F.W. Cummings, Proc. IEEE **51**, 89 (1963)
- [55] V. Weisskopf and E. Wigner Z. Phys. **63**, 54 (1930)
- [56] T.A. Welton, Phys. Rev. **74**, 1157 (1948)
- [57] W. Paul, O. Osberghaus and E. Fischer, Forschungsberichte des Wirtschafts- und Verkehrsministeriums Nordrhein–Westfalen 415, Westfälischer Verlag (1958)
- [58] W. Paul, Rev. Mod. Phys. **62**, 531 (1990).
- [59] P. K. Ghosh, Ion Traps, Clarendon Press (1995)
- [60] D. Leibfried, R. Blatt, C. Monroe, and D. J. Wineland, Rev.Mod.Phys. **75**, 281 (2003)
- [61] H. Kogelnik and T. Li, Appl.Optics **5** 1550 (1966)
- [62] G. Werth, *Applied Laser Spectroscopy* (eds. W. Demtröder and M. Inguscio), NATO ASI Series B, Vol. 241, 479, (Plenum Press, New York, 1990)
- [63] P. Gill, G.P. Barwood, H.A. Klein, G. Huang, S.A. Webster, P.J. Blythe, K. Hosaka, S.N. Lea, and H.S. Margolis, Meas. Sci. Technol. **14**, 1174 (2003)
- [64] T. Udem, R. Holtzwarth, and T.W. Hänsch, Nature **416**, 237 (2002)
- [65] A. Steane, C.F. Roos, D. Stevens, A. Mundt, D. Leibfried, F. Schmidt-Kaler, R. Blatt: Phys. Rev. A **62**, 042305 (2000)
- [66] D. E. Welty et al., ApJ **106** 533 (1996)
- [67] L.M. Hobbs et al., ApJ 334 L41 (1988)
- [68] A. Braneker et al., A&A **413**,681 (2004)
- [69] W. Bechter, Diploma-thesis Universität Innsbruck (1998)

- [70] G. Thalhammer, Diploma-thesis Universität Innsbruck (1999)
- [71] R. W. Drever, J. L. Hall, F. V. Kowalski, J. Hough, G. M. Ford, A. Munley and H. Ward, *Appl. Phys. B***31**, 97 (1983)
- [72] G. Blasbichler, Diploma-thesis Universität Innsbruck (2000)
- [73] N. Kjaergaard, L. Hornekaer, A. M. Thommesen, Z. Videsen, and M. Drewsen, *Appl.Phys.B* **71**, 207, (2000)
- [74] S. Gulde, D. Rotter, P. A. Barton, F. Schmidt-Kaler, R. Blatt, *Appl. Phys. B***73**, 861 (2001)
- [75] S. Stenholm, *Rev. Mod. Phys.* **58**(3), 699 (1986)
- [76] H.J. Metcalf and P. van der Straten, *Laser Cooling and Trapping*, Springer (1999)
- [77] D. F. V. James, *Appl. Phys. B***66**, 181 (1998)
- [78] R. D. Cowan, *The theory of atomic structure and spectra*, University of California Press (1981).
- [79] C. Roos, Th. Zeiger, H. Rohde, H. C. Nägerl, J. Eschner, D. Leibfried, F. Schmidt-Kaler, and R. Blatt, *Phys. Rev. Lett.* **83**, 4713 (1999)
- [80] Q. A. Turchette, D. Kielpinski, B. E. King, D. Leibfried, D. M. Meekhof, C. J. Myatt, M. A. Rowe, C. A. Sackett, C. S. Wood, W. M. Itano, C. Monroe, and D.J. Wineland *Phys. Rev. A* **61**, 63418 (2000)
- [81] S. Urabe, M. Watanabe, H. Imajo, and K. Hayasaka, *Opt. Lett.* **17**, 1140 (1992)
- [82] F. Arbes, T. Gudjons, F. Kurth, G. Werth, F. Marin, and M. Inguscio, *Z. Phys. D* **25**, 295 (1993)
- [83] F. Arbes, M. Benzing, T. Gudjons, F. Kurth, and G. Werth, *Z.Phys.D* **29**, 159 (1994)
- [84] M. Knoop, M. Vedel, and F. Vedel, *Phys. Rev. A* **52**, 3763 (1995)
- [85] T. Gudjons, B. Hilbert, P. Seibert, and G. Werth, *Europhys. Lett.* **33**, 595, (1996)
- [86] J. Lidberg, A. Al-Khalili, L.-O. Norlin, P. Royen, X. Tordoir, and S. Mannervik, *J.Phys.B.* **32**, 757 (1999)
- [87] S. Urabe, K. Hayasaka, M. Watanabe, H. Imajo, R. Ohmukai, and R. Hayashi, *Appl. Phys. B* **57**, 367 (1993).

Bibliography

- [88] G. Ritter and U. Eichmann, *J.Phys.B* **30**, L141 (1997)
- [89] M. Block, O. Rehm, P. Seibert, and G. Werth, *Eur.Phys.J.D* **7**, 461 (1999)
- [90] P. A. Barton, C. J. S. Donald, D. M. Lukas, D. A. Stevens, A. M. Steane, and D. N. Stacey, *Phys. Rev. A* **62**, 032503 (2000)
- [91] M. Knoop, C. Champenois, G. Hagel, M. Houssin, C. Lisowski, M. Vedel, and F. Vedel, arXiv:physics/0309094
- [92] P. Staantum, I.S. Jensen, R.G. Martinussen, D. Voigt, and M. Drewsen, *Phys. Rev. A* **69**, 32503(2004)
- [93] H. Dehmelt, *Bull.Am.Phys.Soc.* **20**, 60 (1975)
- [94] W. Nagourney, J. Sandberg, and H. Dehmelt, *Phys. Rev. Lett.* **56**, 2797 (1986)
- [95] T. Sauter, W. Neuhauser, R. Blatt, and P.E. Toschek, *Phys. Rev. Lett.* **57**, 1696 (1986)
- [96] J.C. Bergquist, R. Hulet, W. Itano, and D.J. Wineland, *Phys. Rev. Lett.* **57**, 1699 (1986)
- [97] V. Letchumanan, M.A. Wilson, P. Gill, and A.G. Sinclair, submitted to *Phys. Rev. A*
- [98] N. Yu, W. Nagourney, and H. Dehmelt, *Phys. Rev. Lett.* **78**, 4898 (1997)
- [99] M. Knoop, M. Vedel, and F. Vedel, *Phys. Rev. A* **58**,264 (1998)
- [100] E. Biemont and C.J. Zeippen, *Comments At. Mol. Phys.* **33**, 29 (1996)
- [101] M.A. Ali and Y.K. Kim, *Phys. Rev. A* **38**, 3992 (1988)
- [102] C. Guet and W.R. Johnson, *Phys. Rev. A* **44**, 1531 (1991)
- [103] S.S. Liaw, *Phys. Rev. A* **51**, R1723 (1995)
- [104] N. Vaeck, M. Godefroid, and C. Froese Fischer, *Phys. Rev. A* **46**, 3704 (1992)
- [105] T. Brage, C. Froese Fischer, N. Vaeck, M. Godefroid, and A. Hibbert, *Physica Scripta* **48**, 533 (1993)
- [106] C.J. Zeippen, *A&A* **229**, 248 (1990)
- [107] F. Schmidt-Kaler, S. Gulde, M. Riebe, T. Deuschle, A. Kreuter, G. Lancaster, C. Becher, J. Eschner, H. Häffner, and R. Blatt, *J.Phys.B.* **36**, 623 (2003)

- [108] J.R. Taylor, Introduction to Error Analysis, University Science Books (1982)
- [109] J. Eschner, Ch. Raab, F. Schmidt-Kaler, R. Blatt, Nature **413**, 495 (2001)
- [110] J. Eschner, Eur.Phys.J.D **22**, 341 (2003)
- [111] J.I. Cirac, R. Blatt, P. Zoller, W.D. Phillips: Phys. Rev. A **46**, 2668 (1992)
- [112] V. Bužek, G. Drobný, M.S. Kim, G. Adam, P.L. Knight: Phys. Rev. A **56**, 2352 (1997)
- [113] A. M. Mundt, Ph. D. thesis Universität Innsbruck (2003)
- [114] S. Gulde, Ph. D. thesis Universität Innsbruck (2003)
- [115] P. A. Bouchev, Ph. D. thesis Universität Innsbruck (2004)
- [116] C. Raab, Ph. D. thesis Universität Innsbruck (2001)
- [117] H. F. Rohde, Ph. D. thesis Universität Innsbruck (2001)
- [118] C. F. Roos, Ph. D. thesis Universität Innsbruck (2000)
- [119] H. C. Nägerl, Ph. D. thesis Universität Innsbruck (1998)
- [120] C. Maurer, C. Becher, C. Russo, J. Eschner and R. Blatt, New J. Phys. **6**, 94 (2004)

Bibliography

The final words in this thesis are reserved for the people who not only supported this work but also made it possible in the first place; from the scientific and personal point of view. In the lab, all were splendid colleagues, some have even become good friends. So a big **Thank you** to:

- Rainer Blatt, the head of the team, for admitting me into the group and supporting this work throughout.
- Christoph, my project supervisor for scientific guidance, especially during writing up and for careful proof reading of my thesis.
- Ferdi and Jürgen for excellent assistance in experimental and theoretical questions, respectively, and good humour.
- Andi who earned his PhD with the first results from this experimental set-up and who turned out to be an excellent partner and fellow in and outside the lab.
- Gavin who joined in later for THE important measurements when I needed help most.
- Hartmut for being available for good scientific advice anytime of the day and for being the perfect partner in the car sharing deal.
- Stephan for always good fun in the lab and in our spare time.
- The rest of the group for creating an enjoyable working atmosphere.
- The cooking group (KGB) for always providing superior food and conversation for lunch.
- My parents for continuous support from up north.
- Sylvia, my sweet girl, for making life in general great fun and for the pizza during night shifts.